EXPLORING QUANTUM PHENOMENA IN HYBRID DOUBLE NANOWIRE DEVICES

Alexandros Vekris

Ph.D. Thesis
Center for Quantum Devices
Niels Bohr Institute
University of Copenhagen

Academic advisors:
Assoc. Prof. Kasper Grove-Rasmussen
Prof. Xiaohui Qiu

Co-supervisor:
Prof. Hongqi Xu

Assessment committee:
Assoc. Prof. Ferdinand Kuemmeth
Assist. Prof. Attila Geresdi
Dr. Eduardo Jian Hua Lee

February 28, 2022

CONTENTS

CONTENTS

LIST OF FIGURES

ABSTRACT

This thesis investigates quantum phenomena in superconductor-semiconductor junctions fabricated in a new material platform of *in-situ* grown parallel nanowires motivated by theoretical proposals describing quantum states such as coupled hybrid states and topological effects in such devices. Even though these two phenomena were not observed in these 1st generation devices, a systematic study of novel double-nanowire platforms was performed in various geometries. Initially, supercurrent was studied through a parallel double quantum dot system which was formed in a double nanowire Josephson junction. Minimal inter-dot coupling was found. Driven by the flux-induced studies in full shell nanowires, a first study of Little-Parks oscillations in double nanowires was performed, showing that an ellipsoid cross section, such one of double nanowires, can be fitted with good agreement using a simple model. The final study of double nanowires shown in this thesis involves multi-probe measurements of superconducting islands. Temperature analysis of the island resonances is well understood using a thermodynamic model, and the behavior of the resonances points towards a common sub-gap state extending across the device. Finally, insight on the physics of a superconducting island in close proximity to a tunable quantum dot is investigated in a single nanowire, where Coulomb-aided Yu-Shiba-Rusinov states are studied in various regimes.

DANSK RESUME

Denne afhandling omhandler kvantefænomener i superleder-halvleder komponenter baseret på en ny materiale platform bestående af in-situ syntetiserede parallelle nanotråde. Komponenterne er motiveret af teorier om for eksempel koblede hybride kvantetilstande og topologiske fænomener. Selvom ovenstående fænomener ikke bliver realiseret, udgør afhandlingen et systematisk studie af kvantefænomener i forskellige dobbeltnanotråde komponentgeometrier. Først fremlægges superstrømsmålinger i parallelle kvantepunkter fremstillet i dobbeltnanotråde Josephson dioder, hvor en øvre grænse for tunnelkoblingen mellem de to kvantepunkter bestemmes. Derefter bliver målinger af Little-Parks effekten i dobbeltnanotråde med aluminium fuldskal for første gang vist og analyseret. Resultaterne viser at Litte-Parks effekten i dobbeltnanotråden, som har et ellipseformet tværsnit, kan beskrives med en simpel model. Det sidste studie af dobbeltnanotråde komponenter omhandler multi-terminal målinger af superledende øer. Temperaturafhængigheden af de observerede konduktans resonanser er analyseret ved hjælp af en termodynamisk model og analysen indikerer een sub-gap kvantetilstand i hele komponenten. Endelig præsenteres målinger på en superledende ø koblet til et kvantepunkt fremstillet i en enkelt nanotråd, hvor Coulomb assisterede Yu-Shiba-Rusinov tilstande bliver studeret i forskellige regimer.

ACKNOWLEDGMENTS

PUBLICATIONS

Results presented in this thesis are adapted from manuscripts 1-4 and 6.

1. **Alexandros Vekris**, Juan Carlos Estrada Saldaña, Thomas Kanne, Thor Hvid-Olsen, Mikelis Marnauza, Dags Olsteins, Matteo M. Wauters, Michele Burrello, Jesper Nygård and Kasper Grove-Rasmussen.
   Electronic transport through double-nanowire superconducting islands.
   In preparation

2. Thomas Kanne, Dags Olsteins, Mikelis Marnauza, **Alexandros Vekris**, Juan Carlos Estrada Saldaña, Sara Loric, Rasmus D. Schlosser, Daniel Ross, Szabolcs Csonka, Kasper Grove-Rasmussen and Jesper Nygård.
   Double Nanowires for Hybrid Quantum Devices.
   Adv. Funct. Mater., 2107926 (2021).

3. **Alexandros Vekris**, Juan Carlos Estrada Saldaña, Joeri de Bruijckere, Sara Lori, Thomas Kanne, Mikelis Marnauza, Dags Olsteins, Jesper Nygård and Kasper Grove-Rasmussen.
   Asymmetric Little-Parks oscillations in full shell double nanowires.
   Sci. Rep., **11**, 19034 (2021).

4. **Alexandros Vekris**, Juan Carlos Estrada Saldaña, Thomas Kanne, Mikelis Marnauza, Dags Olsteins, Furong Fan, Xiaobo Li, Thor Hvid-Olsen, Xiaohui Qiu, Hongqi Xu, Jesper Nygård and Kasper

Grove-Rasmussen.
Josephson junctions in double nanowires bridged by in-situ deposited superconductors.
Phys. Rev. Res., **3** (3), 033240 (2021).

5. Gorm Ole Steffensen, Juan Carlos Estrada Saldaña, **Alexandros Vekris**, Peter Krogstrup, Kasper Grove-Rasmussen, Jesper Nygård, Alfredo Levy Yeyati and Jens Paaske.
Direct Transport between Superconducting Subgap States in a Double Quantum Dot.
ArXiv prerint, arXiv:2105.06815 (2021).

6. Juan Carlos Estrada Saldaña, **Alexandros Vekris**, Luka Pavešić, Peter Krogstrup, Rok Žitko, Kasper Grove-Rasmussen and Jesper Nygård.
Excitations in a superconducting Coulombic energy gap.
ArXiv prerint, arXiv:2101.10794 (2021).

7. Juan Carlos Estrada Saldaña, **Alexandros Vekris**, Rok Žitko, Gorm Steffensen, Peter Krogstrup, Jens Paaske, Kasper Grove-Rasmussen and Jesper Nygård.
Two-impurity Yu-Shiba-Rusinov states in coupled quantum dots.
Phys. Rev. B, **102**, 195143 (2020).

8. Juan Carlos Estrada Saldaña, **Alexandros Vekris**, Victoria Sosnovtseva, Thomas Kanne, Peter Krogstrup, Kasper Grove-Rasmussen and Jesper Nygård.
Temperature induced shifts of Yu-Shiba-Rusinov resonances in nanowire-based hybrid quantum dots.
Commun. Phys. **3**, 125 (2020).

9. Juan Carlos Estrada Saldaña, **Alexandros Vekris**, Gorm Steffensen, Rok Žitko, Peter Krogstrup, Jens Paaske, Kasper Grove-Rasmussen and Jesper Nygård.
Supercurrent in a Double Quantum Dot.
Phys. Rev. Lett. **121**, 257701 (2018).

1

INTRODUCTION

To understand a complex physical problem, the most effective way is to design and study the simplest manifestation of it. In mesoscopic physics, this pattern has been followed to understand how different types of materials such as metals and semiconductors behave. Understanding their properties, e.g., the density of states in these materials, allowed us to study more complicated phases of matter, such as superconductivity. Amongst their peculiar properties, superconductors exhibit no electrical resistance when a voltage is applied across them. However, they behave differently when interrupted by a non-superconducting material, for example a semiconductor. Such a system can be a quasi one-dimensional semiconducting nanowire, which is covered by a superconducting material. Selectively removing the superconductor can form a junction where its carrier density can be controlled. This system is known as a Josephson junction [1] and is one of the most important building blocks of quantum nanoelectronics. With the advancement of nanofabrication and the possible realization of more complex nanostructures, physicists have been inspired to formulate theoretical proposals that involve these building blocks and predict Yu-Shiba-Rusinov (YSR) interactions [2–5], e.g., in chains of adatoms [6], and exotic quantum transport phenomena, such as Majorana zero modes (MZMs) [7], parafermions [8] and the topological Kondo effect [9,10].

The existence of MZMs in nanowires has been extensively investi-

gated [11–14] during the past years in semiconducting InAs nanowires coupled to superconducting materials and is still debated [15, 16]. As new theoretical proposals [8–10] require parallel nanowire platforms, researchers have investigated such systems by forming parallel nanowires with a top-down approach [17, 18]. However, these techniques host challenges such as lack of reproducibility and higher quasiparticle poisoning of the superconducting materials, due to the compromised semiconductor/superconductor interface. To tackle these challenges, the growth of *in-situ* double nanowires coupled by epitaxially grown aluminum has been recently realised [19], paving the way for the fabrication of high quality double nanowires devices, with the aim of investigating the proposed geometries involving e.g. YSR physics, Cooper-pair splitting and the Topological Kondo effect.

The subject of this thesis involves the utilization and characterization of such *in-situ* grown parallel-nanowires in various geometries, with the aim of acquiring knowledge regarding their properties and investigating possible exotic phenomena. Specifically, Josephson junctions are investigated in double nanowires, where the nanowire carrier density is almost depleted, leading to discrete energy levels and quantum dot (QD) formation on each nanowire. The inter-dot coupling between the QDs is found weak, leading to independent ground states on each QD system. The switching current through both QDs is monitored as a function of QD occupation and coupling between the superconducting contacts and the QDs. Furthermore, the superconducting properties of aluminum islands are studied by defining superconducting islands in double nanowires. Coulomb resonances can be probed by various two-terminal combinations, and the presence of a common subgap state extending along the device is argued. Moreover, the Little-Parks effect is investigated in full-shell double nanowires, showing that the nanowires behave as a single object and follows with good agreement the Abrikosov-Gorkov expression for screening currents [20, 21]. Finally, escaping the scope of double nanowires, the interaction of a superconducting island with a tunable magnetic impurity is investigated, showing altered Yu-Shiba-Rusinov excitations due to the charging of the superconducting island.

This thesis is divided into 7 chapters. Chapter 2 introduces the main concepts that are used in the experiments such as superconductiv-

ity, basics of Coulomb blockade and Yu-Shiba-Rusinov screening, while Chapter 3 covers the fabrication steps needed to create nanowire-based samples as well as the measurements techniques used. Chapters 4-8 contain the experimental results of the thesis. Chapter 4 presents the double-nanowire growth specifics and initial transport measurements in such geometries. In Chapter 5, we show a study of a parallel double quantum-dot with weak interdot coupling in a double-nanowire Josephson junction geometry. Chapter 6 covers the characterization of superconducting island devices in different charging regimes defined in double nanowires. Moreover, Chapter 7 describes the Little-Parks effect measured in parallel full-shell nanowires. Chapter 8 focuses on the interaction of a superconducting island with a quantum dot in a single nanowire. Finally, the thesis ends with conclusions and outlook of the field.

2

THEORETICAL BACKGROUND

This chapter covers the basic toolbox that is used in order to comprehend and interpret the experimental data showed in this thesis. Initially, superconductivity is introduced as well as the concepts of Andreev reflection and sub-gap states. Then, the Josephson effect is described followed by an introduction to Coulomb blockade in semiconductors and superconductors. Finally, a more detailed description of the Yu-Shiba-Rusinov states is given, as well as the consequences of finite charging energy of the superconductor.

2.1 Superconductivity

Superconductivity was first realized by H. K. Onnes in 1911 when he monitored the electrical resistance of mercury as a function of temperature. For temperatures less than mercury's critical temperature (T_c), its electrical resistance was found very close to zero. In normal materials, electrons which carry charge through an object scatter in the lattice (i.e. phonons) or with defects in the material, causing a finite electrical resistance when applying a voltage across it. However, when a material turns superconducting electrons with opposite spins and momentum bond, forming Cooper pairs. Hence, electrical transport occurs via Cooper pairs (2e) rather than single electrons (e). The attractive force between the two electrons is mediated by phonons via the lattice of the

material. Since Cooper pairs have integer spin, they are bosons and as a result can be condensed in a single ground state, not following the Pauli's exclusion principle as electrons in normal materials.

Another striking difference between superconducting and normal materials is the density of states (DOS). In a superconductor, all electrons within an energy gap from the Fermi energy (E_F) condense into Cooper pairs. This energy gap is known as the superconducting gap Δ and at larger excitation energies there is a finite density of states ρ_{qp} that quasiparticles occupy (eq. 2.1).

$$\rho_{QP} = \begin{cases} 0 & E < |\Delta| \\ \frac{E}{\sqrt{E^2 - \Delta^2}} & E > |\Delta| \end{cases} \tag{2.1}$$

The density of states in a superconducting material is shown in Fig. 2.1a, where no single quasiparticle states exist within $-\Delta$ to Δ and Cooper pairs condense on the Fermi energy. A peak in the DOS is observed on the coherence peaks ($\pm\Delta$). That peak is decaying for larger energies, where the DOS of normal materials is recovered. The presence of the energy gap is the reason why superconducting materials exhibit no electrical resistance, as Cooper pairs are protected from quasiparticle states by the energy gap Δ.

2.1.1 Andreev reflection

Placing a superconducting material in contact with a normal material creates a transport process known as Andreev reflection. This process involves an electron that tunnels from a normal metal to the superconductor followed by a hole being reflected back to the metal. This causes a net 2e transport to the superconductor, which forms a Cooper pair at the Fermi energy. Taking a step forward, embedding a normal metal between two superconductors gives rise to a standing-wave effect, known as Andreev bound state (ABS) [22]. When the distance between the two superconductors w is smaller than the coherence length ξ, the system -in the single channel limit- is described by the energy of the ABS which is given by Eq. 2.2, where Δ is the superconducting gap, T is the transmission coefficient though the non-superconducting material (weak-link)
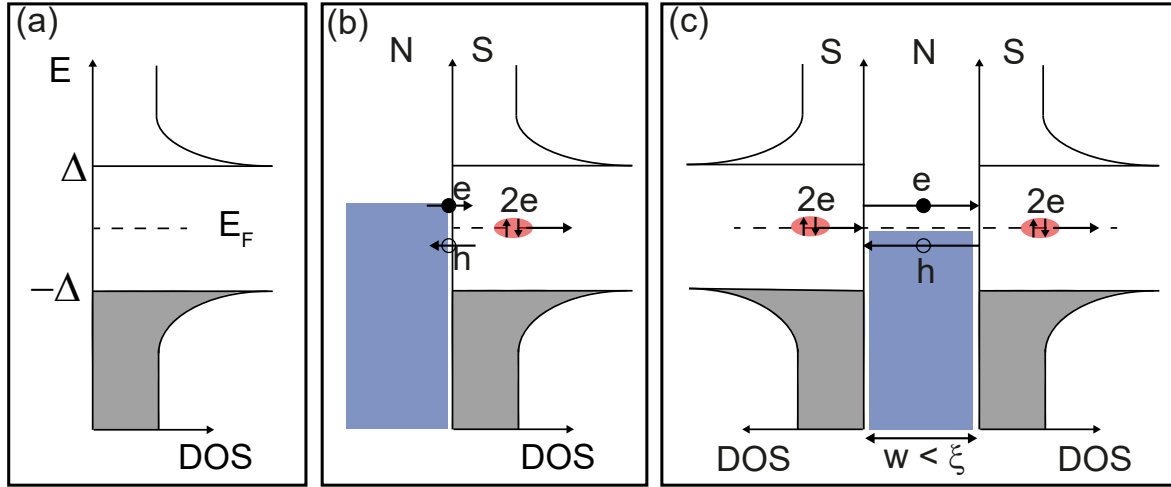
Figure 2.1: (a) Density of states (DOS) as a function of energy in a superconductor. No quasiparticle states exist within the gap $\pm\Delta$ while Cooper pairs condense on the Fermi energy. (b) Normal metal-Superconductor (NS) junction gives rise to a special process in which an electron is reflected as a hole in the NS interface, forming a Cooper pair on the superconductor. (c) SNS junction in which a single Andreev bound state (ABS) can be formed for w $< \xi$ where w is the width of the normal metal and ξ the superconducting coherence length.

and $\phi = \phi_1 - \phi_2$ is the phase difference between the two superconductors.

$$E_{\mathrm{ABS}} = \pm\Delta\sqrt{1 - T \cdot \sin^2(\phi/2)} \tag{2.2}$$

2.1.2 Beyond Andreev sub-gap states

With the advancement of nanofabrication, vast research has been conducted in nanostructures coupled to superconducting materials, realizing ABS [24] and other families of bound states, such as Yu-Shiba-Rusinov states [2–5, 25], superconducting Coulombic excitations [26] and more. Note, that the ABS is used broadly for all states. Furthermore, theoretical proposals involving exotic phases in nanostructures, such as parallel nanowires, have been introduced [8–10]. An overview of these sub-gap states is shown in Fig. 2.2, where a brief introduction is given for each family of states. In the top left of the figure, a generic device hosting sub-gap states is shown. At the superconductor-semiconductor interface, sub-gap states are formed as depicted in the energy versus DOS diagram enclosed in the red rectangle. These sub-
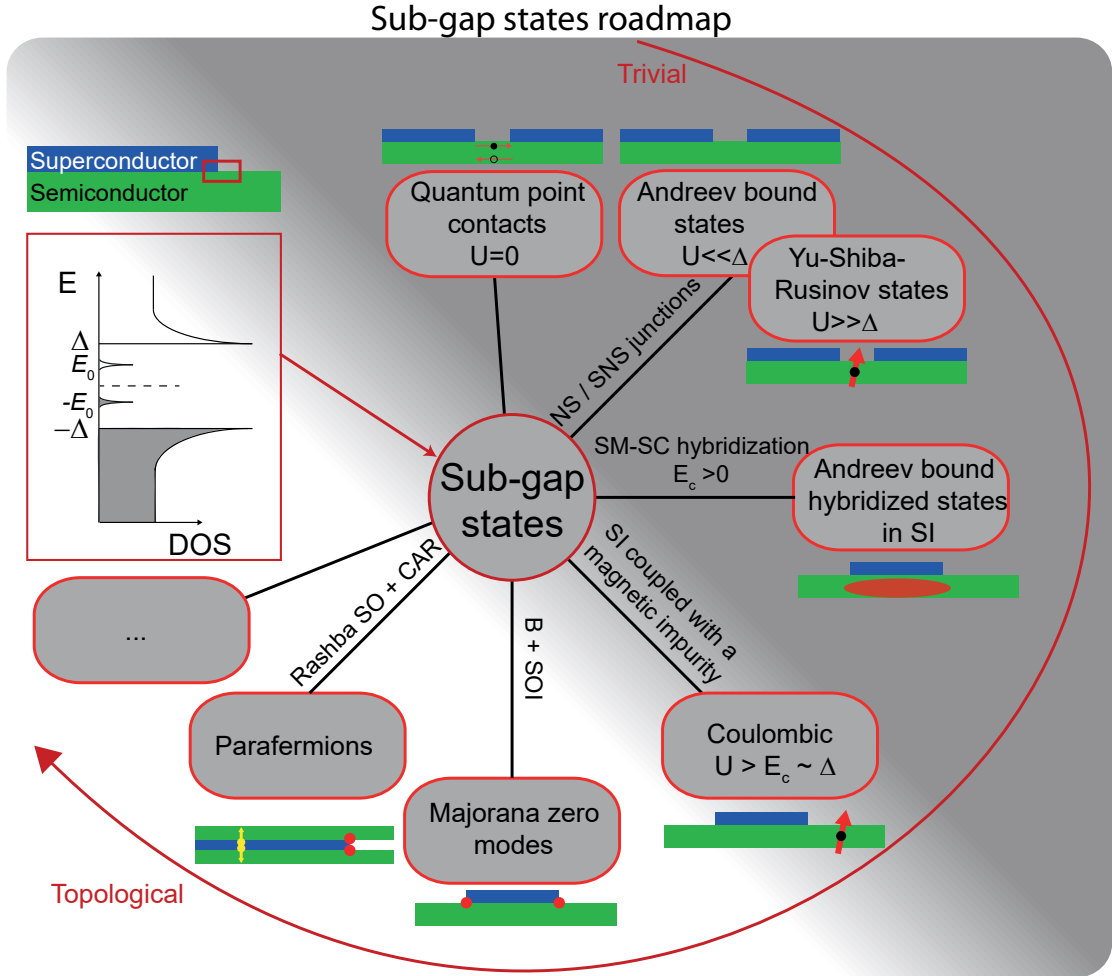
Figure 2.2: Sub-gap states roadmap. Typically, such states are studied in semiconductor-superconductor interfaces, such as semiconducting nanowires with epitaxial aluminum [23]. In a ballistic junction (quantum point contact) ABS are formed and are mediated by the phase difference of the two superconductors. In NS or SNS junctions, ABS arise in the limit where Δ is the dominant energy scale. For a quantum dot formed in the semiconductor with charging energy U, Yu-Shiba-Rusinov (YSR) physics are present which form an exchange singlet state involving quasiparticles in the superconductor and the unpaired spin. In the interface between a superconducting island with a finite charging energy E_c and a semiconductor, hybridized sub-gap states are formed which are caused by the proximity effect. When a magnetic impurity interacts with a superconducting island, YSR states are aided by the Coulomb repulsion in the superconducting island (superconducting Coulombic excitations). Majorana zero modes [7] (MZMs) and parafermions [8] (a generalization of MZMs) are proposed to exist in 1-D nanostructures coupled to superconductors under specific requirements (spin-orbit interaction and Zeeman field for MZMs; Rashba spin-orbit and crossed Andreev reflection for parafermions).

gap states are theoretically infinitesimally wide and exist inside the superconducting gap at energies $\pm E_0$. Experimentally, they are broadened by e.g. temperature or coupling to adjacent leads and can therefore be observed. Following the red arrow (from trivial to topological), the complexity of the sub-gap states in increased. In the simple scenario of a superconductor-normal-semiconductor (SNS) junction with a ballistic N part ($T \approx 1$), ABS are formed which depend on the transmission and the phase difference between the two superconductors, as described in Eq. 2.2. When QDs are formed in the junction, ABS or YSR states occur, depending on the limits of the U/Δ fraction[1]. The superconductor/semiconductor interface gives rise to hybridization, which may bring states E_0 at lower energy than Δ [27], making them experimentally visible via electrical transport [13, 14, 28]. In a system where a superconducting island (SI) with finite charging energy E_c interacts with a tunable QD, the typical YSR spectrum is disturbed, and new features may arise, coined superconducting Coulombic excitations. The presence of Rashba spin-orbit interaction, crossed Andreev reflection and Zeeman field, together with potentially ballistic nanowires, are the main ingredients required to host topological states, such as MZMs [7, 15] or parafermions [8].

Further explanation about specific sub-gap states is given in the following sections and chapters of this thesis. YSR states are encountered in Chapter 5, hybridized sub-gap states in superconducting island-semiconductor interfaces are studied in Chapter 6 and experimental data regarding superconducting Coulombic excitations (SCE) involving a superconducting island coupled to a magnetic impurity are studied in Chapter 8.

2.2 Josephson effect

An important property of superconducting junctions that is studied in this thesis is the Josephson effect [1]. This effect describes the transport of dissipationless current (also known as supercurrent) through a non-superconducting material (weak-link), as shown in Fig. 2.1c. The

---

[1]For the charging energy, the symbol U is used when referring to semiconducting QDs and E_c for superconducting islands.

wavefunctions of the two superconductors overlap, effectively proximitizing the weak-link, and Cooper pair transport can be realized. In the weakly coupled regime, the magnitude of the supercurrent depends on the phase difference $\phi = \phi_1 - \phi_2$ of the two superconductors and is given by Eq. 2.3,

$$I_s = I_c \cdot \sin(\phi) \tag{2.3}$$

where I_c is the maximum critical current the Josephson junction (JJ) can withstand. This is known as the DC Josephson effect. The magnitude of I_c depends on the weak-link and above its threshold a voltage difference is applied between the two superconductors.
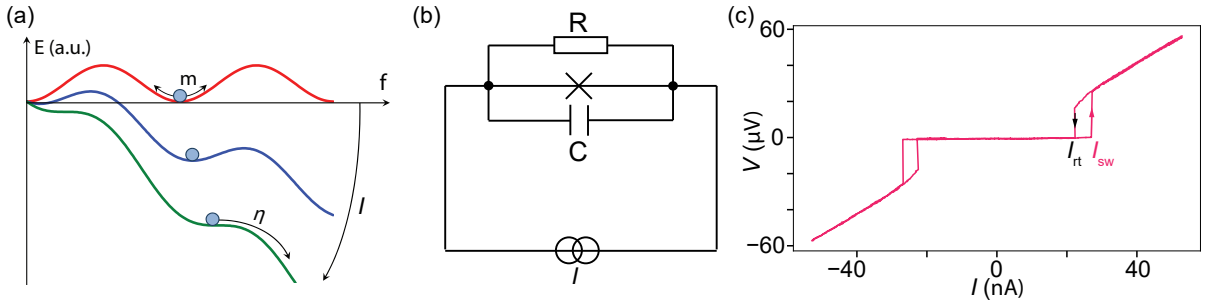
Figure 2.3: (a) Energy of a particle as a function of frequency in a tilted washboard potential. Larger tilt (higher current I) affects the forces applied on the particle. For high enough tilt ($I > I_c$ the particle escapes from the minima. Higher mass m and viscosity η make the particle more resilient to the tilt (or higher current). (b) Equivalent circuit for a JJ used in the RCSJ model. The Josephson junction is modeled as three components in parallel, a resistor, the JJ and a capacitor. (c) Example of an $I_{bias} - V$ curve of a nanowire Josephson junction. The switching I_{sw} and retrapping I_{rt} currents are recorded in different values, showing hysteretic behaviour, owing to the underdamped nature of the junction.

An intuitive system describing the Josephson effect and the switching from the superconducting to the normal state (for $I > I_c$) is the tilted washboard potential depicted in Fig. 2.3a. Here, for $I < I_c$ the washboard is tilted, but the particle is trapped in a local minimum, having a well defined phase ϕ. For larger current (larger tilt), the particle escapes from the local minimum and cannot be retrapped due to its high momentum. This is analogous with an ever-evolving phase ϕ, yielding on average $\sin(\phi)=0$ and no supercurrent. A way to simulate a Josephson junction is by using the resistively and capacitively shunted Josephson junction (RCSJ) model, in which a JJ is modeled in parallel to a resistor and a capacitor that describe the JJ's capacitance

10

and resistance (Fig. 2.3b). In the tilted washboard potential, the capacitance C is analogous to the mass m of the particle and the resistance R is inversely proportional to the viscosity η that the particle is experiencing. Visualizing the above analogies in nanostructures, an $I_{\text{bias}} - V$ measurement of a nanowire Josephson junction is shown in Fig. 2.3c. Measuring from zero applied current to positive values, no voltage drop is recorded until the switching I_{sw}, where the junction is dissipative and thus turns normal. Sweeping the current from a value larger than I_{sw} towards zero, yields a switching at $I_{\text{rt}} < I_{\text{sw}}$, owing to the heating effect in JJs. This can be also thought in terms of the tilted washboard potential; if the particle is running down the potential ($I > I_{\text{c}}$), due to its inertia it will be harder to stop it and bring it on a local minimum (superconducting state). Junctions exhibiting this hysteretic behaviour are known as underdamped [29]. The JJs studied in this thesis exhibit non-ideal I-V curves when the weak-link is tuned in the Coulomb blockade regime. Specifically, the I-V curves exhibit finite resistance in the supercurrent branch, which can be attributed to the effect of noise in small JJs when tuned in the low Josephson energy regime $E_{\text{J}} \ll U$ [30,31], where $E_{\text{J}} \propto I_{\text{c}}$.

2.3 Coulomb blockade

As several of the experiments presented in this thesis involve small objects, e.g., quantum dots and superconducting islands, it is important to introduce the concept of Coulomb blockade. Coulomb blockade can be observed in a nanostructure when three requirements are met: 1) Tunnel barriers are strong enough to yield resistance of $R_{\text{t}} \geq h/e^2$, 2) The thermal energy is significantly weaker than the charging energy $U \gg k_B T$ and 3) The applied bias on the object is weaker than the charging energy $U > eV_{\text{sd}}$, where $U = e^2/C$. The above conditions reassure that only single-electron tunneling is present, as the wavefunction overlap of the source/drain and the QD is weak enough, and additional electrons cannot be added on the QD through thermal excitations.

2.3.1 Quantum dots

Initially, I will present quantum dots formed in semiconducting materials, such as InAs nanowires. Figure 2.4a shows a schematic of a QD (cyan ellipse), where its levels are tuned by V_g and two source-drain leads. Gates $V_{L,R}$ are used to form tunnel barriers between the leads and the QD. Figure 2.4b shows a scanning electron microscopy (SEM) image of a nanowire based QD device, where bottomgates are used to form tunnel barriers and tune the levels of the QD. Focusing on the energy schematics, Figure 2.4c-h illustrates various states and transport processes of a QD embedded in two normal contacts. Blue shaded rectangles represent the filled states of the metallic leads and the gray bars the tunnel barriers formed by the gates to define the QD. The dashed line corresponds to the chemical potential $\mu_{L,R}$ of the leads. Figure 2.4c illustrates the case where the QD is occupied with an even number n of electrons. The energy difference of states with n and n+1 electrons yields the electrochemical potential of the QD $\mu_{n+1} = E_{n+1} - E_n$. As the lowest energy unoccupied level (μ_{n+1}) is above the chemical potential of the leads, there is no transport through the system. Apart from the charging energy U that needs to be paid to access μ_{n+1}, the energy to access the next QD level is required, which is the level spacing δE. This occurs because each level can be occupied by two electrons due to the Pauli exclusion principle. Figure 2.4d shows the case where odd number of electrons are added in the QD. Likewise to Fig. 2.4c, no transport occurs through the QD and the energy needed to add an electron is U as it can be added on the same QD level. To lift the Coulomb blockade and activate transport through the system, it is possible to tune the levels of the QD using the gate, bringing it on resonance with the leads. This produces sequential tunneling through the QD (Figure 2.4e). Alternatively, applying a source drain bias V_{sd} may also trigger transport through the system by lifting the chemical potential of the source as seen in Figure 2.4f. The above schematics assume weak coupling $\Gamma \ll U$ between the leads and the QD. For intermediate couplings, higher order transport processes can occur, which do not rely on sequential tunneling (having the QD level on resonance with the leads). These processes involve excited states and are know as elastic and inelastic cotunneling (shown in Figure 2.4g,h respectively).

12
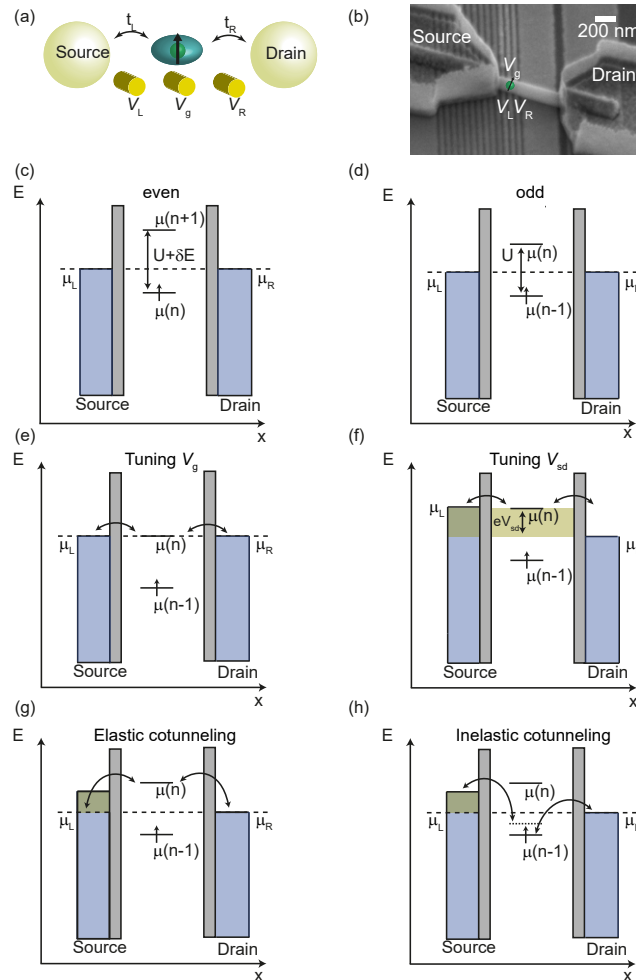
Figure 2.4: (a) Schematic illustrating a QD formed between two metallic leads. Typically, a series of gates are used to define tunnel barriers ($V_{L,R}$) and to tune the levels of the QD V_g. SEM image of a nanowire based QD device. Bottomgates are used to define tunnel barriers and to tune the QD levels. (c-d) Energy schematics for a metal-QD-metal junction for even (c) and odd (d) number of electrons on the QD. As the chemical potential of the leads is not aligned with the chemical potential of the QD, there is no transport. For the even occupation, an additional energy δE needs to be paid to add an electron due to the level spacing. The Coulomb blockade can be lifted by bringing the QD level on resonance with the leads by either tuning the level (e) or by applying a bias V_{sd} (f). Elastic (g) and inelastic (h) cotunneling processes can occur involving excited states of the QD for intermediate couplings between the leads and the QD.

The difference between the two is that in elastic cotunneling the energy is preserved after one transport cycle, while in inelastic processes the QD has higher energy. These effects are common in QD junctions.

The parity of a QD is also relevant for the ground state of the sys-

tem. When a QD has even number of electrons, each pair forms a singlet ground state with spin $S = 0$. However, for odd number an electron is "free" to choose a spin up or spin down orientation, and the ground state is a degenerate doublet with spin $S = \pm\frac{1}{2}$ (for no applied magnetic field). As described in the following section, the ground state can affect the sign of supercurrent and more insight regarding this effect can be found in Chapter 5, where a double quantum dot Josephson junction is studied.

2.3.2 π-junction
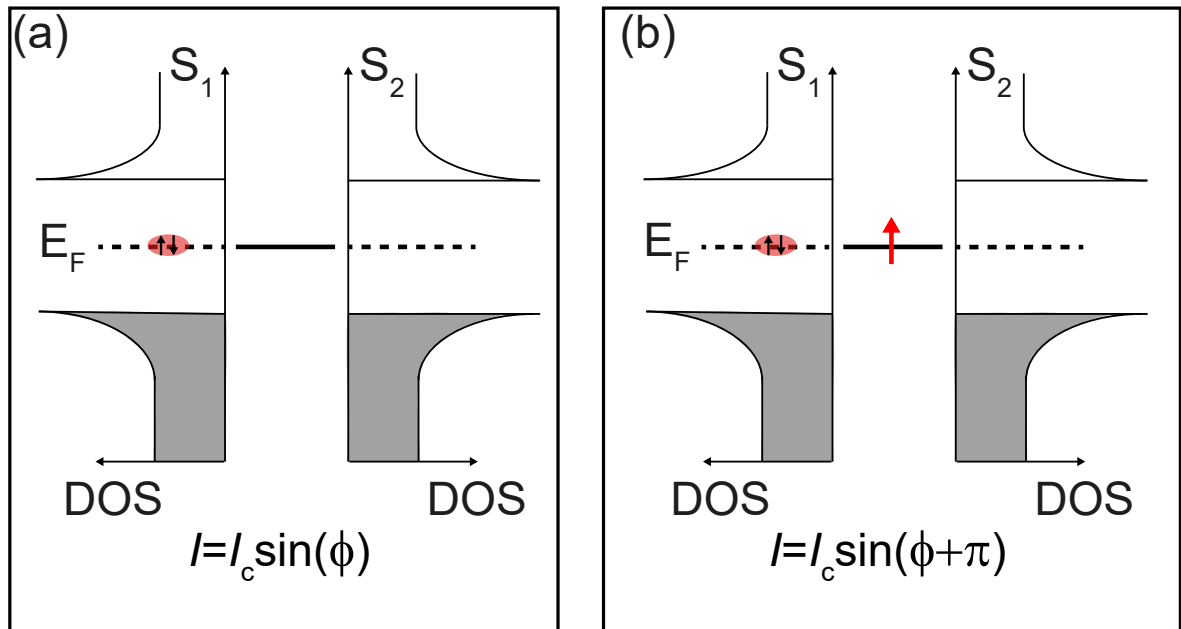
Figure 2.5: Current phase relation of a superconductor-quantum dot-superconductor (S-QD-S) Josephson junction for even (a) and odd (b) number of electrons on the QD. Even number of electrons on the QD have no influence on the current phase relation, however odd numbers result in a phase shift π, causing supercurrent reversal (negative supercurrent).

Experimentally, the Josephson effect has been realized in multiple geometries, where the weak link is not an insulator or a bulk semiconductor, but a tunable system that hosts fixed number of electrons (quantum dot) [32,33]. When a QD is embedded between two superconductors, its parity plays a role in the supercurrent magnitude and sign. Figure 2.5 energy diagrams for even and odd number of electrons in the

QD. When even number of electrons occupy the QD, the ground state is a singlet and the current phase relation of Eq. 2.3 remains unaltered. Passing a Cooper pair through the QD involves passing an electron one by one through the QD level, following Pauli's exclusion principle. The two electrons are annihilated from the source ($c_\uparrow$, $c_\downarrow$) and created in the drain ($c_\uparrow^\dagger$, $c_\downarrow^\dagger$). However, for odd number of electrons (doublet ground state) the phase acquires a π shift, which is equivalent to negative supercurrent. This π shift occurs because the sequence which the Cooper pairs transport through the QD has been altered, as the two annihilation operators cannot be initially performed. Hence, permutations of the operators are needed, which result to a negative sign on the supercurrent.

2.3.3 Double quantum dots
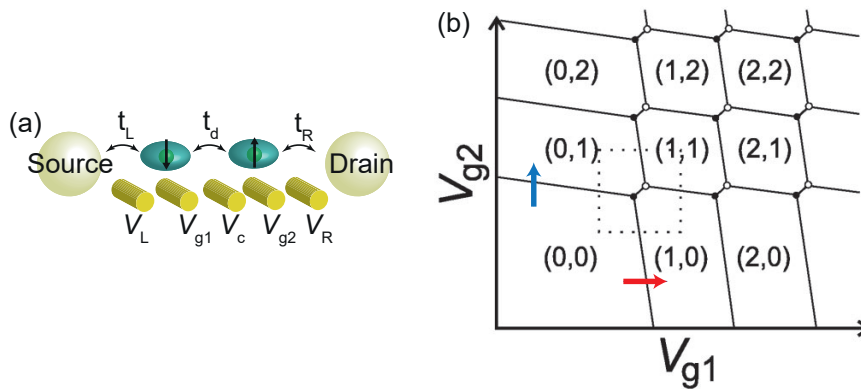
Figure 2.6: (a) Schematic representation of a double quantum dot (DQD). The two QDs are formed by tuning the carrier density of the semiconductor, and their interdot tunneling t_d is tuned by a gate. (b) Charge stability diagram of a DQD assuming no interdot tunneling. Two sets of parallel lines are seen which describe the parity transitions for each QD. Crossing such a line adds an electron to the corresponding QD (following the blue arrow adds charges on the right QD, while the red on the left QD). Each region is defined by a fixed number of charges on the two QDs (N,M). The dashed square indicates the triple-points line, which links charge sectors with (N,M) and (N+1,M+1) electrons. The length of that line is given by the mutual capacitance C_m and interdot tunneling t_d of the two QDs. Adapted from [34].

In this section the physics of a double QD (DQD) system is described. Following the reasoning of the previous section, it is possible to form two QDs in series or in parallel by using the appropriate gate configuration. In this case, the capacitive coupling C_m between the two QDs

becomes relevant, as well as the interdot coupling t_d. A charge stability diagram schematic is shown in Fig. 2.6b. A hexagonal pattern (honeycomb) is defined, where each hexagon has a fixed number of electrons. Crossing a line corresponds to passing a charge degeneracy of the corresponding QD, adding an electron on it. For instance, starting from the (0,0) charge sector (0 electrons on each QD) and increasing V_{g1}, effectively tunes the level of QD_1 and brings the system to a new ground state, the (1,0) charge sector. A characteristic of this pattern is the triple points line that is connecting charge states (N,M) and (N+1,M+1). This line is dependent on the mutual capacitance C_m and interdot tunneling t_d of the two QDs.
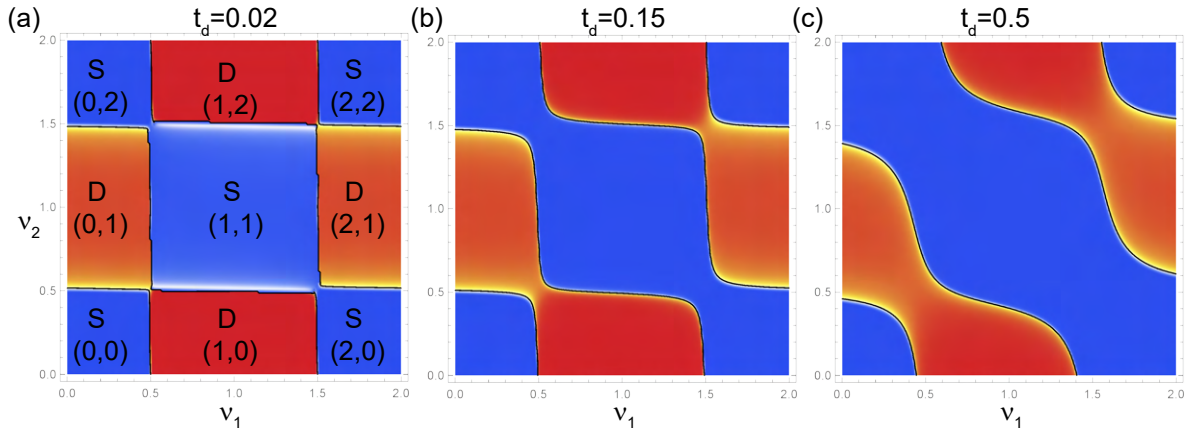
Figure 2.7: Model calculations of a DQD for different values of t_d. Color corresponds to the ground state, with blue being singlet and red doublet. The number on each charge sector corresponds to the number of electrons on the left and right QD respectively. Increasing the tunnel coupling leads to enhanced triple-points lines with evident curved features owing to the hybridization. (c) Further increase of t_c pushes the system towards the single QD limit, as for even higher t_d the two QDs would merge and only one set of parallel transition lines would be visible.

Vaguely speaking, t_d describes how strongly the wavefunctions of the two QDs hybridize. For $t_d \approx 0$ the system is effectively decoupled, where each QD one having its own ground state. This case is relevant for the study of DQD in double-nanowire Josephson junctions presented in Chapter 5. For finite t_d, hybridization plays a role and a common ground state describes the DQD system. Figure 2.7 shows calculations with negligible C_m and increasing t_d, showing that the triple points line and the curvature of the parity lines is enhanced, owing to the increased hybridization of the states. Interestingly, when each QD is

occupied by one electron, they form an exchange singlet ground state. Tuning the system to a high t_{d} (Fig. 2.7c) moves the system towards the single QD case.

2.3.4 Superconducting islands

The previous section investigates the Coulomb blockade effect in QDs formed in semiconductors. In this section we will focus on the consequences of making superconducting materials small enough, that they exhibit Coulomb blockade phenomena. Such objects are known as superconducting islands (SI). To grasp a more intuitive understanding of SIs, we follow the charge parabolas, which are then used to derive the electrochemical potentials of each level μ_{n}. Similarly to semiconductors, when an object is confined in three dimensions, energy parabolas dictate the number of electrons in the QD. A similar description can be used for SI with two main differences being the much smaller level spacing $\delta \mathrm{E}$ which is neglected (due to the much higher density of electrons in metals than semiconductors) and the presence of the superconducting gap Δ which acts as single-electron excitation and produces different SI regimes depending on the E_{c}, Δ relation. To formulate the above description, we use the Hamiltonian $H = H_{\mathrm{c}} + H_{\mathrm{BCS}}$, where H_{c} is given by Eq. 2.4, which describes the energy of a normal QD as a function of $E_{\mathrm{c}} = e^2/2C$ and the expectation value of electrons in the QD.

$$H_{\mathrm{c}} = E_{\mathrm{c}} \sum_n (n - n_{\mathrm{g}})^2 \tag{2.4}$$

The BCS Hamiltonian can be simplified by assuming that a single quasiparticle can occupy a state in Δ for odd number of electrons in the SI, while an addition of an extra electron leads to formation of a Cooper pair, minimizing the energy of the SI. This energy penalty for odd occupation accounts for the parity effect in superconducting islands and is given by Eq. 2.5.

$$H_{\mathrm{BCS}} = \begin{cases} \Delta & \mathrm{n : odd} \\ \\ 0 & \mathrm{n : even} \end{cases} \tag{2.5}$$

When superconducting islands are defined in semiconducting channels such as nanowires [13, 14, 28, 35, 36], sub-gap states with lower energy

than Δ are formed due to the semiconductor-superconductor hybridization. We name the lowest energy sub-gap state E_0.
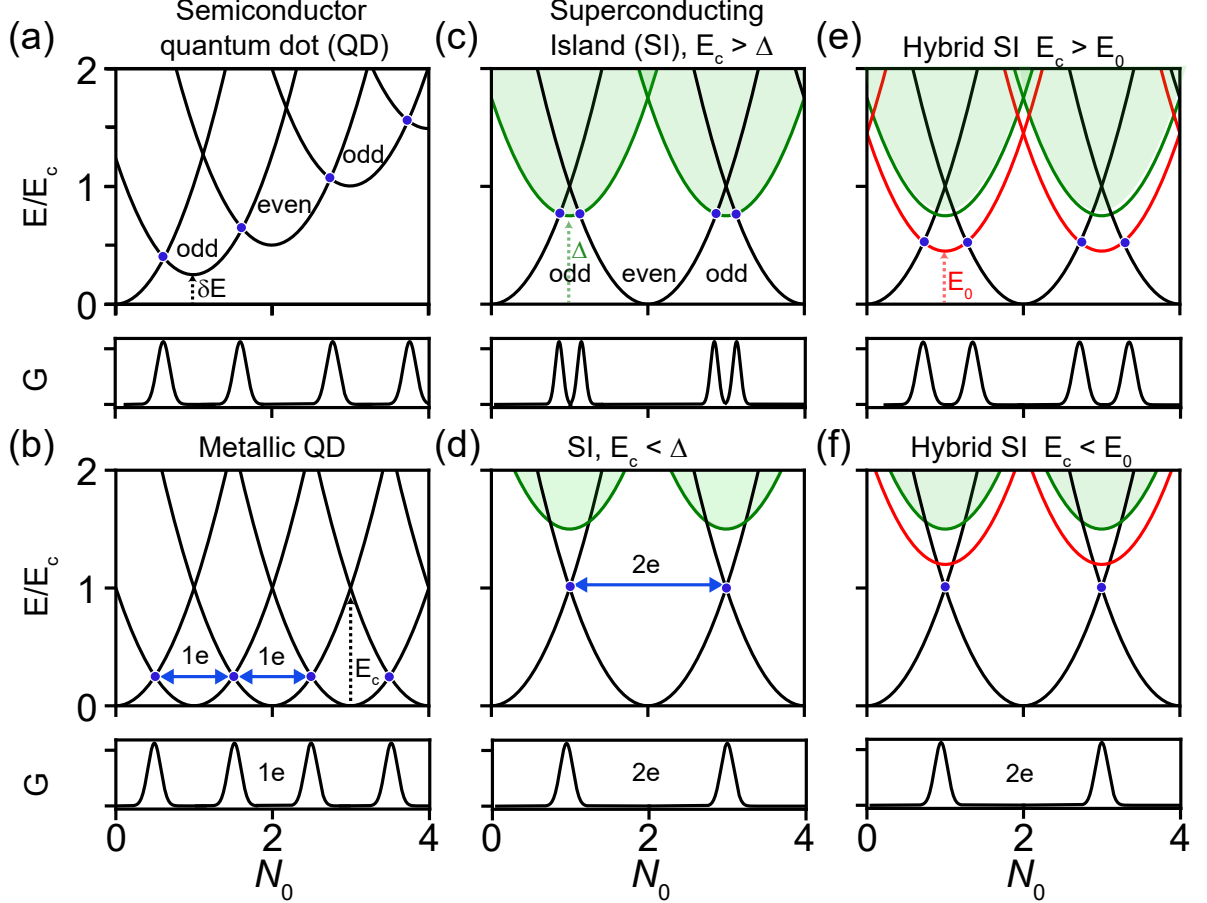
Figure 2.8: Calculated energy parabolas. (a) Energy as a function of QD occupation for a normal QD. The even-odd effect is formed due to the significant level spacing δE. Blue points represent charge degeneracies which cause conductance peaks. (b) Metallic QD with negligible δE yields a 1e periodic pattern. (c-d) Superconducting island energy dispersion using Eqs. 2.4,2.5 for $E_c > \Delta$ (c) yielding the even-odd effect and $E_c < \Delta$ (d) where 2e periodicity is observed. Excitations to Δ are shaded green. (e-f) Hybrid SI where a sub-gap state energy E_0 has been added by hand in the model. Below each energy diagram a zero-bias conductance plot is shown corresponding to each regime.

Figure 2.8 shows energy dispersion as a function of QD occupation for different types and regimes of Coulomb blockaded objects. Figure 2.8a presents a calculation of the energy parabolas for a QD with significant level spacing δE formed in a semiconductor. Due to the Pauli exclusion principle (also discussed in Section 2.3.1), only two electrons can occupy a single level, and therefore the parabola is raised by δE

18

when accessing a new level. If the level spacing is negligible, as is the case in metallic islands, then a 1e periodicity is retrieved, as illustrated in Fig. 2.8b. In a superconducting island [37,38] the gap Δ plays a role in the parity of the island, and Eq. 2.5 is added in the model. Figure 2.8c shows the case where $E_c > \Delta$ resulting in new charge degeneracies below the charging energy, causing an even-odd effect in SI. On the other hand, for $E_c < \Delta$ only Cooper pairs can be added in the island, and zero-bias transport is mediated via Andreev reflection. When a SI is defined in contact to a semiconducting channel, the proximity effect hybridizes the two materials and forms sub-gap states below Δ [13,14,27,28]. The lowest sub-gap state E_0 is illustrated with red in Fig. 2.8e,f and is added by hand in the model. Similarly to Fig. 2.8c,d if the sub-gap state energy is lower than E_c, single-electron transport is allowed through the SI.
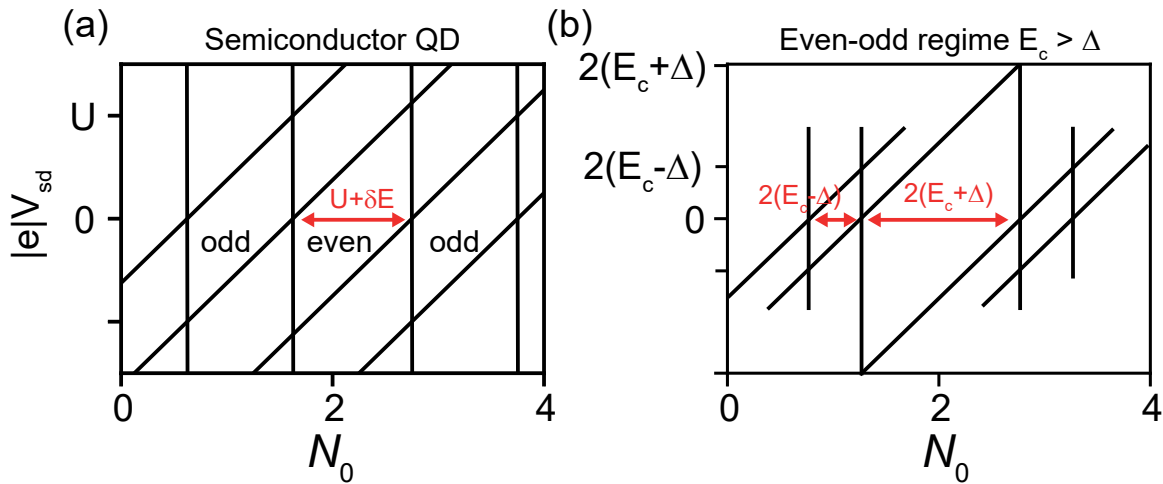
Figure 2.9: Calculated Coulomb diamonds for various QD regimes. Note that for the semiconducting QD we use the notation U=$2E_c = e^2/C$. (a) Normal QD Coulomb diamonds with even-odd structure owing to the level spacing δE. (b) Superconducting island in the even-odd regime where E_c=1, Δ=0.5 (a.u.). For simplicity, we assume the lever arm parameter $\alpha = 1$.

This picture can be linked to electrical transport of Coulomb blockaded objects. Examples of such are shown in Fig. 2.8 below each energy diagram. When the number of electrons is fixed, the system is in equilibrium and no current flows (zero conductance). On the other hand, when the device is tuned such that two parabolas are degenerate (blue circles), then charge fluctuations allow current to pass and conductance

peaks are recorded. Evidently, the spacing of the peaks is an indicator of the regime of the QD (e.g. even-odd or 1e).

Using the energy of the parabolas E_n, one can calculate the electrochemical potentials to add an electron n given n-1 electrons $\mu_n = E_n - E_{n-1}$ and plot the Coulomb diamonds for each regime. Examples of a normal QD and a SI in the even-odd regime are shown in Fig. 2.9. For the semiconducting QD, the height of the Coulomb diamonds is given by U for the odd ones and $U + \delta E$ for the even ones. For a SI in the even-odd regime $E_c > \Delta$, the height of the even diamonds is given by $2(E_c + \Delta)$, while the height of the odd diamonds by $2(E_c - \Delta)$. These tools are used in the following chapters to estimate E_c, Δ and δE from bias spectroscopy measurements.

2.3.5 Temperature dependence of the parity effect

The presence of E_0 dramatically affects the temperature dependence of the parity lines in a superconducting island. To describe that effect, we follow the model introduced in Higginbotham et al. [13]. The parity effect, shown in Fig. 2.8e, can be described in terms of the free energy difference between even and odd states [13]. This energy difference, $F_o - F_e = -k_B T \ln(\frac{Z_o}{Z_e})$, depends on the number of configurations involving even and odd number of quasiparticles $Z_{e,o} \propto e^{-E/k_B T}$.

The essence of these configurations is presented in Fig. 2.10, where the first terms of even and odd states are illustrated. Each configuration has a fixed number of Cooper pairs and quasiparticles. Access to configurations that involve populating E_0 or the continuum edge require energy that can be paid when the temperature is increased. For the even case, the first excited configuration requires breaking a Cooper pair (N $\rightarrow$ N-1) and populating the sub-gap state E_0 and the continuum edge Δ. Hence, the energy of this configuration is $E = E_0 + \Delta$. The next configurations involve populating the continuum edge with more quasiparticles. Similar logic is followed for the odd case, where the first configuration requires exciting the quasiparticle at the sub-gap state to the continuum edge ($E = \Delta$). The next configurations are created by breaking Cooper pairs and exciting quasiparticles to the sub-gap state energy and to the continuum edge.

20

For an aluminum island, the free energy equation can be rewritten as shown in Eq. 2.6,

$$F_{\mathrm{o}} - F_{\mathrm{e}} \approx -k_{\mathrm{B}}T \ln \tanh \left[2\rho_{\mathrm{Al}} V_{\mathrm{Al}} \Delta K_1 \left(\frac{\Delta}{k_{\mathrm{B}}T} \right) + \ln \coth \left(\frac{E_0}{2k_{\mathrm{B}}T} \right) \right] \tag{2.6}$$

where ρ_{Al} is the electron density of states of aluminum [37–39], V_{Al} is the volume of the aluminum island, $K_1(x)$ is the Bessel function of the second kind, Δ is the superconducting gap of the island and E_0 is the lowest energy sub-gap state originating from the superconductor-semiconductor proximity effect.
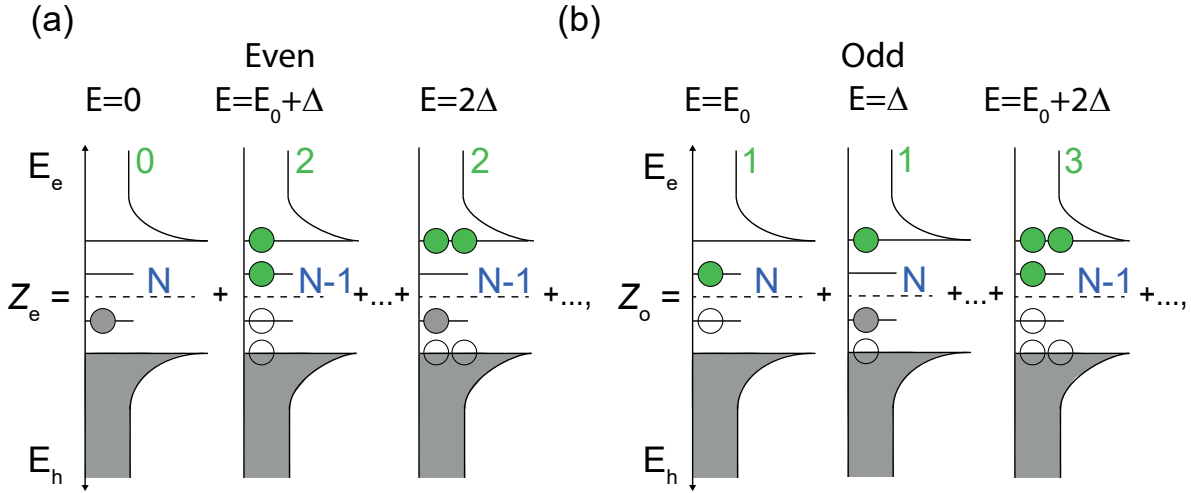
Figure 2.10: Schematics illustrating the ground state and first excited states for even (a) and odd (b) configurations $Z_{\mathrm{e,o}}$ of a SI with a sub-gap state E_0. Processes involve breaking a Cooper pair and exciting quasiparticles to the sub-gap state or to Δ (N→N-1) or exciting a quasiparticle from E_0 to Δ. Green numbers correspond to the total number of quasiparticle for a given configuration, while blue N, N-1 to the number of Cooper pairs in the SI.

Figure 2.11 shows the free energy difference $F_{\mathrm{e}} - F_{\mathrm{o}}$ as a function of temperature for a system with and without a sub-gap state. Assuming a sub-gap state -as in Fig. 2.8e, the normalized free energy difference commences at E_0/Δ and it starts to diminish at T_{sat} (saturation), when the excitations of quasiparticles to Δ become energetically favored, gradually making $Z_{\mathrm{e}} = Z_{\mathrm{o}}$. Larger values of Δ cause this transition to occur at larger temperatures, as the thermal energy required is increased. Absence of a sub-gap state produces a linear dependence of the free energy as a function of temperature, as seen in the blue line of Fig. 2.11. Fur-

ther use of this model is done in Chapter 6, where the free energy of a superconducting island coupled to double nanowires is studied.
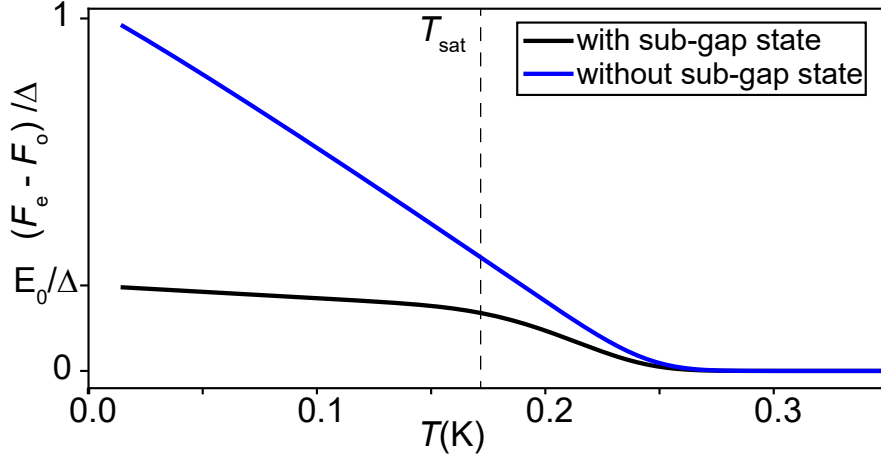
Figure 2.11: Calculation of the free energy difference $F_e - F_o$ as a function of temperature following Eq. 2.6 including a sub-gap state E_0 (black line) and without a sub-gap state (blue line).

2.4 Yu-Shiba-Rusinov physics

This section focuses on the physics of a superconductor in close proximity with a magnetic impurity. Similarly to screening of a spin in the Kondo ground state [40, 41], when a superconductor interacts with a magnetic impurity, such as an unpaired spin in a QD, an excited state involving the spin and a quasiparticle excited at Δ of the superconductor emerges [2–4]. For strong enough coupling Γ between the two objects, that state can become the ground state and cause a doublet to singlet $D \rightarrow S^{\text{YSR}}$ ground state transition [42, 43]. That transition process is illustrated in Fig. 2.12, where we plot the energy of the YSR state as a function of QD occupation n. Initially, at weak coupling Γ between the superconductor-QD system, the ground state is dependent on the number of electrons in the QD. Even number (0,2) correspond to S, while odd (1) to D. The red lines correspond to the first excited state, which for odd number of electrons is a S^{YSR} state[2]. Increasing Γ lowers the excitation energy, as the red lines are moving towards zero energy. For

---

[2]Note that YSR states are relevant in the $U \gg \Delta$ limit.
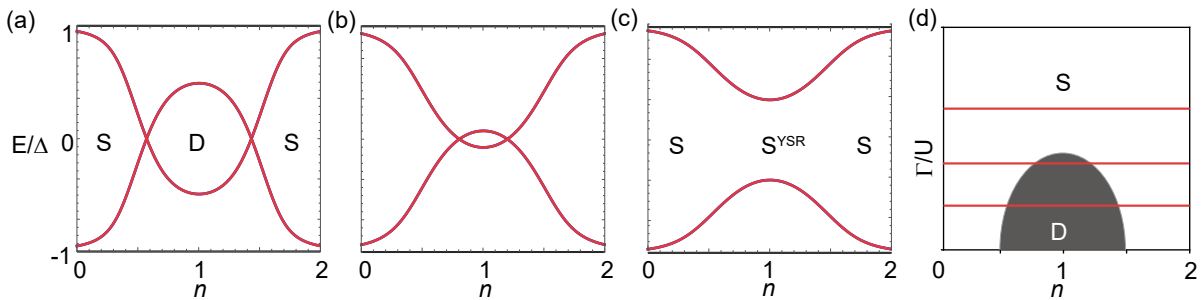
Figure 2.12: First excitation spectrum for a superconductor-quantum dot (S-QD) system as a function of QD occupation. (a) At weak coupling between the S-QD ground state transitions are observed as the excitations (red lines) are crossing zero energy, realizing ground state transitions. (b) Increasing coupling Γ shrinks the doublet parity lines. (c) High enough Γ causes a $D \rightarrow S^{YSR}$ transition. (d) Phase diagram sketch for different QD occupation showing three examples of Γ/U.

strong coupling[3] such as $\Gamma \sim U$, the S^{YSR} is energetically favorable and becomes the ground state of the system. Now the red line is corresponding to the excited D state. Figure 2.12d shows a phase diagram of Γ/U versus QD occupation n. For weak coupling, the trajectory tuning the QD crosses the doublet dome, causing a ground state transition $S \rightarrow D \rightarrow S$. Increasing Γ makes the doublet dome smaller, which effectively is quenched for strong enough coupling. Apart from monitoring the excited state evolution, such a transition can be observed via the supercurrent, as the current-phase relation is modified due to the ground state transition. This method is used in Chapter 5 to analyze the supercurrent of a DQD Josephson junction.

The above scenario involves grounded superconductors. However, for the case of small superconducting islands interacting with a QD, a new energy scale emerges which is its charging energy E_c [44]. The relation between E_c and Δ gives rise to a honeycomb-like charge stability diagram reminiscent of a normal DQD, but with significant differences. Figure 2.13 shows numerical renormalization group calculations of charge stability diagrams in different regimes, showing the evolution of the QD-SI system in the E_c/Δ plane [44]. The coupling between the QD and the SI is fixed. For weak E_c (case of a grounded superconductor), the ground state of the system is only tuned by the QD occupation; singlet for even (blue) and doublet for odd (red). Increasing the E_c/Δ

---

[3]Here and for normal QDs in the following chapters we use the notation $U=e^2/C=2E_c$.
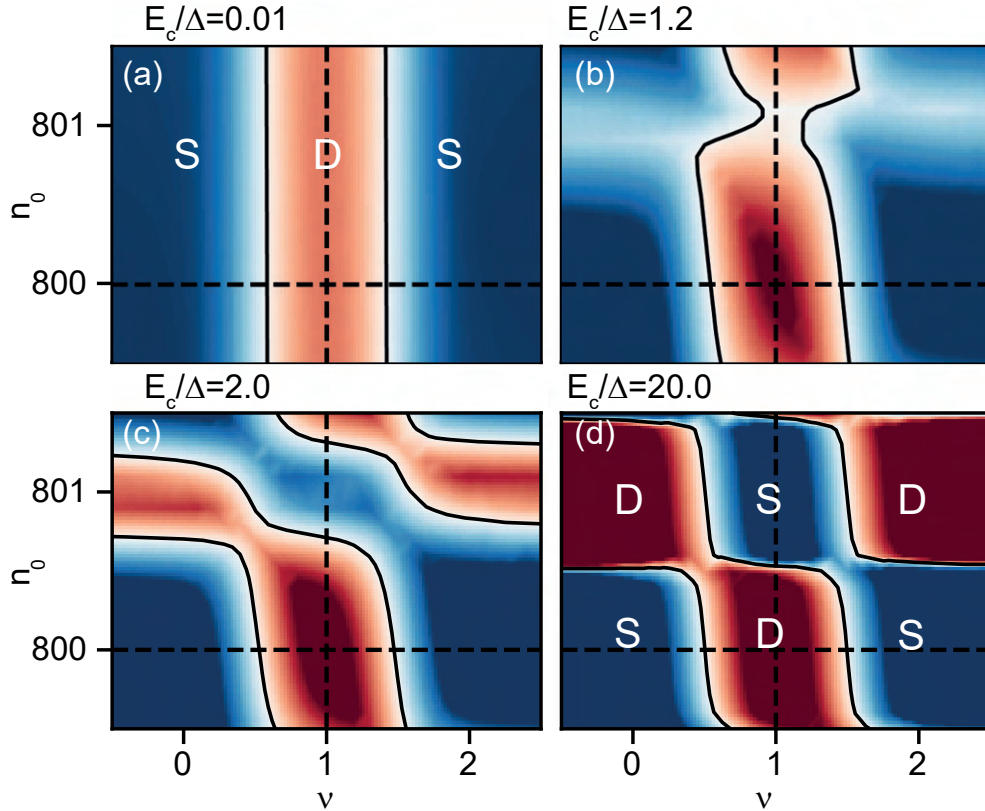
Figure 2.13: Numerical renormalization group calculations of the QD-SI system tuned in different E_c/Δ regimes as a function of QD (ν) and SI (n_0) occupation. Red color corresponds to doublet (D) ground state and blue to singlet (S). The figure is adapted from Ref. [44].

ratio, parity lines depend on the occupation of the SI too, as the SI parity is now important. Experimental data on this system as well as a more in depth clarification of the effects are presented in Chapter 8.

3

FABRICATION AND EXPERIMENTAL TECHNIQUES

This chapter covers the fundamental fabrication techniques that were used to develop the nanowire-based devices of this thesis. The experimental techniques are also presented, covering the different measurement setups (voltage bias, current bias) that were used.

3.1 Hybrid double-nanowire growth

In this thesis, our main focus is on a specific type of III-V materials, which have recently been developed by Kanne et al. [19]. These materials are InAs nanowires, which are grown in close proximity from one another in a Molecular Beam Epitaxy (MBE) chamber, forming a parallel-nanowire platform that can be utilized for different experiments. Before introducing the double-nanowire specifics, we can understand why we are interested in InAs nanowires in the first place.

InAs nanowires have been in the center of attention in the quantum transport community due to their quasi 1-D nature, spin-orbit coupling, and simplicity in device fabrication. The above reasons have made InAs nanowires one of the main candidates for quantum dot studies coupled to normal or superconducting reservoirs [32, 43], transmon applications [45, 46], Cooper-pair splitting geometries [17, 47] and testbeds for topological superconductivity, such as Majorana fermion proposals [7].

In addition, the possibility to grow an epitaxial layer of superconductor without breaking vacuum [19, 23, 48] has made such nanowires a prime choice for superconductor-semiconductor junction experiments, as a hard superconducting gap can be induced, minimizing quasiparticle poisoning in contrast to ex-situ superconductor deposition. Furthermore, recent proposals [8–10] employ parallel nanowire channels. Although a top-down approach of depositing two nanowires in close proximity has been investigated [17,18], the absence of an in-situ superconductor connecting the two nanowires is crucial. This has been one of the main motivations for creating *in-situ* parallel nanowires coupled with epitaxial superconducting shells.
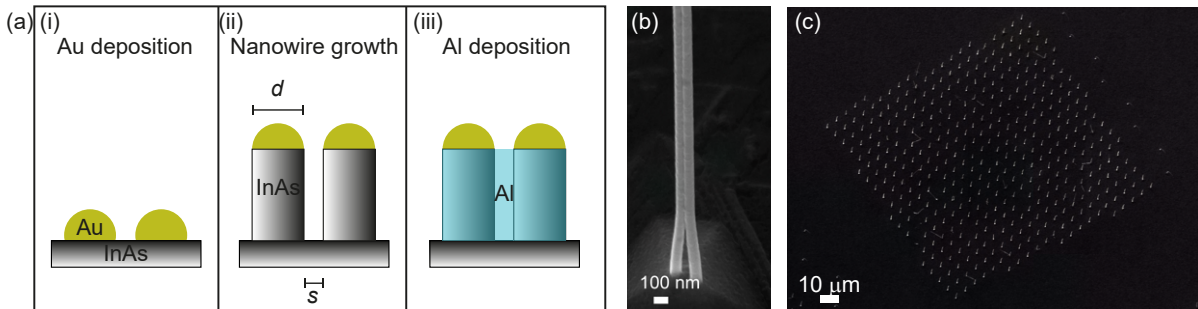
Figure 3.1: (a) Schematic illustration of the three basic steps of hybrid double-nanowire growth. (i) Initially, the gold particles are defined on an InAs substrate; (ii) InAs growth using the Vapor-Liquid-Solid (VLS) method in a MBE chamber forms the double nanowires (DNW). The diameter d of each wire is dependent to the size of the gold particle (with radius r_D) and the spacing s by the distance of the two particles (D_{Au}); (iii) *in-situ* aluminum deposition, bridging the two nanowires via the superconductor. (b) A Scanning Electron Microscopy (SEM) image of a hybrid double nanowire. (c) Large scale SEM image of the growth substrate showing a square pattern with many hybrid double nanowires.

The growth of hybrid double nanowires[1] is briefly introduced in Fig. 3.1a. Gold particles are deposited using electron beam lithography techniques on an InAs substrate, followed by loading the substrate in an MBE chamber. The diameter d of each wire and the spacing s between the two nanowires is dictated by the lithography pattern of the particles. The double-nanowire growth takes place in the MBE chamber and

---

[1]The double-nanowire growth was developed by collaborators T. Kanne, M. Marnauza and D. Olsteins.

the nanowires are defined. The final step is the *in-situ* aluminum deposition which occurs without breaking the vacuum between the InAs growth and the Al deposition. More information regarding the dpuble-nanowire growth and types is included in Chapter 4. In the samples we have used, the nominal Al thickness varies from 12 to 20 nm. Figure 3.1b shows an SEM example of a hybrid double nanowire. Fig. 3.1c shows a large-scale SEM image of the growth substrate, where a square pattern with nanowires is visible.
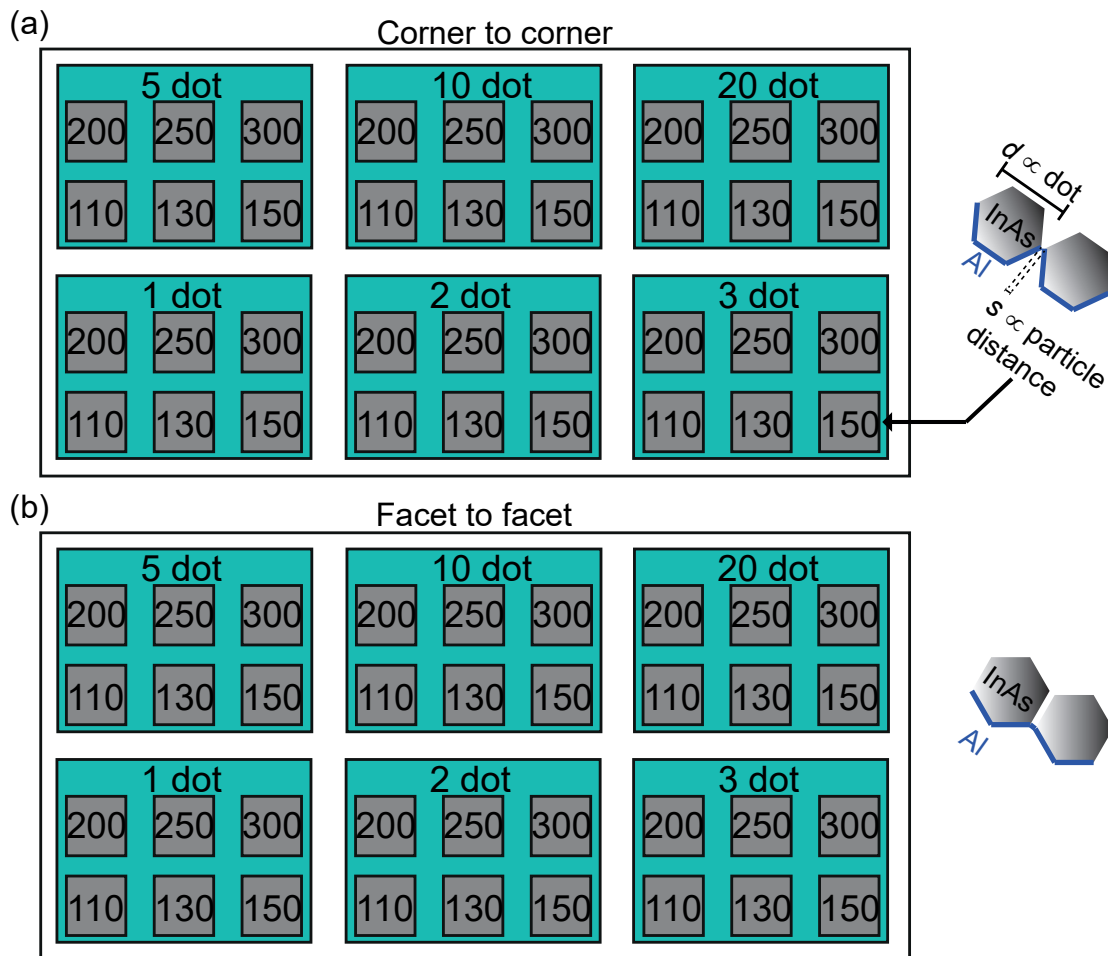
Figure 3.2: (a) Segment from the design map of the QDev939 double nanowire growth substrate. The double nanowires can be found in facet to facet (FF) or corner to corner (CC) configuration and their diameter is tuned by the number of dots. Each dot has six different spacings (in nm) of the gold particles, which are analogous to the spacing s of the two nanowires after growth.

The growth of hybrid double nanowires provides the versatility to choose from a variety of nanowire diameters d and spacings between

the nanowires s. Different combinations of the above are designed in the growth substrate, giving us the opportunity to choose the ideal s and d depending on the experiment. A map covering the different combinations of the above is shown in Fig. 3.2. The map is divided in a corner-to-corner and a facet-to-facet configuration, depending on the orientation of the gold particles. 1 dot wires correspond to diameters $d \approx 45$ nm, while the 20 dot to $d \approx 85$ nm. For small spacings (110-150 nm), the double nanowires tend to merge into one nanowire or they are connected, resulting in an unwanted geometry for the experiments of this thesis. On the other hand, for spacing larger than 200 nm, the double nanowires are growing separately and are ideally only connected through the aluminum shell. For the experiments presented in this thesis, 200-250 nm spacings in combination with the 10 dot and 20 dot sizes were mostly used.

3.2 Fabrication techniques

In order to create devices with double nanowires, the first step is to fabricate the "base chips", which are highly doped Si/SiO$_2$ 5x5 mm^2 substrates with patterned alignment marks and bonding pads. An example of a base chip is shown in Fig. 3.3a. The alignment marks (red dashed squares) are used to align all the next subsequent fabrication steps with respect to them. The big outer marks are used for the electron beam lithography (EBL) alignment, while the small marks in the center of the chip are used to align the SEM images of the nanowires on the design program. The other features are the bonding pads, which are exposed using ultraviolet (UV) lithography. The circular points are used to connect the chip with a daughterboard using aluminum bonds, and the lines towards the center of the chip are used to connect contacts and gates of the nanowire devices. The area enclosed in the cyan square is the device space, where nanowires are deposited. Taking a closer look, Fig. 3.3b shows an SEM image with deposited nanowires in a chip. Nanowires are deposited using a micromanipulator tool, where a 100 nm tungsten needle can be moved in X,Y and Z dimensions using an Eppendorf TransferMan-4r micromanipulation unit. We use the needle to slowly approach nanowires in the growth substrate, and break them from their stems. Due to Van der Waals forces, the nanowires

28

(a) Base chips

(b) Nanowire deposition

10 μm

(c) Adding nanowires on design

1 μm

(d) Nanowire etching

etched segments

1 μm
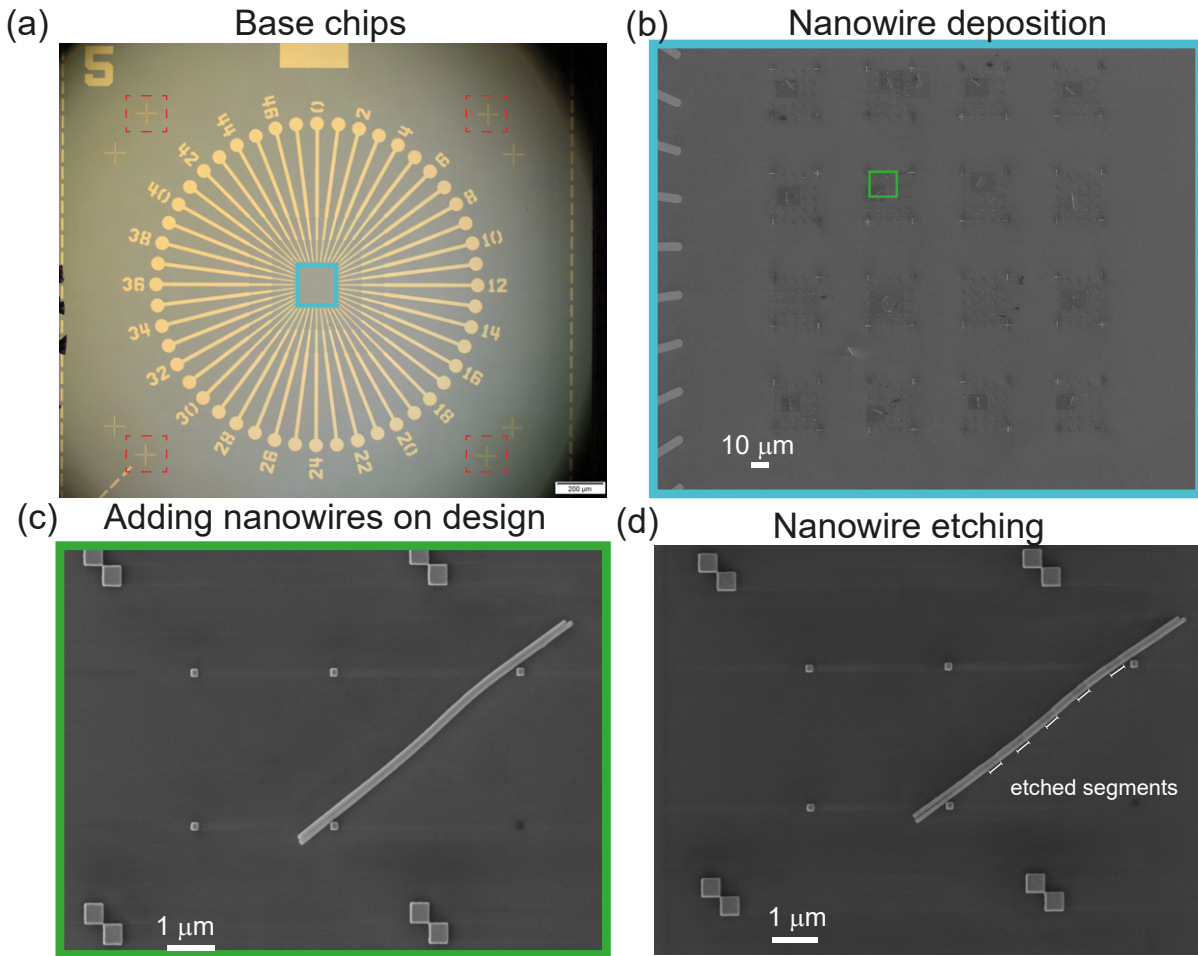
Figure 3.3: Fundamental fabrication steps of nanowire based devices. (a) Si/SiO_2 basechips are used as deposition substrates. The large lines are used to connect the electrodes of the device in the cyan square to the outer world by bonding them to an external motherboard. Dashed red squares are the alignment marks which are vital for the alignment of lithography steps. (b) SEM of the cyan square showing deposited double nanowires. (c) A zoom-in on a double nanowire. Such images are essential to align the nanowires on the design software. (d) Selectively etched aluminum from a double nanowire, white lines pinpoint the etched segments.

usually stick to the needle, and they can be deposited on the Si/SiO_2 substrate by sliding the needle on it. Double nanowires are challenging in comparison to single nanowires, as their orientation on the substrate is important (both nanowires should touch the substrate, as shown in Fig. 3.3c). To verify this and the general quality of the double nanowires (not broken, both lying on the substrate, connected by aluminum), we acquire zoomed-in SEM images, an example of such shown in Fig. 3.3c. The next fabrication step is to define the etch windows using EBL. To do
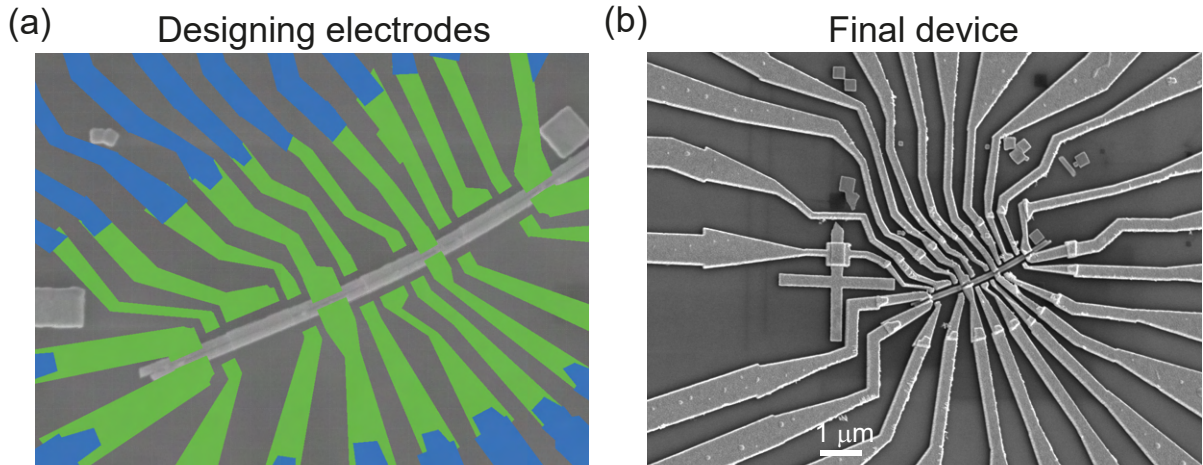
Figure 3.4: (a) Design of inner (green) and outer (blue) contacts and gates. Extended lines (blue) are designed if the inner contacts lithography is successful. (f) SEM of a working device after a complete fabrication process.

the etching we use aluminum etchant type D for 8 seconds. An example of a nanowire post-etching is shown in Fig. 3.3d. Typically the aluminum is overetched laterally by $\approx$ 50 nm. More details for the etching process can be found in the Appendix A.

The next step involves the fabrication of ohmic contacts and gate electrodes. Similarly to the etching process, gates and contacts are defined with EBL. An example of a design is shown in Fig. 3.3e. Typically the minimum distance between adjacent electrodes needs to be larger than 75 nm to achieve successful lift-off. In the more complex devices, such as superconducting islands in double nanowires, inner contacts are defined first in many devices, and the most successful ones are chosen after SEM inspection. Typically, the yield is approximately 60% due to misalignment of contacts or lift-off problems. This is shown in Fig. 3.4a, where green features are the inner contacts and blue ones are the outer contacts-which are exposed in a subsequent lithography step. After exposing the pattern and developing, argon milling is performed prior to the metallization without breaking the vacuum, using a standard recipe developed for InAs nanowires (see details in the Appendix A). The final device can be seen in Fig. 3.4b, where contacts and gates have been metallized by 5 nm Ti and 205 nm Au.

30

Hafnium oxide deposition

For the devices shown in Chapter 8, an additional fabrication step was necessary to fabricate gates that can be thinner and have a greater gate effect (top-gates) than normal side-gates shown in Fig. 3.3f. To do so, a dielectric HfO$_2$ layer needs to be deposited on top of the device before the top-gates. Figure 3.5 shows a nanowire device in three different fabrication steps; after aluminum etching and electrode deposition (Fig. 3.5a), after atomic layer deposition (ALD) covering the nanowires with an insulating HfO$_2$ layer (Fig. 3.5b), and the final device with top-gates covering the nanowire (Fig. 3.5c).
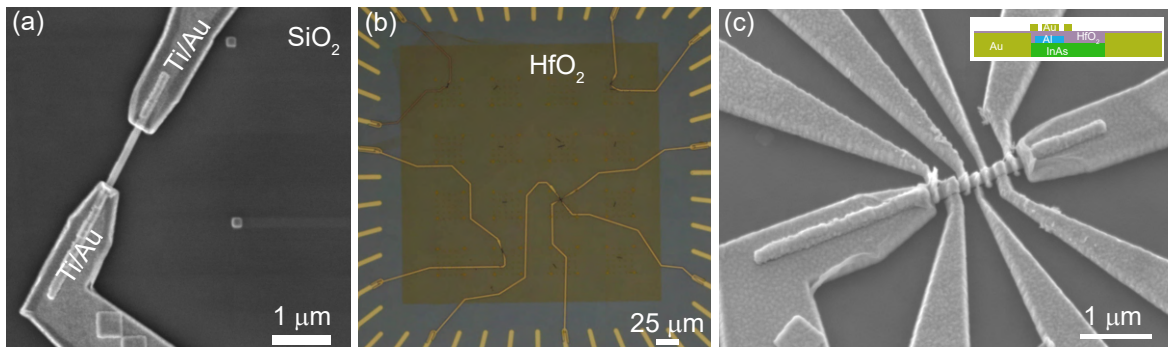
Figure 3.5: (a) InAs nanowire device deposited on a Si/SiO$_2$ substrate with Ti/Au evaporated contacts. (b) Atomic layer deposition (ALD) of an insulating layer ≈ 6 nm (HfO$_2$) covering the nanowires. (c) top-gates deposited on the nanowire to tune couplings between leads and islands. The goal is to form small quantum dots in the nanowire and form tunnel barriers. Inset shows a cross section schematic of a top-gated device.

Top-gates versus side-gates

The top-gates are usually much more effective compared to side-gates, as their lever arms are higher (due to the closer proximity to the nanowires). That allows faster and easier measurements, as nanowire segments are easier to pinch off, while side-gates would require much more negative voltages to pinch off a device. On the other hand, top-gates have the disadvantage that they require two additional fabrication steps, which can increase the risk of potential damage to the device during the fabrication process. Moreover, the deposition of the dielec-

tric usually creates more charge traps that can be activated during measurements when tuning the device, creating gate-induced switches, and overall a noisy device. In conclusion, side-gates show consistently less switchy behaviour, but with less tuning capability.

3.3 Bonding and loading

Devices were bonded using the in-house built daughterboards shown in Fig. 3.6a. Silver paint is used as an adhesive between the doped Si backside of the devices and the daughterboard cavity. Aluminum wire is used to connect the device's electrodes to the daughterboard. After bonding is complete, the sample is mounted on the motherboard on the puck, which can be then loaded in the dilution refrigerator, shown in Fig. 3.6c.
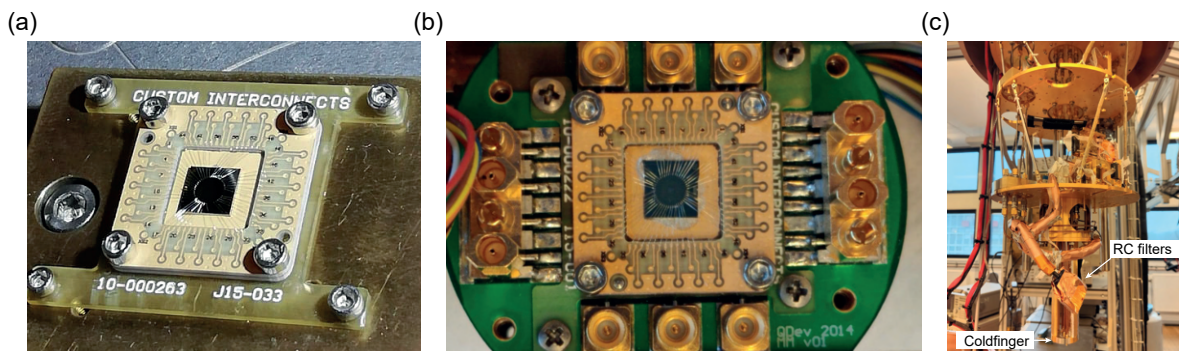
Figure 3.6: (a) Image of a final device on a chip glued on a daughterboard using a silver paint adhesive. Aluminum wires bond the electrodes designed in the chip to the daughterboard. (b) Daughterboard with a bonded device mounted in a puck which is loaded in a cryofree dilution refrigerator. A total of 48 DC lines with RC filters are used. (c) Photograph of the dilution refrigerator which is used throughout the experiments shown in this thesis. The picture was taken when the fridge was open during service.

3.4 Measurement setups

This section presents the different measurements setups that were used in this thesis. Two measurements setups were utilized. In order to study the density of states of a hybrid nanowire device, such as a superconductor coupled to a quantum dot, one can measure the differential conductance, which is a reference of the density of states, when the device
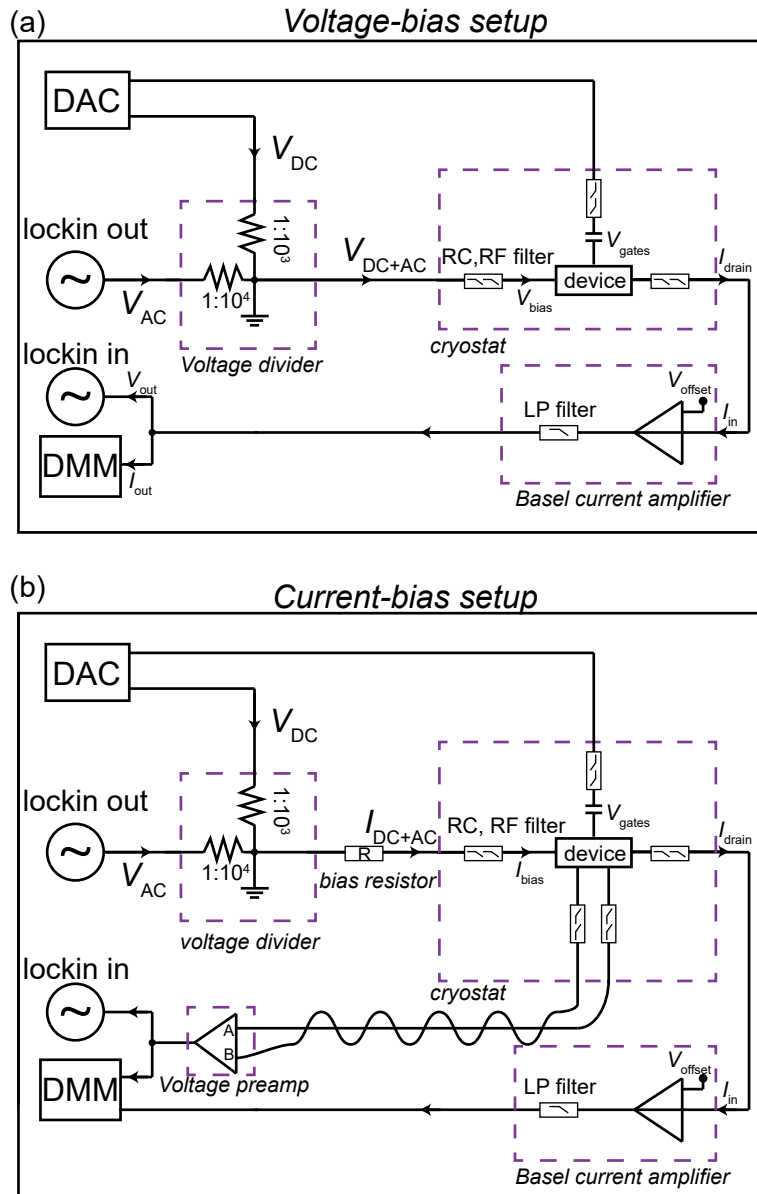
Figure 3.7: Measurement setups. (a) Schematic of the voltage-bias circuit used in the experiments. (b) Schematic of the current-bias circuit which was used in the Little-Parks experiment and the switching current measurements of the double-nanowire Josephson junctions experiment. The choice of the bias resistor varied from 8 kΩ to 2 GΩ depending on the experiment and the device resistance.

is tuned in the tunnelling regime. This two-terminal setup is known as voltage-biased and was mostly used to study bias spectroscopy of bound states and superconducting islands (see Chapters 5,6). In Josephson junctions devices and full-shell superconducting nanowires (see

Chapters 5,7), the voltage drop is not well defined as the resistance of such structures can be negligible. Therefore, an alternative four-terminal setup is utilized biasing the device with a current from an outer lead and measuring the voltage drop in two inner leads. This setup is known as current-biased. Figure 3.7 shows schematics of voltage-bias (a) and current-bias (b) setups that were used in this thesis.

For all the measurements conducted, SR830 lockins were used to apply AC excitations and measure the differential conductance signals. The DMMs were Agilent34401A, the current amplifier was a Basel I to V converter (SP983c) and the voltage preamplifier used in four-probe measurements was a "NF electronic instruments LI-75A low noise preamplifier". A 16 bit decaDAC was used to apply the DC source and gate voltages. Lastly, all fridge lines are filtered using RC filters (π + 2x(2 kΩ, 2.7 nF)) and RF filter (3xπ), which are mounted on the 30 mK plate.

4

VAPOR-LIQUID-SOLID HYBRID DOUBLE-NANOWIRE GROWTH AND CHARACTERIZATION

This chapter includes with more detail the growth and types of double-nanowire platforms that are utilized in Chapters 5,6,7. Two growth types are developed (I, II) which are optimized to create nanowires connected only via the superconductor (I), and nanowires at close proximity (II) to enhance interwire tunnelling. Initial measurements in double nanowires are presented, showing superconducting properties and quantum dot features.

4.1 Introduction

Attractive properties of InAs nanowires such as their quasi 1-D nature, spin-orbit coupling and device fabrication feasibility have drawn the attention of the quantum transport community. These properties have made InAs nanowires one of the main candidates for qubit devices [49],

Cooper-pair splitting geometries [17, 18, 50], Yu-Shiba-Rusinov physics experiments [43, 51] and testbeds for topological superconductivity. Single nanowires covered by epitaxial aluminum are well established and studied in a plethora of experiments [23, 48], however recent theoretical proposals which predict exotic phenomena require parallel nanowire systems [8–10]. Instead of following a top-down approach to create such parallel nanowires [17, 18], we follow a novel strategy where the two nanowires are grown *in-situ* in close proximity and superconductors are deposited on them without breaking vacuum [19]. This technique has strong advantages as it allows the double nanowires to be bridged by the superconductor and reduce poisoning effects on the superconductor.
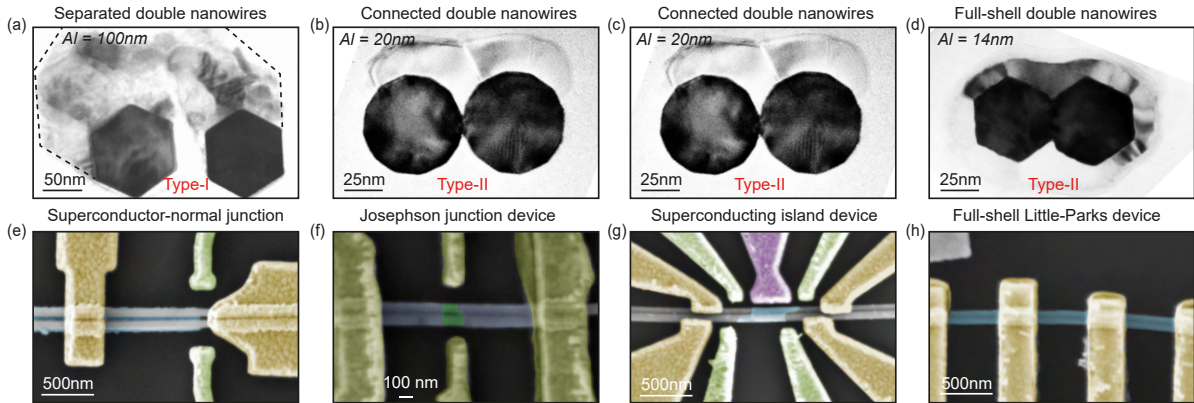
Figure 4.1: Double-nanowire configurations and device layouts. (a-d) Transmission electron micrographs (TEM) of nanowire cross sections, where pairs of parallel InAs nanowires in four different configurations are coated with an Al film, either on one side (a-c) or around the entire pair as a full shell (d). (e-h) Scanning electron microscopy (SEM) images of devices; gated normal-superconductor junction (e), double-nanowire Josephson junction (f), superconducting island with four independent contacts and several sidegates (g), and double nanowire with a full shell superconducting coating (h). Blue false-color represents the aluminum coating, while yellow purple and light green the leads and gates electrodes.

Figure 4.1 shows examples of double nanowire (DNW) cross sections and devices that have been implemented.[Throughout the experiments, we have used two type of DNW. Type-I are more rigid and nominally only connected through the aluminum, while Type-II are thinner nanowires which may merge during growth resulting in stronger interwire tunnelling. Figure 4.1a shows a cross section of a Type-I DNW. The aluminum covers half the facets of the nanowires and has nomi-

nal thickness of 100 nm. Figure 4.1e shows a normal-superconductor junction device utilizing DNWs from the above growth where the aluminum has been selectively etched to form such a junction. Figure 4.1b shows a different DNW growth with Type-II nanowires where again half the facets are covered by aluminum and the nominal aluminum thickness is 20 nm. Figures 4.1f,g show two device geometries, where a Josephson junction and a superconducting island (SI) have been formed in DNWs. Transport measurements of such junctions are included in detail in Chapters 5,6. Using a different growth synthesis of DNWs, a full shell of aluminum can be achieved, covering both InAs nanowires. A TEM of such a DNW is shown in Fig. 4.1d. Such nanowires have been used in full-shell experiments, where Little-Parks oscillations are probed in the nanowires (see Chapter 7).

4.2 Growth of double nanowires

In this section we will look into the different types (I,II) of double nanowire growth. Each type has fundamental properties which make them ideal for certain experiments. Typically, type-I DNWs are separated and only merged by the superconductor, making them ideal candidates for experiments where the tunneling between the two nanowires should be minimal. On the other hand, type-II DNWs are clamped together after the growth process due to van der Waals forces, enhancing the tunneling through the nanowires and possibly non-local effects such as crossed Andreev reflection (CAR). However, more parameters such as the gold catalyst distance D_{Au} and the gold catalysts disc radii r_D are essential as they influence the final distance of the two nanowires and their diameters.

Type-I double nanowires

Figure 4.2 illustrates different type-I DNWs grown at various diameters d (corresponding to the gold catalysts radii r_D) and at fixed catalyst spacing D_{Au}. Figure 4.2c shows SEM images which are obtained at an angle opposite to the Al deposition direction in order to highlight the morphology of the nanowires. The top row focuses on the base of the nanowires, while the bottom row reveals the shading effects on the
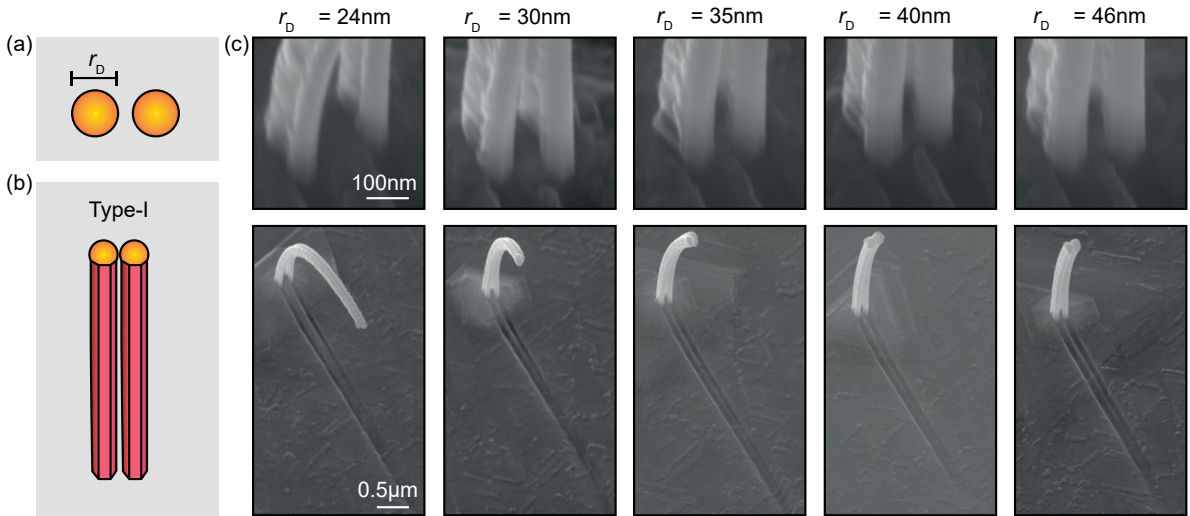
Figure 4.2: InAs nanowire pairs grown utilizing the type I approach. (a) Initial Au particle configuration. (b) Schematic of double nanowire with a constant inter-nanowire separation. (c) SEM micrographs of nanowires grown with a center to center Au particle separation of $D_{Au} = 160$ nm and different Au disc radii r_D. Top-row micrographs show the bottom part of the nanowire pairs and the lower row shows the full nanowire system and shadows cast on the substrate during metal evaporation.

substrate. From Figure 4.2, pronounced thickness-dependent bending of the nanowires is observed as seen also for single nanowires [23, 52]. By examining the metal deposited on the substrate, it appears that all semiconductor nanowires grow separately and in a later stage connect via the Al film, in accordance with TEM studies of cross-sections such as Figure 4.1a. For these specific growth conditions, small diameters result in less rigid nanowires which tend merge near the top, while thicker ones with diameters larger than 80 nm produce a fixed spacing between the nanowires along the whole length. The latter ones follow the type-I characteristics.

Type-II double nanowires

In order to create type-II nanowires, the growth parameters are adjusted to form thinner and longer nanowires. This combination of parameters promote van der Waals forces and lead to clamped nanowires. Specifically, to achieve smaller nanowire diameter the V/III flux ratio is increased (see Kanne et al. [19] for growth details). Double nanowires following the above technique are shown in Fig. 4.3. For small gold
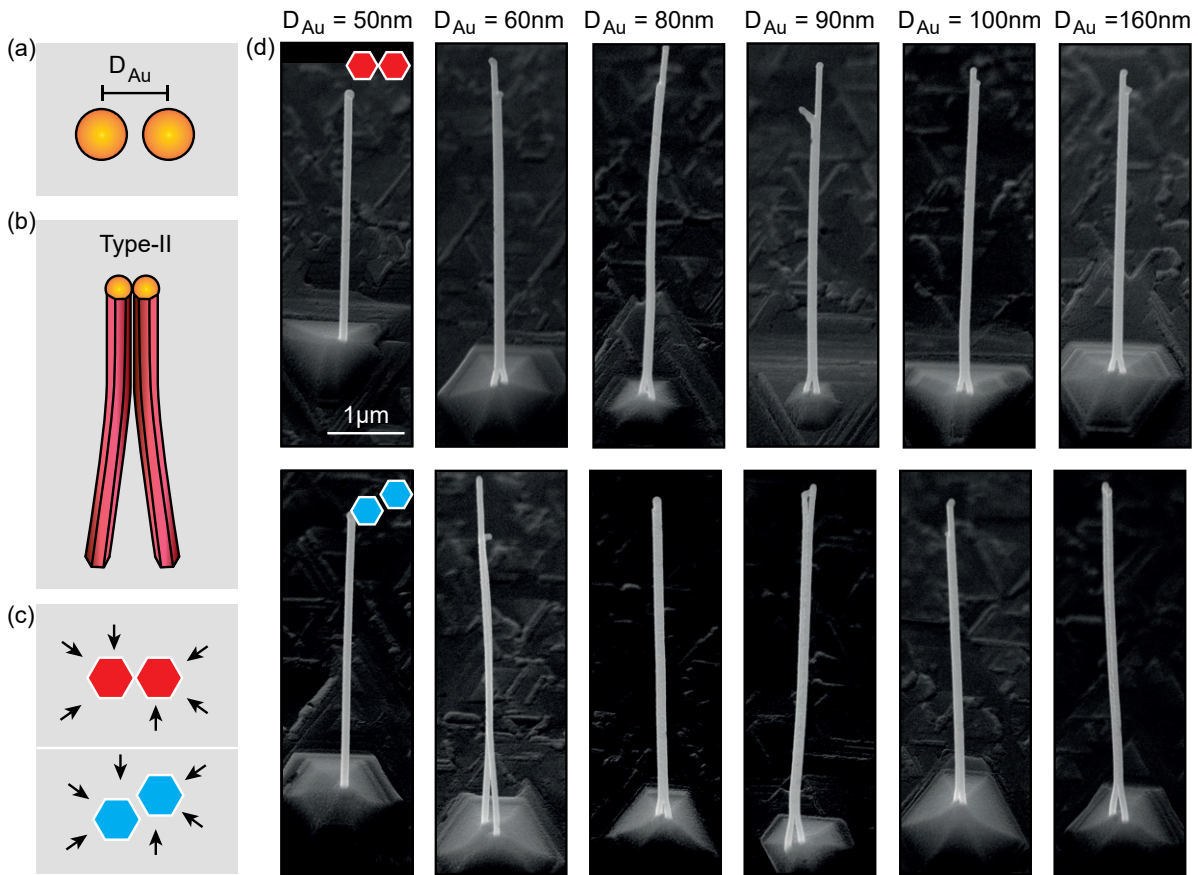
Figure 4.3: Parallel InAs nanowires utilizing the type II growth approach with a full shell of Al. (a) The initial Au particle disk separation (D_{Au}). (b) The type-II merging scheme. (c) Top-view schematic of a corner-to-corner (red) and a facet-to-facet (blue) configurations with a ~ 27 nm full Al shell resulting from six depositions perpendicular to nanowire facets. (d) SEM micrographs of nanowire pairs in the corner-to-corner and facet-to-facet configurations for Au particles formed by one single electron beam exposure and a center to center particle separation according to the text above the micrographs. The scales are all the same and noted in the first micrograph.

particle separation D_{Au} the nanowires merge into a single crystal as seen in the left panel of Fig. 4.3d. Larger distance makes the DNWs well defined. Figure 4.3c illustrates the two different DNWs configurations that are designed which the corner-to-corner (red) and facet-to-facet (blue). The yielded nanowires have diameters of ~ 50 nm for Au droplets with $r_D \sim 24$ nm and ~ 130 nm for $r_D \sim 100$ nm.

4.3   Electrical transport characterization

Electrical transport characterization of the DNWs is essential in order to study the properties of these novel structures and compare with known results in single InAs nanowires. Here, we focus on low-temperature transport measurements of two different types of devices in the quantum regime. The objective is to demonstrate that decoupled DNWs and multi-terminal device functionalities can be achieved. Older experiments on parallel nanowires have employed a top-down approach, where individual nanowires were pushed together on a substrate [17, 18]. In contrast, we transferred ready-made DNWs from the growth substrate to the pre-patterned substrates using a micromanipulator under an optical microscope.

The first example is shown in Fig. 4.4a where the 100 nm thick Al has been selectively etched and the double nanowire is contacted in two ends forming a normal (N)- superconductor (S) junction (see also SEM in Fig. 4.1e). Two sidegates have been defined to tune the carrier density of the semiconductors, effectively forming a quantum dot on each nanowire. Figure 4.4b shows a zero-bias differential conductance G map as a function of the two gates showing two set of parallel lines. Each set of lines represent charge degeneracies of a QD, with the vertical-like lines corresponding to the QD_1 tuned by V_{g1} and the horizontal-like lines corresponding to QD_2 tuned by V_{g2}. The two QDs have weak inter-dot coupling, judging from the absence of avoided crossing near the degeneracies of both QDs. To study the superconducting properties of the device, bias spectroscopy measurements are performed. Figure 4.4b,c shows bias spectroscopy measurements tuning QD_1 and QD_2 respectively. These measurements follow the trajectories of the dashed lines in Fig. 4.4a. For both QDs clear signs of tunneling via the superconducting coherence peaks are observed at eV_{sd}=200 μV, consistent with the superconducting gap of aluminum. Furthermore, signs of Yu-Shiba-Rusinov physics are observed, as especially QD_1 reflects sub-gap states in different coupling regimes [42, 43, 53].

The second example is sketched in Fig. 4.4e, where a superconducting island is defined in a DNW and each end of the nanowires are probed, similar to the SEM shown in Fig. 4.1g. In this experiment the goal is to investigate if a superconducting island could be realized
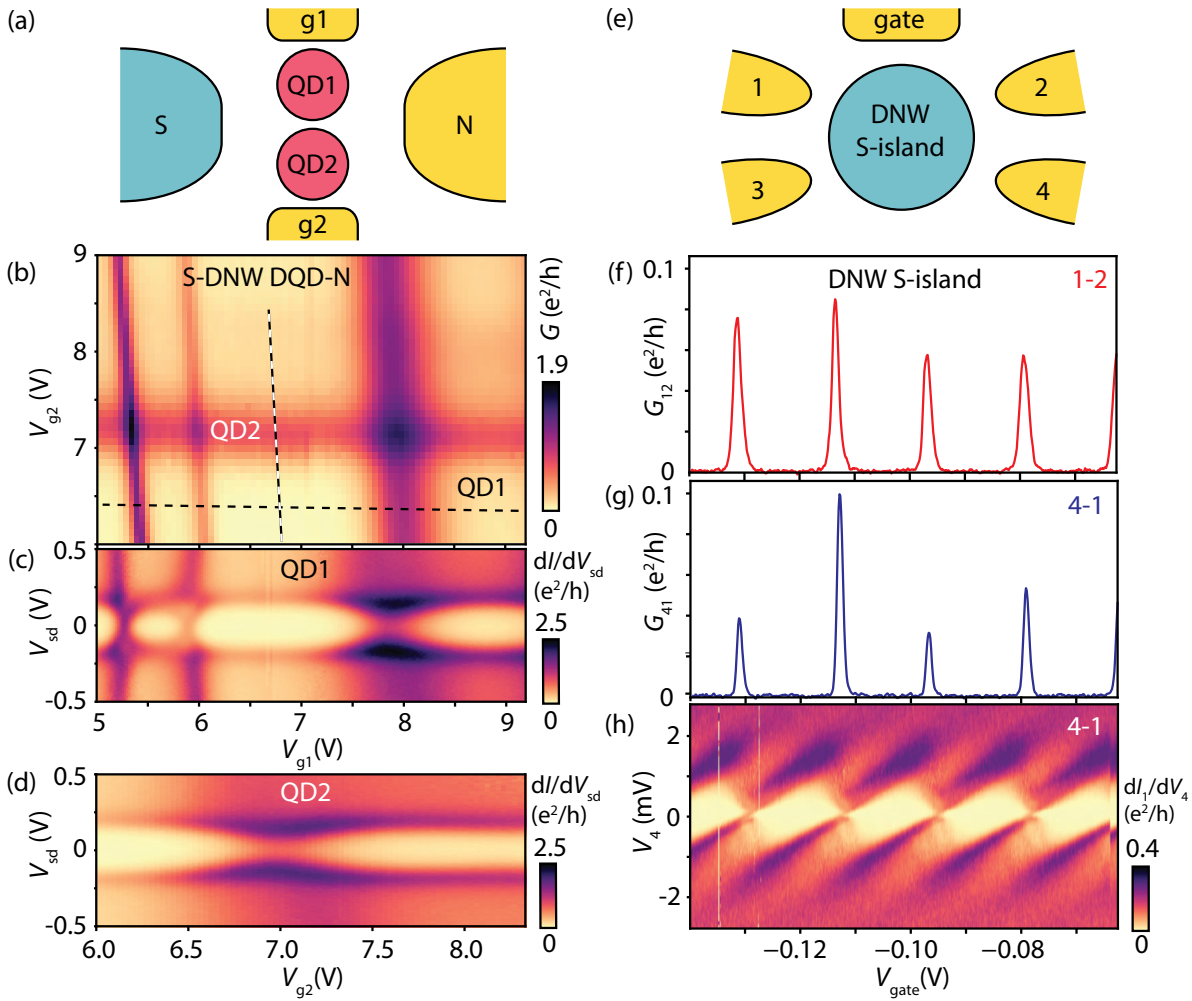
Figure 4.4: Electrical transport measurements of two hybrid double nanowire devices. (a) Schematic of a gated superconductor (S)-parallel double quantum dot (QD)-normal (N) device defined in a DNW. (b) Linear conductance G versus side gate voltages V_{g1} and V_{g2}. The nearly horizontal and vertical conductance lines reveal the transport resonance conditions for the two QDs controlled by the respective gates. (c-d) Differential conductance dI/dV_{sd} versus bias V_{sd} and gate V_g of QD1 (QD2) along the horizontal (vertical) dashed lines in (b). The measurements are a combination of both g1 and g2 but only one gate voltage is plotted on each measurement. The maps show that both quantum dots are coupled to a common superconducting lead (gap $\Delta \sim 0.2$ meV). A small gate shift has occurred between measurement (b) and (c,d). (e) Schematic of a S-DNW island with independent NW leads. The device geometry is similar to Fig. 4.1(g)). (f-g) Linear conductance G versus plunger gate V_{gate}. The plots show Coulomb blockade behavior for two pairs of electrodes, i.e. upper nanowire (1-2) and interwire (4-1) hybrid nanowire transport. (h) Bias spectroscopy showing Coulomb blockade diamonds related to transport through the S-island via leads 4-1. All measurements were performed at 30 mK.

and probed by different lead combinations. Figure 4.4f,g shows two examples of zero-bias gate traces using different two-terminal combinations. The measurements show clear Coulomb blockade features, and the peaks are found at the same gate values for both combinations, showing that the same object is probed by different lead combinations. Figure 4.4h shows an example of bias spectroscopy revealing the Coulomb diamonds of the superconducting island. Superconducting islands in DNWs are presented in detail in Chapter 6.

4.4 Outlook

This chapter showcased new possibilities for realisation of quantum devices using in-situ grown double nanowires. These advancements can aid in the pursue of topological effects in hybrid nanowire systems [8–10]. Furthermore, extended structures can be realized and some examples are shown in Fig. 4.5. Nanowires can be partially shadowed by a "mask" nanowire in order to create in-situ NS junctions preventing the use of wet etch techniques. Finally, more complex structures shown in Fig. 4.5(c-f) have been realized, where triple nanowire geometries and nanowire fences are shown. Such geometries can be utilized for multi-probe experiments or SQUID designs and in arrays of QDs experiments.
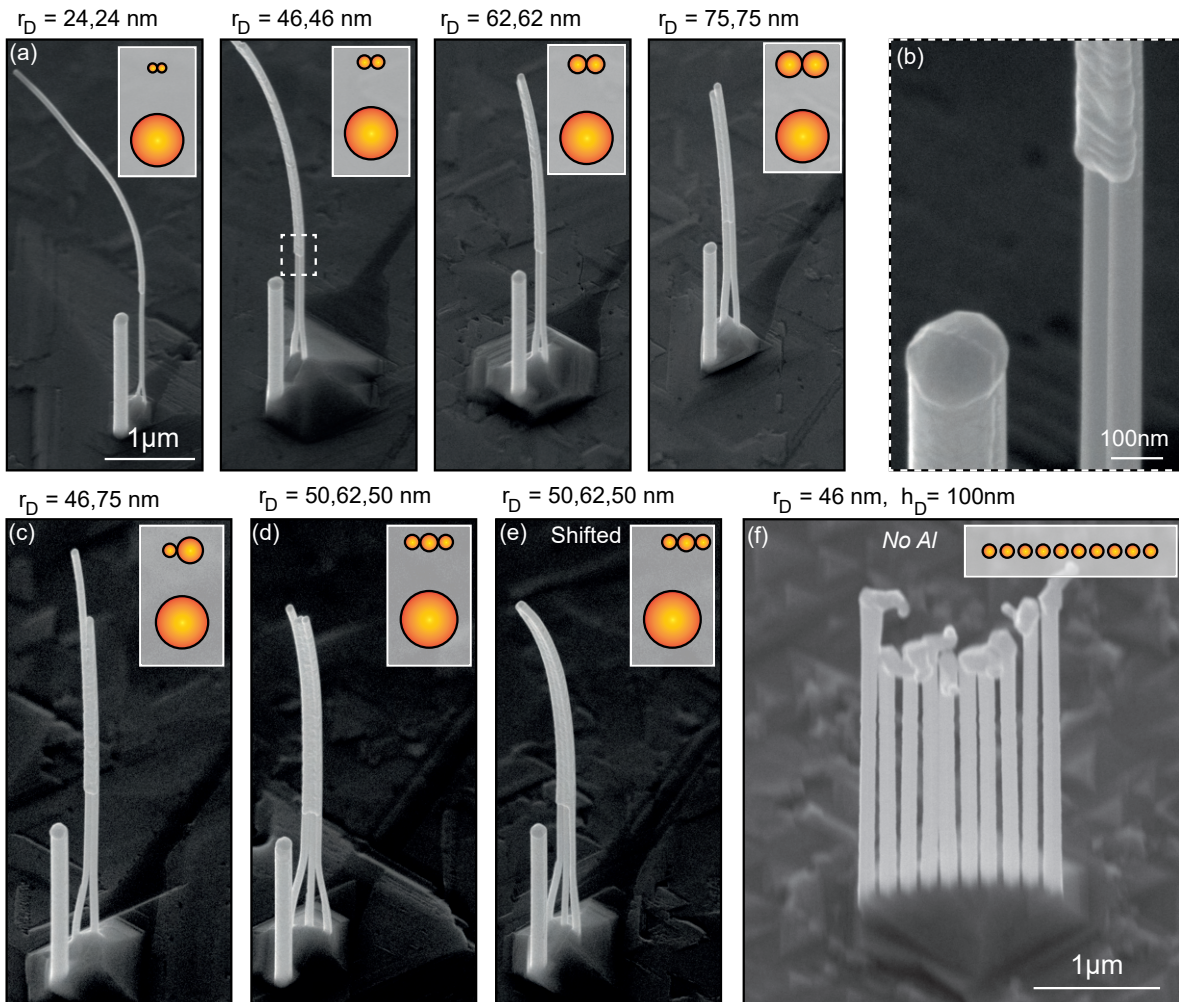
Figure 4.5: SEM micrographs of parallel nanowires in complex configurations. All nanowires were grown on the same wafer and all with ~ 20nm Al (except panel f). (a) In-situ shadowed parallel nanowires with varied dimensionality formed by different Au partices sizes. (b) Zoom on the second panel in (a). The sharp shadow junction is visible as well as the rounded nanowires obtained by tuning the growth parameters. (c) Parallel nanowire pair with different diameters. (d) Three nanowires merged around the center nanowire that has an increasing diameter. (e) Three nanowire bundle similar to (d), however shifted to ensure that one nanowire is not shadowed. (f) Linear array of 10 parallel nanowires without metal coating.

43

5

JOSEPHSON JUNCTIONS IN DOUBLE NANOWIRES BRIDGED BY IN-SITU DEPOSITED SUPERCONDUCTORS

In this chapter we characterize parallel double quantum dot Josephson junctions based on closely-spaced double nanowires bridged by in-situ deposited superconductors. The parallel double dot behavior occurs despite the proximity of the two nanowires and the potential risk of nanowire clamping during growth. By tuning the charge filling and lead couplings, we map out the parallel double quantum dot Yu-Shiba-Rusinov phase diagram. Our quasi-independent two-wire hybrids show promise for the realization of exotic topological phases.

5.1 Introduction

Double Rashba-nanowires bridged by superconductors are at the center of proposals for qubits [49], coupled subgap states [55] and exotic

topological superconducting phases based on Majorana zero modes (MZMs) [8–10, 56–66]. Researchers have theorized on the existence of a topological Kondo phase in such wires when the bridging superconductor is in Coulomb blockade [9, 10, 65, 67] and, more recently, described a device hosting parafermions [8]. Realization of these proposals should benefit from material science developments resulting in improved nanowire/superconductor interfaces with low quasiparticle poisoning rates [13, 14, 68].

These clean interfaces have been used in the pursuit of MZMs in single nanowires [12, 14] and, more recently, for coupling single and serial quantum dots (QDs) defined on single nanowires to superconductors to realize one and two-impurity Yu-Shiba-Rusinov (YSR) models [69–73]. YSR states, belonging to the class of Andreev bound states [15, 24, 42, 43, 51, 53, 70–72, 74–80], arise in the limit of large Coulomb charging energy, $U > \Delta$, as a result of the virtual excitation of a quasiparticle into the edge of the superconducting gap [81, 82]. This quasiparticle can exchange-fluctuate with a localized spin in the QD, and if the exchange coupling is strong (i.e., when the Kondo temperature, T_K, is larger than $\sim 0.3\Delta$), the ground state (GS) changes from a doublet to a singlet [83]. In Josephson junctions (JJs), this induces a π-0 phase-shift change in the superconducting phase difference [32, 33, 69, 70, 84–98].

Devices which use pairs of QDs placed in a parallel configuration [99–101] and coupled to common superconducting leads have been extensively studied with the purpose of producing entangled electron states through Cooper pair splitting [17, 18, 47, 102]. However, the behaviour of the switching current, I_{sw}, in the presence of YSR screening [51, 70, 103] in parallel double QDs remains to be investigated.

In this work, we characterize superconductivity in closely-spaced pairs of InAs nanowires bridged by a thin epitaxial superconducting aluminum film deposited in-situ [19]. To do so, we fabricate two side-by-side JJs out of one pair of nanowires and demonstrate that each nanowire hosts a single QD, through which supercurrent flows. From the charge stability diagram and magnetic field measurements, we establish that the interwire tunnelling at the junction is negligible with an upper bound of $\sim 50~\mu eV$. The YSR physics is analyzed through the gate dependence of the linear conductance and I_{sw}, where we find that

the common superconducting leads screen *individually* each QD, hinting at individual YSR clouds instead of a single one extending over the two QDs. We furthermore show indications of supercurrent interference when the ground-state parities of the QDs are different, reminiscent of a superconducting quantum interference device (SQUID) at zero magnetic field.

The chapter is structured in sections. Initially, we introduce the YSR double QD phase diagram and measurements of two double QD shells in different coupling regimes are presented establishing weak interdot coupling. Then, we show signatures of interference between the supercurrents flowing through each junction and we demonstrate the YSR screening evolution of I_{sw}. Finally, we present our conclusions and provide perspectives of our work.

5.2 Characterization of the parallel quantum-dot Josephson junction

In this section, we outline the device layout and demonstrate the Josephson effect and weak interdot tunnelling in Device 1. Data from an additional device (Device 2) is shown in Appendix B.

Figure 5.1a shows a falsely-colored scanning electron microscopy (SEM) image of Device 1. Two 80-nm InAs nanowires (in green), grown close to each other in a molecular beam epitaxy chamber, and covered each on three of its facets by an in-situ deposited 17 nm-thick layer of aluminum (in blue) [19], are individually picked with a micromanipulator and deposited on a Si/SiOx substrate with an oxide thickness of 275 nm. A resist mask is defined by electron beam lithography to selectively etch Al using the commercial etchant Transene-D, creating a parallel double JJ with ≈ 100 nm-wide bare sections of the two nanowires as weak links. Ti/Au 5 nm/250 nm-thick contacts and individual nanowire side-gates are deposited after a subsequent lithography step. Prior to the metal deposition step and without breaking vacuum, the Al native oxide is removed by argon milling to establish a good contact between Ti/Au and Al. The devices are measured in a dilution refrigerator at base temperature $T = 30$ mK.

QDs are formed when the two nanowires are brought near depletion with the use of the individual side-gate voltages, V_{gL} and V_{gR}. The side gates are also used as plunger gates of the QDs. A global back-
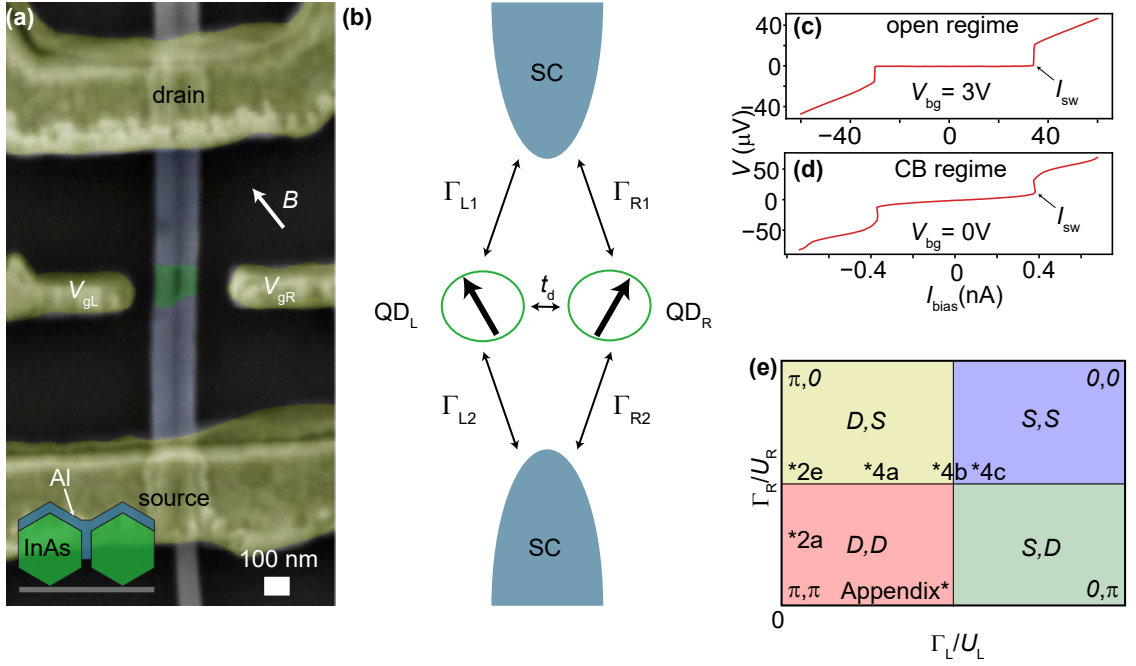
Figure 5.1: (a) Scanning electron micrograph of Device 1. Two nanowires with common superconducting leads form two parallel Josephson junctions. Side-by-side quantum dots serve as weak links for each JJ. The direction of an external in-plane magnetic field, B, when applied, is indicated by an arrow and has an angle of $45°$ with the device. In inset, a schematic cross-section of the double nanowire is shown, indicating facets of the nanowires covered by Al at the leads. (b) Sketch of the two side QDs coupled to two superconducting leads. Interdot tunnel coupling, t_d, may be present. The GS parity of the left (L) and right (R) QDs is changed by tuning their level positions, ϵ_L and ϵ_R, or by increasing the total tunnelling rates of each QD to the leads, $\Gamma_L = \Gamma_{L1} + \Gamma_{L2}$ and $\Gamma_R = \Gamma_{R1} + \Gamma_{R2}$. (c,d) $I_{bias} - V$ curves measured at $V_{bg} = 3\,\mathrm{V}$ and $V_{bg} = 0\,\mathrm{V}$ showing switching current, I_{sw}, in the open and in the Coulomb blockaded regimes, respectively. I_{bias} is swept from negative to positive. (e) Sketch of the GS phase diagram depending on the tunnelling rates Γ_i ($i =$L,R) between the leads and the two QDs, when $t_d = 0$ and each QD has an unpaired electron. D stands for doublet, and S for singlet. The expected phase-shift in the Josephson current-phase relationship of each QD JJ, 0 or π, is indicated. The qualitative Γ_L, Γ_R positions of different shells from Figs. 5.2, 5.4 and Appendix B (Device 2) are indicated by asterisks.

gate V_{bg} is used to tune the coupling between the contacts and the QDs, allowing us to explore different coupling regimes. The combination of side gates and backgate also makes it easier to obtain double quantum dot (DQD) shell structure. In Fig. 5.1b, we sketch the tunnelling rates of the QDs to the common superconducting leads (SC), Γ_{L1}, Γ_{L2}, Γ_{R1}, and Γ_{R2}, which may vary among different shells of the QDs and can be tuned by V_{bg}. The QDs may also be coupled to each other by an inter-

dot tunnel coupling, t_d. We identify the different shells by the letters W, X, Y. QD parameters extracted for these are given in Table 5.1. For an overview of the different shells explored, see Appendix B.

The source and the drain contacts of the device each branch out into two leads as shown in Fig. 5.1a, enabling us to characterize the parallel JJs [104] in a four-terminal configuration (at the level of the leads) by applying a current, I_{bias}, from source to drain leads and measuring the voltage response, V, in a different pair of leads. In this way, we obtain $I_{bias} - V$ curves which switch from a supercurrent branch at low I_{bias} to a high-slope dissipative branch at I_{sw}. Two of such curves are shown in Fig. 5.1c,d for the open and Coulomb blockaded regimes, respectively. We measure I_{sw} up to 35 nA in the former regime and up to approximately 500 pA in the latter regime. Figure 5.1d is measured with QD_L in Coulomb blockade and QD_R near a Coulomb resonance. Note that the supercurrent exhibits hysteresis, as the switching is found at different current for positive and negative applied bias. In Coulomb blockade, the supercurrent branch shows a finite slope, R_S, which increases with $\sim 1/I_{sw}$; however, this does not affect our identification of I_{sw} as a jump in the curve down to 5 pA (see Appendix B). In our analysis below we do not claim quantitative estimates of the critical current, I_c (which may be larger), but address merely the qualitative behavior of I_{sw}. From independent $I_{bias} - V$ measurements in the open regime, we estimate an upper bound of the metal-lead/hybrid-nanowire contact resistance in the order of 20 Ω (see Appendix B for more information).

As a guide to the different GS configurations accessed in this work, we show in Fig. 5.1e a sketch of the phase diagram of the parallel DQD JJ versus coupling to the leads when the two QDs have *independent* GSs ($t_d = 0$). The sketch corresponds to odd occupancy (1,1) of the QDs and it is valid for the large level-spacing regime, $\Delta E_i > U_i$, where i stands for left and right QDs. The independent-GS case is applicable to our device as most I_{sw} measurements are done away from the triple points of the QDs, where the effect of a finite t_d is negligible. GS changes occur when the total tunnelling rates $\Gamma_{L,R}$ of each of the QDs to the common superconducting leads surpass a threshold which depends on $U_{L,R}/\Delta$ [42], where Δ is the superconducting gap. Above this threshold, the spin of each QD is individually screened by the superconducting leads via the YSR mechanism [55, 105]. For doublet GS, the current-phase rela-

5. JOSEPHSON JUNCTIONS IN DOUBLE NANOWIRES BRIDGED BY IN-SITU DEPOSITED SUPERCONDUCTORS

Table 5.1: Parameters for shells W, X, Y of Device 1. The charging energies, $U_{L,R}$, are extracted from Coulomb diamond spectroscopy. The total tunnelling rates of each QD, $\Gamma_{L,R}$, are obtained by (*a*) fitting the even side of Coulomb diamonds in the normal state, or (*b*) from the full width at half maximum of the corresponding Coulomb peak. The Kondo temperature, T_K, is obtained by (*c*) fitting the Kondo peak (when applicable), or by (*d*) using the equation $T_K = \frac{1}{2k_B}\sqrt{\Gamma U}e^{\pi\epsilon_0(\epsilon_0+U)/\Gamma U}$, with $\Gamma_{L,R}$, $U_{L,R}$ as known values, and $\epsilon_0 = \epsilon_{L,R}$ the level position of the corresponding QD. Extraction methods are presented in detail in Appendix B. From the charge stability diagram we extract similar sidegate and backgate capacitances for the left and right QD in the order of $C_{gL,gR,bg} \sim 1$ aF and thus the charging energies are dominated by the source and drain capacitances.

Shell	U_L (meV)	U_R (meV)	Γ_L (meV)	Γ_R (meV)	$\frac{\Gamma_L}{U_L}$	$\frac{\Gamma_R}{U_R}$	$k_B T_{K_L}$ (meV)	$k_B T_{K_R}$ (meV)	$\frac{k_B T_{K_L}}{0.3\Delta}$	$\frac{k_B T_{K_R}}{0.3\Delta}$
W	3.8 ± 0.5	2.3 ± 0.3	0.23 ± 0.02^a	0.6 ± 0.1^b	0.06 ± 0.01	0.26 ± 0.05	$(3.1 \pm 0.3) \cdot 10^{-5d}$	0.03 ± 0.01^d	$6 \cdot 10^{-4}$	0.5
X	3.7 ± 0.5	1.1 ± 0.3	0.33 ± 0.01^a	0.55 ± 0.05^d	0.09 ± 0.01	0.5 ± 0.1	$(8 \pm 1) \cdot 10^{-5d}$	$0.07 - 0.18^{c,1}$	0.001	3.2
Y	3.6 ± 0.5	1.1 ± 0.3	1.05 ± 0.01^a	0.55 ± 0.05^d	0.29 ± 0.04	0.5 ± 0.1	0.06 ± 0.02^d	$0.07 - 0.18^c$	1	3.2

tionship is π-shifted, e.g. $I = I_c\sin(\phi + \pi)$ [32, 33, 87, 93] as indicated in Fig. 5.1e. The simple analysis above is valid when a single level Coulomb blockaded QD acts as a weak link instead of e.g. a quantum point contact (single barrier), where a non-sinusoidal current-phase relationships applies [106].

To estimate t_d, we first investigate via two-terminal voltage-biased differential conductance (dI/dV) measurements two shells corresponding to the two leftmost quadrants of the DQD phase diagram in Fig. 5.1e. The two-terminal dI/dV is recorded using standard lock-in amplifier techniques with an AC excitation of 2 μV. Figure 5.2a shows a colormap of dI/dV at source-drain bias $V_{SD} = 0$ of shell W in the superconducting state versus V_{gL} and V_{gR}, which represents the stability diagram of the two QDs in the weakly-coupled regime where $\Gamma_{L,R} \ll U_{L,R}$ (see Table 5.1 for shell parameters). Since the slope of the supercurrent branch, R_S, is empirically related in our device to $1/I_{sw}$, we can use $R_S = 1/(dI/dV(V_{SD} = 0))$ as an indicator of the magnitude of I_{sw}. This is particularly relevant in the Coulomb-blockade regime, when I_{sw} is small and R_S is significant (see Appendix B). We only use this empirical relation to comment on the voltage-biased measurements in Fig. 5.2. We observe approximately vertical and horizontal conductance lines which overlap and displace each other at their crossings, without exhibiting any significant bending. The displacement is a signature of a finite interdot charging energy, while the lack of bending indicates that $t_d \approx 0$
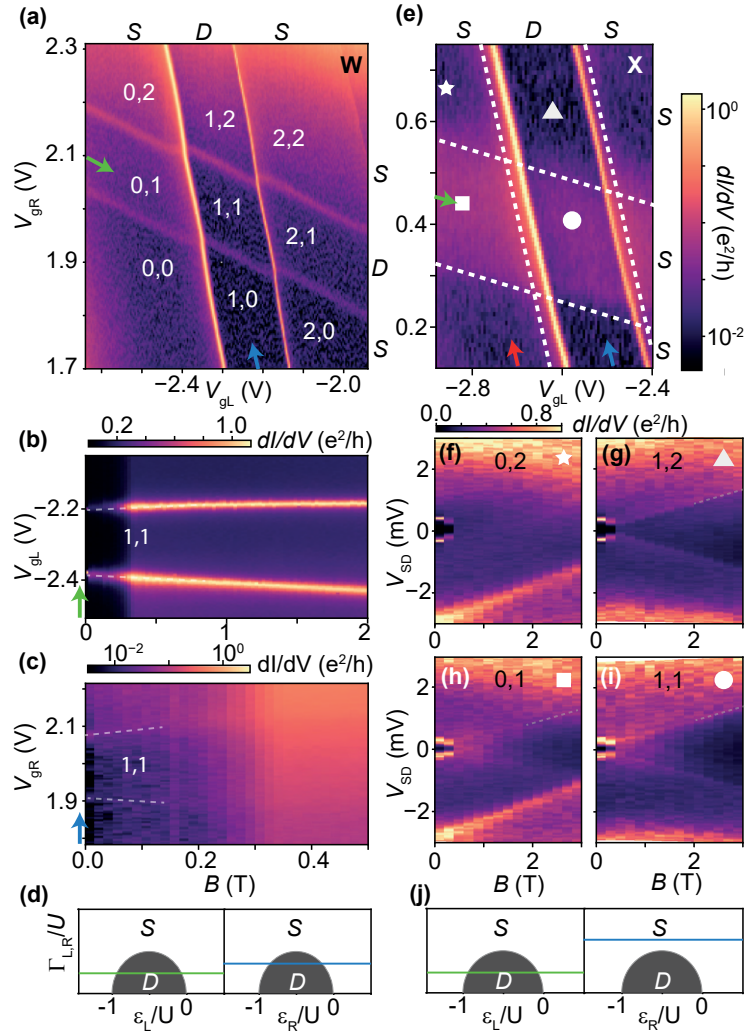
Figure 5.2: (a,e) Colormaps of two-terminal, voltage-biased zero-bias differential conductance, dI/dV, in the superconducting state for shells W (a) and X (e) vs. left and right QD plunger gates. In (a), charges N_L, N_R correspond to the charge occupation of the highest unoccupied energy level of each QD. In (e), white dashed lines represent the position of the Coulomb lines measured at $B = 2$ T. (b,c) Zero-bias dI/dV colormaps showing the magnetic field, B, dependence of parity transition lines which enclose the 1,1 charge sector in (a), vs. plunger gate voltages of the (b) left and (c) right QDs, obtained by sweeping the gates along the green and blue arrows, shown in (a). For simplicity, only V_{gL} and V_{gR} are respectively shown. (f-i) Colormaps of dI/dV vs. magnetic field, B, and source-drain bias voltage, V_{sd}, taken in four different charge sectors indicated by symbols in (e). Higher B field measurement of (h) can be found in Appendix B. Dashed lines are added as a guide to the eye. (d,j) Pairs of phase-diagram sketches for independent left and right QDs. Horizontal color-coded lines in each pair indicate qualitatively $\Gamma_L(\Gamma_R)$ vs. left (right) QD level position $\epsilon_L(\epsilon_R)$ in the stability diagrams of (a) and (e), respectively, following the arrows shown.

(with an upper limit of 50 μV based on the width of the sharpest conductance lines). No signatures of crossed-Andreev reflection (CAR) or of elastic co-tunnelling [107] are observed in this measurement. We interpret these lines as GS parity transition lines, which indicate changes of parity in the left and right QDs, respectively. The lines separate nine different and well-defined parity sectors. We assign corresponding effective left and right QD charges, N_L, N_R, to each of these sectors based on the shell-filling pattern of the stability diagram in larger plunger-gate ranges (see Appendix B). The charges obtained in this way are indicated in Fig. 5.2a. These charges correspond to the charge occupation of the highest unoccupied energy level of each QD.

To assign GS parities to these nine sectors, and to determine independently if, in addition to interdot charging energy, there is a significant t_d, we trace the evolution of the parity transition lines of the 1,1 charge sector against B. In the case of singlet GS, i.e., when the spins of the two QDs are exchange-coupled (finite t_d), these lines are expected to come together with B [108]. Instead, as shown in the zero-bias dI/dV colormaps in Figs. 5.2b,c, the parity transition lines enclosing the 1,1 charge sector split apart with B, i.e., the two QDs are independent doublets, despite the relative proximity of the two nanowires. The splitting of the parity lines occurs both in the case when the parity of the left (right) QD is varied and the right (left) QD is kept in the doublet GS (see green and blue arrow, respectively, in Fig. 5.2a). The GS (singlet S or doublet D) of the other eight charge sectors are indicated on the top and right exterior parts of the stability-diagram colormap in Fig. 5.2a.

Given the decoupling between the two QDs, we can approximate their phase diagrams by those of two independent single QDs. Neglecting the interdot charging energy, we sketch in Fig. 5.2d the well-known single-QD phase diagrams for the GS of the left and right QDs versus QD level position, $\epsilon_{L,R}$, and versus the total tunnelling rate of each QD to the leads, $\Gamma_{L,R}$, over their charging energy, $U_{L,R}$. The doublet dome has an upper height limit of $\Gamma_{L,R}/U_{L,R} = 1/2$ in the infinite Δ limit, and its height decreases in the $U \gg \Delta$ limit (i.e., the YSR regime) to which our QDs belong [77,109]. In the left phase diagram, the horizontal green line which crosses the doublet dome indicates a cut where ϵ_L is varied and ϵ_R is kept fixed such that the GS parity of the right QD is a doublet, and the GS parity of the left QD is variable. This line rep-

resents schematically the gate trajectory in Fig. 5.2b, as indicated with the green arrow, which is collinear to the green arrow in Fig. 5.2a, and which varies the parity of the left QD as *S-D-S* while keeping the parity of the right QD as *D*. A similar relation exists between the horizontal blue line in the right phase diagram, and the gate trajectory (blue arrow) in Fig. 5.2c, also collinear to the corresponding arrow in Fig. 5.2a. From these phase diagrams, we note that parity transitions are strictly equal to Coulomb degeneracies only at zero $\Gamma_{L,R}$. The measurements above confirm the expected DQD behavior for low lead couplings, which shows a *D,D* ground for charge state 1,1 corresponding to the lower left quadrant of the phase diagram in Fig. 5.1e.

   Next, we investigate a shell with different couplings to the leads (shell X) which belongs to the upper left quadrant of phase diagram in Fig. 5.1e. Figure 5.2e shows the zero-bias dI/dV colormap in the superconducting state vs. the plunger gates of the two QDs of shell X. The two horizontal GS-parity transition lines, which bounded the green trajectory in the case of shell W, are absent in the case of shell X, and are instead replaced by a band of enhanced conductance. The conductance band is cut two times by approximately vertical conductance lines, which correspond to GS-parity transition lines of the left QD.

   The parity of the band of enhanced conductance in the stability diagram is determined from the *B*-evolution of the differential conductance in the normal state versus V_{sd} at two fixed gate voltages. These two gate voltages are indicated by a square (charge states 0,1) and a circle (1,1) in the stability diagram, and their *B* dependence is respectively shown in Figs. 5.2h,i. As a control experiment, the *B* dependence for two fixed gate voltages above the conductance band indicated by a star (0,2) and a triangle (1,2) in the stability diagram, is shown in Figs. 5.2f,g. The four measurements show closing of the superconducting gap at $B = 0.4$ T, which is consistent with the jump in the zero-bias dI/dV signal in Figs. 5.2b,c at $B \approx 0.4$ T. However, whereas Figs. 5.2g-i (1,2 0,1 1,1) display conductance steps near zero-bias which split with *B* field in the normal state, there is no such splitting in Fig. 5.2f, consistent with even filling of both dots. We assign effective QD charge numbers to the charge stability diagram from a $B = 2$ T measurement shown in Appendix B, and overlay the Coulomb lines obtained, which delimit the nine charge sectors (white dashed lines in Fig. 5.2e).

We note an additional important difference in the data of the low-bias splitting states. In Fig. 5.2g (1,2) the splitting can be traced back to zero bias at $B = 0$, while in Fig. 5.2h (0,1) the splitting is traced to zero bias only at a finite field of ≈ 1 T. The pair of features whose splitting can be traced to a $B = 0$ onset in Fig. 5.2g (1,2) correspond to co-tunnelling steps of the odd-occupied left QD experiencing Zeeman splitting. In turn, the pair of features which starts to split at 1 T in Fig. 5.2h corresponds to the Zeeman splitting of a Kondo resonance in the right QD. The splitting ensues when $E_Z \sim k_B T_{K_R}$. [110] Notice that the Kondo resonance is also visible in the data after the gap closure at $B = 0.4$ T. From the splitting, we find a g-factor $g \sim 8.5 \pm 0.1$. Table 5.1 shows that $k_B T_{K_R} > 0.3\Delta$ for shell X, which is consistent with a YSR singlet state in the right QD in the superconducting state.

The B-dependence data in Figs. 5.2f-i therefore allows us to assign the GS to the QDs, D or S, in each of the nine sectors in Fig. 5.2e. We indicate schematically by a green and blue horizontal line in the two individual-QD phase-diagrams in Fig. 5.2j the GS along the gate trajectories collinear to the same-colored arrows in the colormap of Fig. 5.2e. The green (blue) gate trajectory, which goes along (perpendicular to) the band of enhanced conductance intersects twice (goes above) the doublet dome, leading to two (zero) parity transitions.

5.3 Supercurrent interference for different quantum-dot parities

We switch back to the four-terminal measurement configuration to correlate the intrinsic phase of each JJ with the magnitude of I_{sw}. In Fig. 5.3, we show I_{sw} versus plunger gate voltages, where I_{sw} is extracted in a similar fashion as in Fig. 5.1d. In Figs. 5.3a,c (5.3b,d), the plunger gate voltages are swept along trajectories which vary the occupation in the left (right) QD while keeping the occupation of the right (left) QD fixed, following the green (red, blue) arrows in Figs. 5.2a,e, i.e. for shell W and X, respectively. For reference, we assign the expected phase-shift in the current-phase relationship, π or 0, based on the measured GS parities of the two QDs. This phase-shift is accurate when at least one QD is in Coulomb blockade. The value of I_{sw} at the parity transitions may include contribution due to presence of bound states crossing zero-

Figure 5.3: (a-d) Extracted I_{sw} vs. plunger-gate voltage trajectories collinear to same-colored arrows in (a,b) Fig. 5.2a, shell W, and (c,d) Fig. 5.2e, shell X. In (d), two traces are shown to illustrate the decrease in I_{sw} as a consequence of the subtracting effect of a π phase-shift in one of the QD Josephson junctions. The red curve is offset on the gate axis in order to correct for the cross-talk between the gates and the QDs. The I_{sw} is extracted by measuring the $I_{bias} - V$ curve from negative to positive current for each gate value, and is identified as the switching on the positive current branch.

energy. Hence, the magnitude of I_{sw} on transitions should not be taken into account.

The common phenomenology in the data is as follows. After a smooth build-up of I_{sw} towards a $0 \to \pi$ transition, the current abruptly drops at the edge of the π domain, resulting in an asymmetric I_{sw} peak [33]. A pair of asymmetric peaks is seen in the data in Figs. 5.3a-c, as one of the QDs experiences parity transitions and therefore a sequence of $0 - \pi - 0$ phase-shift changes. If the parity stays unchanged, such peaks are absent, as in Fig. 5.3d. Instead, I_{sw} is smoothly enhanced towards odd occupation of the right QD, which is YSR-screened (i.e., $k_B T_K > 0.3\Delta$) [93]. Interestingly, when comparing the red and blue traces in Fig. 5.3d, which correspond to different phase shift (π and 0, respectively) in the JJ formed by the left QD, we observe that I_{sw} is stronger near $V_{gR} = 0.4$ V. Note that $V_{gR} = 0.4$ V corresponds to the

1,1 charge state for the blue trace, and to the 0,1 charge state for the red trace. The exact magnitude of I_{sw} in that gate value for the red and blue curve is consistent with what is found in Fig. 5.3c in the ($\square$) and ($\bigcirc$) respectively. We can interpret the reduction in I_{sw} at $V_{gR} = 0.4$ V in the blue trace with respect to the red trace by considering the double nanowire device as a SQUID at zero threaded magnetic flux [32,87,93]. The I_c of a SQUID with a sinusoidal current-phase relation at zero flux can be written as [93]

$$I_c = \sqrt{(I_{c1} - I_{c2})^2 + 4I_{c1}I_{c2}\left|cos\left(\frac{\delta_1 + \delta_2}{2}\right)\right|^2} \qquad (5.1)$$

where $I_{c1,c2}$ are the critical currents of the two JJs, and $\delta_{1,2}$ are the intrinsic phase shifts (0 or π) of the junctions. As a result, the total I_c is given by $I_{c\square} = I_{c1} + I_{c2}$ when the DQD is in the 0,0 phase, and $I_{c\bigcirc} = I_{c1} - I_{c2}$ in the π,0 phase. These equations can explain the findings in Fig. 5.3c,d, as I_{sw} is enhanced when both JJs have the same intrinsic phase, and it is weaker when the two JJs have different phase.

5.4 Screening evolution of switching current

Finally, we demonstrate individual control of the couplings between the SC leads and the QDs, realizing the transition from the upper left (one screened spin in 1,1) to upper right quadrant (both spins screened) in the YSR phase diagram depicted in Fig. 5.1e. Whereas the changes in GS parity in Fig. 5.2 occurred primarily by changing the side-gate voltages to go from shell W to shell X, here the changes occur within a unique shell. This is done in a shell identified as Y, using V_{bg} as a tuning knob of $\Gamma_{L,R}$. In Figs. 5.4a-c, we show colormaps representing parity stability diagrams at different V_{bg} analogous to those in Figs. 5.2a,e; however, instead of plotting a measurement of voltage-biased dI/dV, we directly plot a four-terminal measurement of I_{sw} vs. plunger-gate voltages. To obtain each colormap, we measure the $I_{bias} - V$ characteristic at each plunger gate voltage coordinate (i.e., at each pixel in the colormap) and extract I_{sw} as in the example in Fig. 5.1d.

In Fig. 5.4a, the I_{sw} parity stability diagram shows two I_{sw} peaks which correspond to two parity transitions of the left QD. The lack

Figure 5.4: (a-c) Colormaps of I_{sw} as a function of the plunger gates of the two QDs, taken at three different V_{bg} values in shell Y. In (a), Coulomb lines positions (black dashed lines) are obtained from a normal-state two-terminal differential conductance measurement at $B = 2$ T. To keep shell Y in frame, the effect of V_{bg} has been compensated by changing V_{gL} and V_{gR}. In (a) and (c), the GS of the two independent QDs is indicated on the exterior side of the colormaps. (d) Independent-QD phase-diagram sketches as function tunnelling rate $\Gamma_{L,R}$ and QD level position, $\epsilon_{L,R}$, for the left QD (top panel) and right QD (lower panel). In the top panel, green-shaded horizontal lines indicate qualitatively Γ_L in directions collinear to the arrows of the same color in (a-c). The blue line indicates qualitatively Γ_R in (a-c). Note that decreasing the back-gate voltage results in stronger coupling to the left superconducting lead. The I_{sw} is extracted by measuring the $I_{bias} - V$ curve from zero to positive current for each gate point.

of right-QD parity transition lines indicates that the right QD is YSR-screened. We corroborate that this is indeed the case from a measurement of T_{K_R} at $B = 0.4$ T in the normal state, and we find $k_B T_{K_R} > 0.3\Delta$ (see Table 5.1). We also note that, although faintly-visible here, a two-terminal dI/dV measurement of the stability diagram in otherwise the same conditions as here displays an horizontal band of (weakly) en-

hanced conductance, which is the same phenomenology identified in Fig. 5.2d with YSR spin-screening. However, the enhancement is weak enough to preclude resolution of I_{sw}, and therefore a similar band of I_{sw} does only show at the right part of Fig. 5.4a ($V_{gL} \approx -2.95$ V, $V_{gR} \approx 0.45$ V).

Reducing V_{bg} alters the I_{sw} parity stability diagram by bringing the two I_{sw} peaks (parity lines) of the left QD closer together, as shown in Fig. 5.4b. Note that a faint, approximately horizontal band of I_{sw} is observed along the direction pointed by the dark-green arrow, which comes as a result of enhancement of I_{sw} due to YSR spin-screening of the right QD. In Fig. 5.4c, further reduction of V_{bg} leads to merging of the parity lines into a vertical band of I_{sw} across the whole plot. At this point, the spins of both QDs are YSR-screened into singlets. We have therefore traced the phase diagram shown in Fig. 5.1e, where either one spin of a QD or both are screened by the YSR mechanism, triggering a phase change in the current-phase relation of the JJs. Additional data on the magnetic field dependence of this shell can be found Appendix B.

5.5 Searching for bound state hybridization

In this section, we present measurements conducted in two different coupling regimes, compared to what is shown in the previous sections, with the motivation of observing signatures of CAR by studying the behavior of the bound states formed on each QD. A signature of CAR in double nanowire devices, would be observing anti-crossings between the bound states which are interpreted as hybridization of the two states owing to the CAR process.

In Fig. 5.5a a charge stability diagram of the same device discussed in the previous sections is shown. Now, the couplings between the QDs and the superconducting leads are weaker, placing the device in the $\Gamma \ll U$ regime. The DQD is also tuned in the single-level regime, since clear even-odd pattern is observed in both QDs. Figure 5.5b shows a bias spectroscopy measurement following the red dashed line of Fig. 5.5a. Here, QD_R is tuned while QD_L is kept at fixed electron number. Bound states belonging to QD_R are dispersing with the change of the gate voltage, while the bound states of QD_L do not. A similar behaviour is observed in the reverse scenario when QD_L is tuned in

Figure 5.5: (a) Charge stability of the double quantum dot tuned in the weakly coupled regime. Coloured dashed lines correspond to the trajectory of the bias spectroscopy measurements shown in the next panels. (b) Bias spectroscopy measurement tuning the electrons of the right QD. Bound states belonging to the QD that is being tuned show dispersion (pointed by the red arrow), while the bound states of the QD with fixed number of electrons are independent to the gate setting (black arrow). (c,d) Bias spectroscopy measurements now tuning the left QD following the dashed black and gray arrows respectively. Bound states belonging to the left QD show dispersion (black arrow) while the ones of the right QD do not (red arrow). All measurements are saturated in conductance to highlight the faint features of the bound states. Note that no anti-crossing of the two bound states is observed.

Fig. 5.5c,d. The difference between the two panels is that Fig. 5.5d is measured closer to the resonance of QD_R, bringing the bound state of QD_R at a lower energy (pointed by red arrow). Note that in a standard Josephson junction, we do not expect to see bound states crossing zero energy as there should be no density of states in the window -2Δ to 2Δ. However, we see replicas of bound states crossing zero energy, and they are attributed to a local density of states in one of the superconducting leads (soft superconducting gap). Furthermore, we observe that near charge degeneracies where the two bound states are found at the same

energy, no signs of anti-crossings are seen. On the contrary, the states
are crossing, hinting that there is no CAR process mediating the two
states. A possible reason why we did not observe signs of CAR is that
we did not measure the device is the right coupling regime. It may be
more favourable for CAR processes to tune the device in a higher cou-
pling regime, as that might enhance the probability of splitting a Cooper
pair to the two QDs [103].

Figure 5.6 shows an additional dataset in an intermediate coupling
regime, where bias spectroscopy cuts are measured tuning the right
(Fig. 5.6b) and the left QD (Fig. 5.6c). No signs of anti-crossings between
the two sets of bound states are observed.
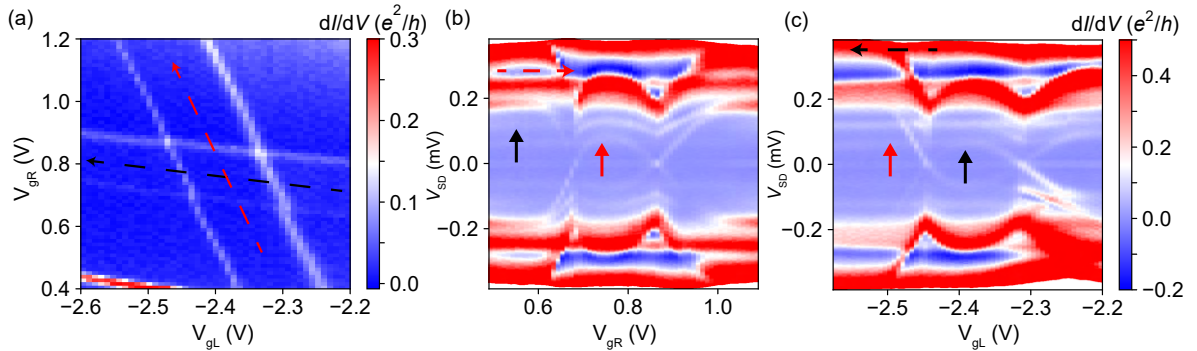
Figure 5.6: (a) Charge stability of the double quantum dot tuned in an intermediate
coupled regime. Coloured dashed lines correspond to the trajectory of the bias spec-
troscopy measurements shown in the next panels. (b) Bias spectroscopy measurement
tuning the electrons of the right QD. Bound states belonging to the QD that is being
tuned show dispersion (pointed by the red arrow), while the bound states of the QD
with fixed number of electrons are independent to the gate setting (black arrow). (c)
Bias spectroscopy measurements now tuning the left QD following the dashed black
arrows. Bound states belonging to the left QD show dispersion (black arrow) while
the ones of the right QD do not (red arrow). Bias spectroscopy measurements are
saturated in conductance to highlight the faint features of the bound states. No anti-
crossing of the two bound states is observed.

5.6 Conclusions & Outlook

In conclusion, we have demonstrated parallel quantum-dot Josephson
junctions fabricated out of a double-nanowire platform in which the
nanowires are bridged by an in-situ deposited superconductor. We

mapped out the parallel quantum dot YSR phase diagram via conductance and switching current measurements showing the tunability of the ground state of each JJ from doublet to singlet. The analysis also revealed that the nanowires are predominantly decoupled with an upper bound on the dot tunnel coupling in the order of $t_{\mathrm{d}} \leq 50~\mu$eV for the specific charge states studied in two devices (see Appendix B). A lower bound is hard to identify due to the lack of evident anti-cross in Device1, but in Device2 the lower bound of t_{d} is estimated to be in the same order of magnitude as the upper bound. In general, other shells may be stronger coupled at higher gate voltages and the interdot tunnel coupling may be increased by adjusting nanowire growth parameters [19]. Finally, we showed indications of switching current addition and subtraction via appropriate choice of ground states of the two dots involving the YSR singlet state, i.e., $0,0$ and $\pi,0$ (phase difference) regimes, respectively.

The above observations of basic superconducting properties in insitu made hybrid double-nanowire material open up for more advanced experiments addressing a number of recent theoretical proposals. In parallel double-quantum-dot Cooper-pair splitters [47, 111], the CAR mechanism responsible for the splitting is weakened by an increase in the distance between the tunnelling points from the superconductor into the two quantum dots [112]. The proximity of the nanowires set by growth [19] and the cleanness of the Al-InAs interface may turn out beneficial for CAR, which is also the basis for creating coupled YSR states in these systems [55, 113]. The latter is investigated in a parallel work on the same hybrid double-nanowire material [19] as used in this work [103]. The hybrid double nanowires are furthermore prime candidates for realizing several species of topological subgap states [8, 56]. For finite CAR, the requirements for entering the topological regime hosting Majorana bound states have been shown to be lowered [58, 62], and parafermions may be achieved in a regime where CAR dominates over local Andreev processes [8]. In superconducting islands fabricated in our hybrid double nanowires, the topological Kondo effect can be pursued, [9, 10, 65] and in Josephson junctions as here demonstrated, non-standard types of Andreev bound states have been predicted [64] in the topological regime. Furthermore, a φ_0 junction geometry can be investigated in the double-nanowire platform, by implementing the dou-

ble nanowires in a SQUID. As an ending remark, we note that double nanowires can also be made with a full superconducting shell [19, 114], relevant for investigating flux-induced subgap states [71, 115, 116].

6

COULOMB BLOCKADE IN DOUBLE NANOWIRE SUPERCONDUCTING ISLANDS

In this chapter we characterize in-situ grown parallel nanowires bridged by a superconducting island. We show that the defined superconducting island is connecting the two nanowires and their Coulomb blockade resonances can be probed by multi-terminal devices. The temperature and magnetic field dependence of the resonances is investigated, showing that the same bound state is extended in both nanowires. These nanowires show promise for the implementation of several proposals that rely on parallel nanowire platforms.

6.1 Introduction

In-situ grown double nanowires are at the center of research regarding qubit devices [49], coupled sub-gap states [55, 103] and exotic topologi-

cal superconductivity, as a plethora of theoretical proposals [8, 56–66] and experiments involve paralAllel wires coupled to superconductors [17–19, 54, 103, 114]. These devices constitute the basis for the design of the so-called Majorana-Cooper pair boxes [117–119] and provide the key element for the observation of the predicted topological Kondo effect in hybrid superconductor-double-nanowire islands [9, 10, 120], which would signal the non-local nature of Majorana zero-energy modes.

Superconducting islands (SIs) [37, 38, 121–123] in *single* nanowires have been extensively studied in the last years. Subjects explored are quasiparticle relaxation, poisoning lifetimes [13, 28, 124] and the evolution of SI Coulomb peaks in a magnetic field [14, 35, 36, 125–131] to shed light on potential topological properties [132]. Furthermore, devices incorporating the Little-Parks effect [115], interferometry [133] and reflectometry [134–136] yielded additional insight. The most commonly studied material system has been InAs/Al but alternative superconductors such as NbTiN, Sn and Pb [137–140] or alternative nanowire materials [125, 141] have been explored. Despite this progress and their multiple applications, SIs coupled to multiple nanowires have not yet been demonstrated.

Here we realize multi-terminal hybrid *double*-nanowire SI devices by utilizing *in-situ* grown InAs semiconductor double nanowires bridged by a small epitaxially-grown Al superconductor. The devices display different charging energy regimes, which we explore in various two-terminal combinations. In a first device, we measure the magnetic field and temperature dependence of the SI Coulomb peaks, and find a similar dependence in every two-terminal combination. Using a thermal model which describes the free energy difference of even and odd states [13], we extract consistently similar bound state energies for different two-terminal combinations in two different gate configurations. Our results indicate the presence of a common bound state coupled to the four ends of the nanowires and thus extended across the hybrid SI. In a second device, we observe two-electron charging free of quasiparticle poisoning.
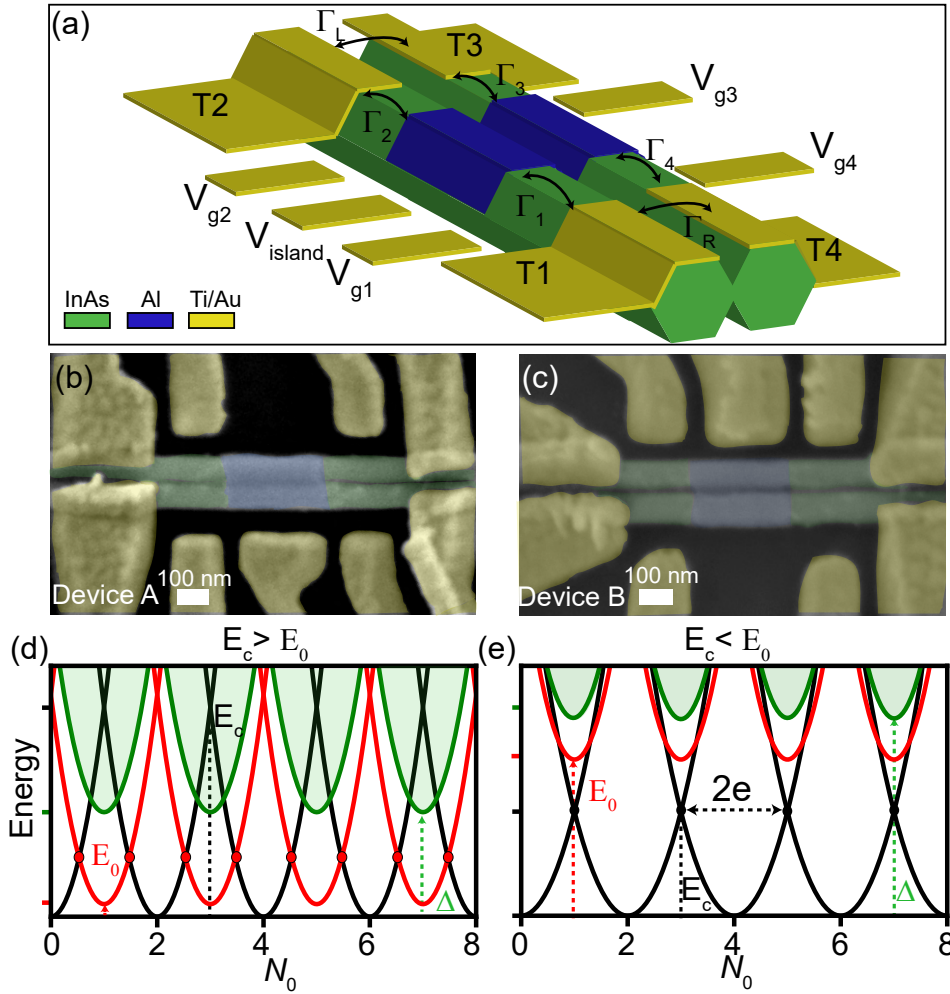
Figure 6.1: (a) Schematic of a double-nanowire SI device. (b-c) Scanning electron microscopy images of two functional SI devices. (d-e) Energy as a function of the induced charge $N_0 \propto V_{\text{island}}$ in the SI for the regime (d) $E_c > E_0$ and (e) $E_c < E_0$. Black parabolas describe states with even electron number corresponding to Cooper pairs. Red parabolas describe states with an odd electron number corresponding to a quasiparticle occupying a sub-gap state whose energy at odd N_0 values is E_0. For $E_c > E_0$, even-parity states are the ground state in a window of width $2(E_c + E_0)/E_c$ centered around even N_0 values, while odd-parity states are the ground state in a window of width $2(E_c - E_0)/E_c$ centered around odd N_0 values. Red dots indicate the crossing of parabolas differing by one electron. For $E_c < E_0$, even-parity states are the ground state at any N_0. The point where two parabolas of the same parity meet yields E_c measured from the base of the parabolas (black dashed line). Green parabolas correspond to the charge dispersion of the edge of the superconducting gap Δ.

6.2 Results and discussion

Figure 6.1(a) shows the devices concept. Two nanowires (green) provide access to the SI (blue) through four metallic terminals (T1−T4, yellow) with coupling tunability (Γ_{1-4}) and gate-induced island charge tunability (V_{island}). Interwire couplings ($\Gamma_{L,R}$) are also present. Figure 6.1(b,c) shows scanning electron microscopy (SEM) images of the investigated devices. The nanowires are grown by molecular beam epitaxy on a pre-patterned substrate where the inter-wire spacing and their diameters are well controlled [19]. Their hexagonal cross-sections have a diameter $d \approx 85$ nm, with three of their facets covered by an epitaxially-grown aluminum film of thickness ≈ 17 nm which also bridges them. The nanowires are placed on a doped Si/SiO_2 substrate with an oxide thickness of 275 nm and standard electron beam lithography (EBL) techniques are followed to selectively etch (using Transene D for 9 seconds) the aluminum and form 300 nm-long SIs. Contacts and gates are defined by EBL, and metal evaporation of 5 nm Ti/205 nm Au is performed after an argon milling treatment of the native InAs oxide to establish good ohmic contact. The contacts are separated from the SI by ≈ 220 nm of bare nanowire segments.

The SI is characterized by a capacitance C, resulting in a sizable charging energy $E_c = \frac{e^2}{2C}$. This yields a parabolic energy dispersion of all states against V_{island} [see Fig. 6.1(d-e)]. These states are characterized by even or odd occupation numbers. Even states (black lines) correspond to Cooper pair states without Bogoliubov quasiparticle excitations. Odd states at low energies, instead, correspond to the presence of a single Bogoliubov excitation. In particular, for energies above the superconducting gap Δ, the system presents a continuum of one-quasiparticle states (green parabolas). In a SI made of a single conducting material, the ratio E_c/Δ determines whether, upon sweeping V_{island}, the SI can be filled with electrons one-by-one ($E_c > \Delta$) [37], or in steps of a Cooper pair ($E_c < \Delta$) [38]. In our heterostructured devices, the proximity between the semiconducting nanowire (InAs) and the superconducting aluminum gives rise to additional hybridized states. If any of them lies at an energy E_0 below Δ (red parabolas), the charging mechanism is determined by the ratio E_c/E_0 instead. The correspond-

66

ing parabolic dispersion for the two limiting ratios of E_c/E_0 is depicted in Fig. 6.1(d,e) as a function of the gate-induced charge $N_0 = C_0 V_{island}$ on the island, where C_0 is the capacitance between the island and the gate with applied voltage V_{island} [13, 14].

A measurable electrical current through the SI is caused by single quasiparticles that excite the ground state into a higher-energy state with charge differing by one electron. Therefore, a zero-bias differential conductance arises when parabolas of different color cross. If Andreev reflection is allowed by sufficient coupling of the SI to the metallic leads, a current is also observed when two black parabolas cross in the $E_c < E_0$ case in Fig. 6.1(e).

In double-nanowire devices with $E_c > E_0$, the presence of a sub-gap state sufficiently tunnel-coupled to all leads causes a characteristic transport signature: The zero-bias differential conductance (dI/dV) between any given pair of the four terminals of the device must indeed reproduce the same spacing as a function of V_{island}, corresponding to electron loading/unloading into this state at the red dot degeneracies in Fig. 6.1(d). To this end, we measure dI/dV in device A in Fig. 6.1(b), which exhibits even-odd charging behavior of the SI consistent with $E_c > E_0$, in six different two-terminal setups (I − VI) against V_{island}, and present our results in Fig. 6.2. The measurements are conducted by sourcing one terminal with an AC voltage of $V_{AC} = 5\,\mu V$ superimposed on a DC voltage V_{DC}, and recording the differential conductance dI/dV on a second terminal while electrically floating the remaining two terminals. For example, Fig. 6.2(a) shows a zero-bias measurement using setup I, where the SI is probed via the upper nanowire through leads T3 and T4, while leads T1 and T2 are floating. Setups I, III, IV and V show clear peaks of conductance, while setups II, VI do not. The visible peaks appear at the same V_{island} voltages (due to partly shorted contacts in setup V and VI). However, the lack of additional peaks in the conductance spectra gives a first indication that the Coulomb resonances are consistent with a common sub-gap state in the SI as shown in the simple model of Fig. 6.1d.

We ascribe the lack of Coulomb peaks in setup II to the large coupling asymmetry of leads T1,T2, which leads to very faint features (for high-bias measurements see Appendix C). With setup VI, a large background conductance of more than 0.6 e^2/h is measured, reflecting the

large direct tunneling Γ_R between leads T1,T4. A closer inspection reveals dips of conductance at the gate values where we observe peaks in the other setups. The dips may be owed to the Fano effect [142], possibly coming from a resonant level from the SI and a highly transparent path with a continuum of states (tunnelling from lead T1 to T4). An inset in Fig. 6.2(f) shows a conductance dip fitted with the Fano formula yielding $q = -0.55$ [142, 143] consistent with the expected value. Setup V exhibits a weaker background conductance (0.02 e^2/h), indicating that $\Gamma_L < \Gamma_R$. Note that all combinations involving the lead T2 exhibit weakly conducting peaks suggesting a high asymmetry between the coupling Γ_2 and the couplings $\Gamma_{1,3,4}$.

We estimate $E_c \approx 0.5$ meV, (see Appendix C Fig. C.1) and $\Delta = 0.19$ meV (measured in nanowires from the same growth substrate [54]), from where $E_c > \Delta$ is confirmed. Note that the $E_c > \Delta$ case without a sub-gap state E_0 would also be consistent with the same Coulomb peaks structure of Fig. 6.2. To discern between these two interpretations we perform further measurements. We first focus on a broader bias voltage range around zero. Figure 6.3(a) shows a colormap of dI/dV against bias voltage and V_{island} measured with setup III. Here, apart from the evident Coulomb blockade structure of the SI, negative differential conductance (NDC) features are observed in blue at finite bias in an alternating pattern. While we can not clearly distinguish all excitation lines, these features resemble previous studies in SIs [13, 28], and appear only at gate ranges where the SI is charged with an *odd* number of electrons. However, the energy where the NDC is found is not consistent with the interpretation that a quasiparticle is trapped in the continuum states above the gap. A possible explanation is that quasiparticles are trapped to a second sub-gap state at a higher energy from the lower one, and this process creates NDC. This mechanism is of similar nature to quasiparticles being trapped in the continuum [13].

Next, we investigate the magnetic field (B) dependence of the zero-bias Coulomb peaks in the same V_{island} range as Figs. 6.2 and 6.3a. In this way, we establish whether the extracted g-factor from the Zeeman shift of the Coulomb peaks is consistent with a sub-gap state, and we confirm the parity assigned to the charge sectors. Figure 6.3(b) shows a colormap of the zero-bias differential conductance versus V_{island} and B recorded with setup III. Peaks delimiting odd parity sectors split apart
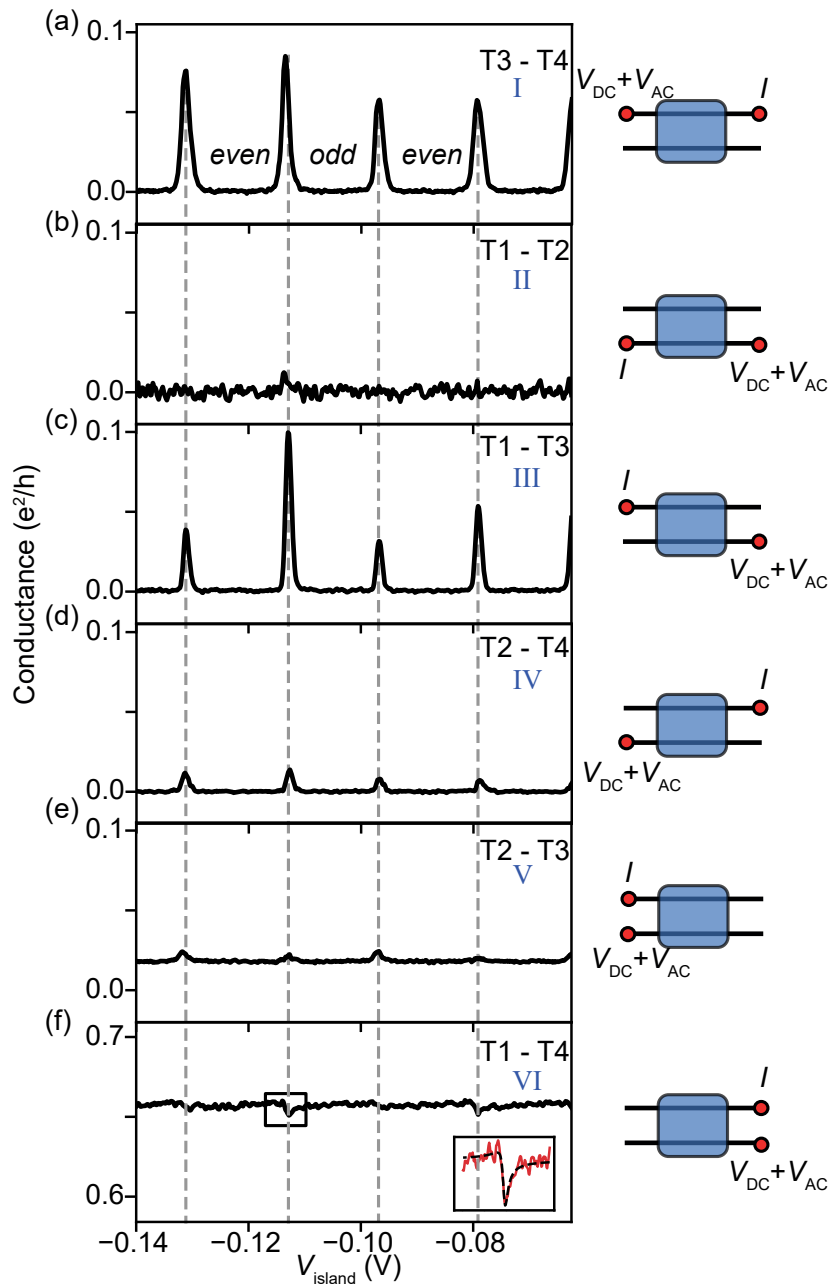
Figure 6.2: (a-f) Zero-bias conductance traces as a function of V_{island} for each two-terminal combination. Each panel is accompanied with a device schematic illustrating the measurement setup. Setups (a,c-f) show clear modulations of the conductance monitored at the same gate voltage (gray dashed lines), proving that the same charged object is probed. Dips of conductance superimposed on a large background conductance in (f) are interpreted as Fano resonances due to the interference of a continuum of states (interwire tunnelling) with the levels of the SI when they are on resonance.
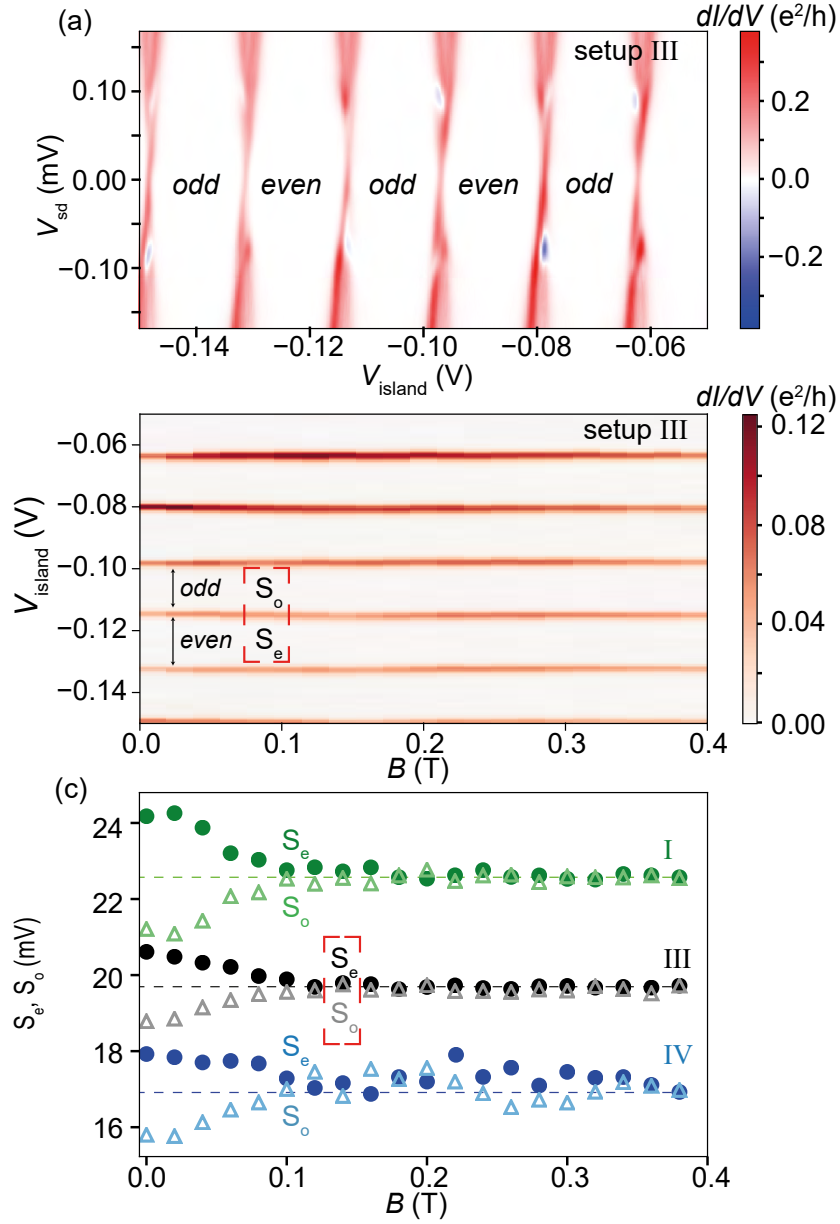
Figure 6.3: (a) High resolution bias spectroscopy of the SI in the setup III measured at base temperature $T = 30$ mK. Negative differential conductance features are observed when there is an unpaired quasiparticle in the SI (odd sectors). (b) Magnetic field B dependence of the island resonances measured at zero-bias. Spacings of even and odd sectors are indicated with S_e, S_o. (c) S_e (circle points) and S_o (light-colored hollow triangles) as a function of B for three different measurement setups. Red brackets correspond to the S_e, S_o spacings shown in (b). Error bars are smaller than the data points, therefore not shown. Data points of setups I and III have been offset on the y-axis for clarity. Dashed lines are added as guide to the eye. The low peak conductance in setup IV makes the peak spacing S_e, S_o more susceptible to noise.

Table 6.1: Extracted parameters using eq. S1 for two different gate tunings of Device A, as shown in Fig. 6.4(c,d). The gate voltages for tuning α are $V_{g1} = 0.35$ V, $V_{g2} = 0.5$ V, $V_{g3} = -1$ V, $V_{g4} = 2.2$ V and $V_{bg} = 1$ V. For gate tuning β the gates are set at the same voltages except for $V_{g3} = -0.8$ V and $V_{g4} = 2.3$ V.

	Setup	$\Delta(\mu eV)$	$E_0(\mu eV)$
	I	171±3	34±1
Gate tuning α	III	175±3	34±1
	IV	183±3	37±1
	V	172±3	15±1
Gate tuning β	III	175±3	12±1
	IV	173±5	11±1

with B, while those delimiting even parity domains come together. This observation is qualitatively consistent with both Δ reduction due to pair breaking and Zeeman splitting of the sub-gap state of energy E_0 (at $B = 0$). To discern between these two effects, we perform a quantitative analysis of the peak spacings from even and odd sectors, S_e and S_o. The effective g-factor of the spacing change with B is estimated at $g = 7.8 \pm 0.2$, consistent with a sub-gap state due to the hybridization between the InAs nanowires ($g = -15$ in bulk InAs) and the Al ($g = 2$ in bulk Al). To demonstrate that the Zeeman splitting is observed in various setups in consistency with a common sub-gap state in the SI, we show in Fig. 6.3(c) the evolution in B of the peak spacing for three different setups measured in the same V_{island} range. At $B \approx 100$ mT, the spacings converge and faint (irregular) oscillations are observed for higher magnetic fields. The convergence of $S_{e,o}$ below the critical field has been analyzed in terms of trivial/topological states [15,129,144] or the simultaneous diminishing of the gap [43]. Note that the complete closing of the superconducting gap occurs at higher magnetic field ($B_c \geq 200$ mT), as determined from additional measurements shown in Fig. S5 of the SM, which rules out that the extracted effective g-factor is mainly due to gap closure. This lower bound for B_c is in agreement with the upper bound of $B_c = 400$ mT obtained from Josephson devices based on nanowires from the same growth substrate [54].

A third piece of evidence of the presence of a common sub-gap state in the SI lies on the temperature evolution of the zero-bias reso-
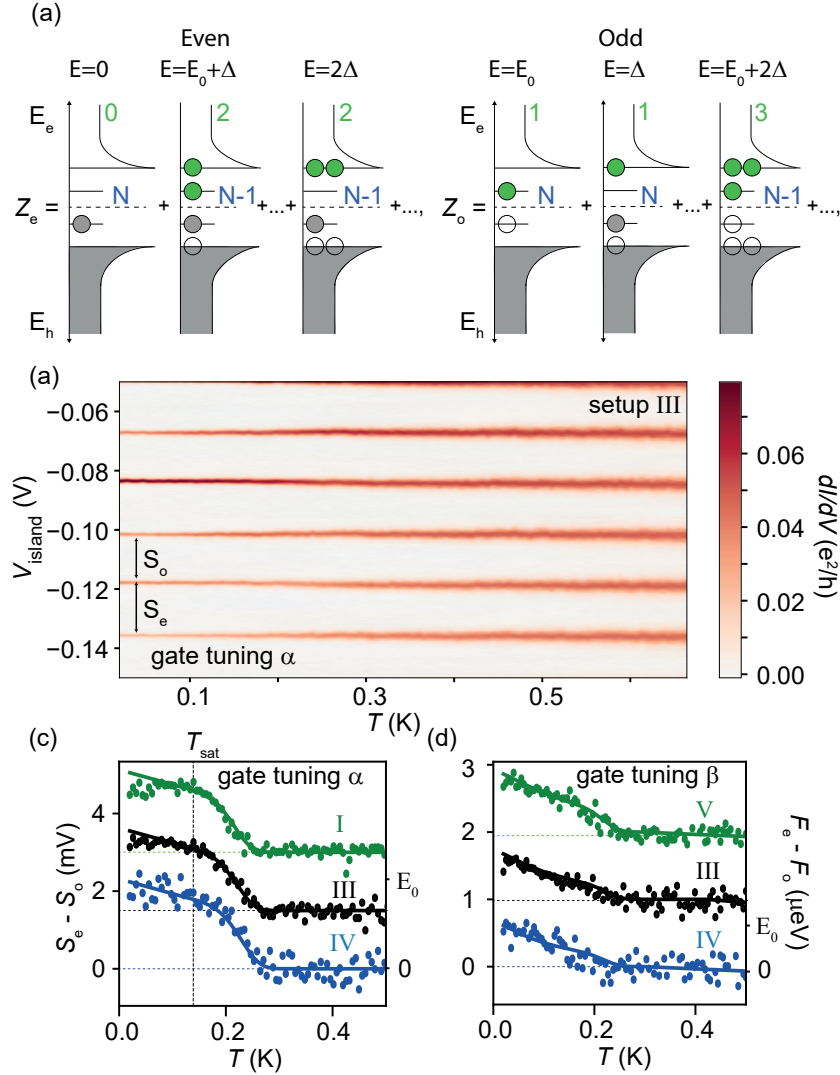
Figure 6.4: (a) Partition function elements Z_e and Z_o for even and odd occupation of the island, respectively. The first term in the left (right) schematic sum corresponds to the case of zero (one) quasiparticle (QP) on the sub-gap state and N number of Cooper pairs on the island. The electron(hole)-like excitation of a QP is pictured as a green solid circle (hollow circle). QP excitations at the gap edge ($\pm\Delta$) or to the sub-gap state E_0 are related to breaking a Cooper pair (N$\rightarrow$N-1). Green numbers refer to the total number of QP for a given configuration. Blue labels, N and $N-1$, correspond to the number of Cooper pairs. Energies on each schematic correspond to the energy cost required to realize the respective configuration. Gray color represents filled states. Non-degenerate sub-gap state is assumed. (b) Temperature dependence of island resonances measured in setup III and gate tuning α. Double headed arrows indicate the size of the analyzed even and odd sectors. (c,d) Difference of even-odd sectors as a function of temperature for three different setups measured in gate tuning α and β respectively. Solid lines are fits of the free energy difference using Eq. S1.

nances [13]. The temperature modifies the free energy difference between the odd and even states as $F_o - F_e = -k_B T \ln\left(\frac{Z_o(T)}{Z_e(T)}\right)$, where $Z_o(T)$, $Z_e(T)$ are the partition functions for odd and even states. In Fig. 6.4(a), we have drawn the first terms of each partition function, corresponding to the ground state and the first excited states for even and odd occupation of the SI. Excited configurations occur by breaking a Cooper pair and exciting the electrons at the continuum edge or at the sub-gap state (N→ N-1, where N is the number of Cooper pairs), or by exciting quasiparticles from E_0 to the continuum edge. Naturally, configurations that involve a large number of excited electrons cost more energy. For low temperatures, only the first terms of the partition function play a role. Thus, $Z_e > Z_o$ yielding a finite $F_o - F_e$ value which remains nearly constant (saturated) up to a temperature T_{sat}. As the temperature is increased, the thermal excitation of quasiparticles to the continuum above the superconducting gap is gradually favored, reducing the relative weight of the first terms of Z_e and Z_o and increasing the relative weight of higher-order terms which, above T_{sat}, lead to a linear reduction $F_o - F_e$. Eventually, $Z_e = Z_o$, such that $F_o = F_e$.

We observe this two-sloped dependence in all two-terminal setups in which Coulomb peaks are visible. Figure 6.4(b) shows an example colormap of zero-bias differential conductance versus temperature and V_{island}, the latter swept in the same range as Figs. 6.2 and 6.3. The Coulomb peaks width, which is related to all four couplings and the Fermi distribution of the metallic leads, increases with temperature (full-width at half-maximum: 70 μeV at T=30 mK; 290 μeV at T=0.67 K) as expected. As a measurement of the temperature evolution of $F_o - F_e$ in this device, we extract the difference in peak spacings $S_e - S_o$ versus temperature from this colormap and from similar measurements with two-terminal setups I and IV, and plot the results in Fig. 6.4(c) with vertical offsets for clarity. The two-sloped temperature evolution of $S_e - S_o$ culminating in $S_e = S_o$ is evident in our data. The initial spacing difference is ≈ 2 mV (corresponding to a free energy difference $\Delta F \approx 35\ \mu eV$) and the spacings become indistinguishable ($S_e = S_o$) at $T \approx 280$ mK. We fit the data (solid lines) using $S_e - S_o = \frac{4}{\alpha e}(F_o - F_e)$, where α is the lever arm and the difference of the free energies is given by Eq. S1 in the SM. From the fit, we extract an estimate of Δ and E_0 of the same order for

73

all three setups (see Table 6.1 for details). This indicates that the same sub-gap state is probed by different two-terminal combinations. The fit is good for peak spacing data measured at different magnetic field, which changes the value of E_0 (see Fig. S5 in SM). By slightly changing the gate configuration of the device (gate tuning β), the two slopes in the temperature dependence of $S_e - S_o$ become similar (Fig. 6.4(d)). The fit to data taken with three different setups yields a lower sub-gap state energy $E_0 = 13 \pm 3$ μeV, from which we conclude that E_0 is also gate-tunable.

As the onset (i.e., T_{sat}) of the fast reduction of $S_e - S_o$ with temperature indicates quasiparticle population above the superconducting gap, previous studies have linked it with the number of quasiparticles $n_{qp}V_{Al}$ in the SI [13], where n_{qp} is the quasiparticle density and V_{Al} the volume of the aluminum island. In our device, $T_{sat} \approx 140$ mK, from which we extract $n_{qp}V_{Al} < 3 \cdot 10^{-3}$ (see Appendix C for estimation details), in agreement with previous findings for single-nanowire SIs [13].

Finally, we report measurements of the additional device shown in Fig. 6.1(c) where a smaller charging energy E_c of the SI (possibly caused by larger capacitances to the gates and electrodes) allows for Cooper-pair charging. Figure 6.5(a) presents a bias spectroscopy measurement using setup I as a function of V_{island}, from which $E_c \approx 110$ μeV and $E_0 \approx 130$ μeV are extracted, and therefore $E_c < E_0$. Single-electron excitations between even and odd charge parabolas (Fig. 6.1e) result in Coulomb diamond features where the lower tips of the diamonds do not touch zero bias (see dashed lines). However, due to significant couplings to the normal leads, a zero-bias signal becomes visible, as shown by the black trace taken along one of the crossings. The spacing between these faint zero-bias peaks is $2e$ periodic, indicating Cooper-pair charging in this regime. To confirm the $2e$ periodicity of the zero-bias peaks, we investigate their B dependence. An example of a two-terminal measurement using setup I is shown in Fig. 6.5(b), while Fig. 6.5(c) shows extracted peak positions versus B for three different two-terminal measurement setups. The $2e$-periodic resonances split and turn into $1e$-periodic ones at $B \approx 320$ mT for all setups, at which point $B \approx B_c$. No indications of quasiparticle poisoning are observed at low B [28]. It is worth noting that the interwire tunneling $\Gamma_{L,R}$ in Device B is lower than Device A (see Appendix C, Fig. C.9), possibly due to a larger spacing
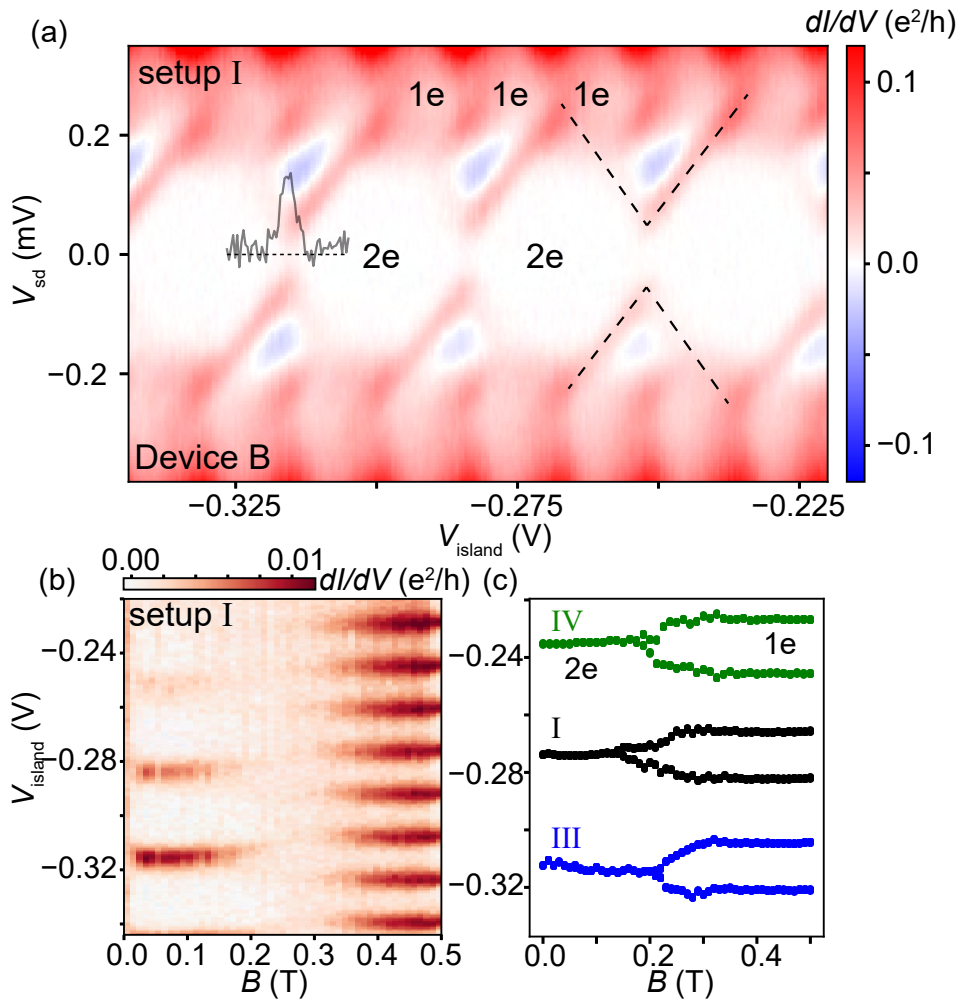
Figure 6.5: (a) Bias spectroscopy of an additional device in the $E_c < E_0$ regime. Two-electron periodicity is observed at low bias while one-electron periodicity is recovered at large bias. The overlaid black trace corresponds to the zero-bias conductance on the given gate segment. The peak conductance is $0.007 \, e^2/h$. (b) Zero-bias magnetic field dependence of the island resonances. Two-electron periodicity is transformed to one-electron periodicity due to the island becoming normal. (c) Peak positions for three different two-terminal setups showing the two-electron to one-electron transition of the SI.

between the nanowires, as seen in Fig. 6.1(c).

6.3 Conclusions

In this work we have characterized SI devices fabricated in an in-situ aluminum deposited double-nanowire platform. The main virtue of our double-nanowire SI devices is the presence of multiple terminals.

We performed two-terminal transport measurements similar to those used for single-nanowire SI devices to combinations of the multiple terminals of device A. The various two-terminal measurement combinations indicate the presence of a sub-gap state extended across the hybrid DNW SI as follows. First, Coulomb peaks with even-odd ground state parity alternation were observed at the same gate voltages in all setups where they were visible, indicating coupling to a common sub-gap state, however, with a background leakage between the end-end contacts preventing fully independent two-terminal setups. Second, NDC was observed in bias spectroscopy indicating the blocking of a quasiparticle relaxed by a sub-gap state. Third, the g-factor of the shifts of Coulomb peaks with B was estimated to be larger than that of pure Al, consistent with the shifts being due to the Zeeman splitting of a hybridized sub-gap state. Finally, a fit of the temperature dependence of the Coulomb peaks with a thermal model was used to extract the energy of the sub-gap state E_0 and the superconducting gap Δ for various two-terminal measurement setups, finding common values. The fit was done for a second gate setting (β), obtaining a common E_0 value as well, and the same Δ value as in the first setting (α), with the difference in E_0 in the two settings attributed to the influence of the gate on the InAs-Al hybridization [27]. The presence of independent sub-gap states in each NW would be distinguished by observing different energies in certain two-terminal configurations.

The relevance of delocalized states is in the long-range coupling possibilities which they provide. For example, a quasiparticle occupying a delocalized state can be used to couple localized spins in quantum dots via the Yu-Shiba-Rusinov mechanism across distances as long as the SI length [131].

Our devices exhibited different charging regimes, which enabled the study of the quasiparticle population with different methods. In Device A ($E_c > \Delta$ regime), the quasiparticle density was found to be comparable to that of single-nanowire SI devices [13]. In Device B ($E_c < \Delta$), no signs of quasiparticle poisoning were observed. Our double-nanowire platform thus shows promise for applications where parity conservation is required [14].

Despite the challenges of interwire coupling and low B_c, our devices comprise a step towards the realization of exotic proposals in

parallel nanowires coupled by superconductors [8–10, 58, 120] and alternative systems for multichannel Kondo phenomena [145–147]. The above limitations can be overcome by employing nanowires well separated from one another integrated by higher B_c superconductors such as Pb [139]. These advancements further our understanding of the sub-gap states (e.g. Yu-Shiba-Rusinov, Andreev bound states or Majorana zero-modes) hosted by parallel nanowires bridged by SIs. In particular, a new generation of devices showing $1e$ charging behavior in a large field range below B_c may shed light on the nature of the involved sub-gap state by investigating the predictions related to multichannel or topological Kondo phenomena.

<div style="text-align: right; font-size: 4em;">7</div>

ASYMMETRIC LITTLE-PARKS OSCILLATIONS IN FULL SHELL DOUBLE NANOWIRES

In this chapter we investigate a different utilization of double-nanowire hybrids, by coating them with an aluminum full-shell. The aim is to study the Little-Parks effect in these structures and investigate the similarities and differences of these systems to single nanowire Little-Parks devices.

7.1 Introduction

The recent observation of signatures of flux-induced topological superconductivity in individual semiconductor nanowires coated by a shell of superconducting Al has brought the Little-Parks (LP) effect into the spotlight [115, 148, 149]. The reduced dimensions of this core-shell system make possible interesting manifestations of this effect [150].

7. Asymmetric Little-Parks Oscillations in Full Shell Double Nanowires

The thinness of the shell results in fluxoid, rather than flux quantization [151, 152]. Depending on the ratio between the coherence length, ξ, and the diameter of the nanowire, d, which determines the diameter of the shell, the LP oscillations can either exhibit a reduced critical temperature, T_c, at half integer values of flux quantum Φ_0 (non-destructive regime, $\xi \ll d$), or $T_c=0$ (destructive regime, $\xi \gg d$). In the destructive regime [153], the application of a magnetic field perpendicular to the nanowire simultaneously with a field which threads magnetic flux through the shell can provoke the emergence of an anomalous metallic phase between nearby LP domes [150].

While the use of single nanowires for investigation of the LP effect is at an early stage [71, 115, 150, 154, 155], the use of double nanowires is still unheard of. Double nanowires covered by a half/full superconducting shell are of interest for exploring robust manifestations of topological superconductivity, such as Majorana zero modes, the topological Kondo effect and parafermionic modes [8, 9]. The realization of the two former could benefit from the advantages of the potentially vortex-induced topological superconductivity investigated in single-nanowire devices due to the LP effect [115, 116].

In hollow cylinders made of thin superconductor materials, including the nanowire shells described above, the applied magnetic field, B, needs to be properly aligned with the axis of the cylinder so as to maximize the critical field, B_c, at which the LP oscillations die out due to bulk destruction of superconductivity. This can be done by mechanical alignment of the sample to the axis of an external coil, or by field rotation using two-axis or three-axis vector coils to align the field with the sample orientation. Both of these ways of alignment are subject to error due to finite experimental resolution.

Here, we report the Little-Parks effect in closely-spaced InAs double nanowires fully covered by a thin epitaxial superconducting Al shell [19]. The nanowires are used as a template to shape the shell. Therefore, while the shell could potentially behave as two connected but individual hollow superconducting cylinders, we find in this work, by comparing our measurements to a mean-field model, that the shell actually behaves as a *single* cylinder. In addition to demonstrating the single-cylinder behavior of the shell of the nanowires, we show a way of inducing an asymmetry in the LP oscillations which relies on B mis-

80

alignment. As the single-cylinder model predicts the presence of the asymmetry for any misalignment, the degree of asymmetry can be used as an accurate measurement of the degree of misalignment of the field with the long axis of the sample. For completeness, we note that similar double nanowires, however, with only half-shell superconductor coverage are addressed in several parallel works [19, 54, 103].

7.2 Results

Setup

The InAs double nanowires are grown by the vapor-liquid-solid method, with Au droplets as growth catalysts. The growth is followed by in-situ Al epitaxy [19, 23]. A typical example of the as-grown Al-coated double nanowires is shown in the scanning electron micrograph Fig. 7.1a. Despite being grown from gold droplets which are separated by > 100 nm, the nanowires usually clamp together at their upper segments. The clamped part constitutes the bulk of the double nanowires and it is the part investigated in this work. Fig. 7.1b shows a transmission electron micrograph of a thin cross-sectional slice of the clamped part of a double nanowire. The two nanowires (in black) have an hexagonal cross section with six facets each. They are covered by Al (in grey) on their five exterior facets. Their remaining facets face each other with a small relative misalignment. There is no substantial Al in between. The inset schematics in Fig. 7.1a show the possible relative orientations of the nanowires: 1) facet-to-facet (F-F), as in Fig. 7.1b, and 2) corner-to-corner (C-C). The relative orientations are chosen by properly designing the positions of the gold droplets through electron beam lithography; however, the exact relative positions are subject to variability [19]. The primary sources of misalignment may relate to the Au particle formation mechanism and to Au particle diffusion. Slices such as the one in Fig. 7.1b taken from other double nanowires show different relative placement and distances between the nanowires, reflecting this variability and the possibility that the nanowires do not fully clamp before the Al is deposited. Both C-C and F-F devices were investigated, with no significant differences found in most devices.
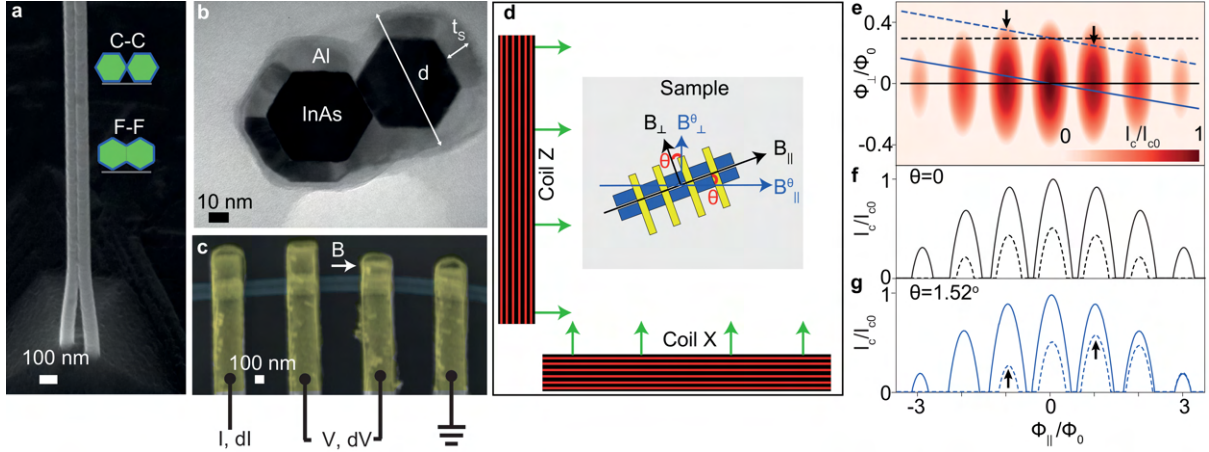
Figure 7.1: Experimental setup and model for asymmetric Little-Parks effect. (a) Scanning electron micrograph of as-grown InAs double nanowire covered with in-situ deposited epitaxial Al. The inset shows two possible relative configurations of the six-faceted nanowires. **(b)** Transmission electron micrograph of a $\approx$ 80 nm-thick slice of double nanowires. **(c)** False-colored scanning electron micrograph of a device. **(d)** Schematics of the magnetic field setup. **(e-g)** I_c dependence on parallel and perpendicular magnetic fluxes calculated with a single hollow superconducting cylinder model, showing an asymmetric Little-Parks effect due to field misalignment in the case of the dashed blue curve. See text for details.

To characterize the Little-Parks effect in the superconducting Al shell of the double nanowires, we performed four-terminal differential resistance, dV/dI, measurements in current-biased mode in devices with the layout of the one shown in the scanning electron micrograph of Fig. 7.1c. The measurements were done in a dilution refrigerator with a base temperature of T = 30 mK. In the devices, the Al shell was contacted with Ti/Au leads following milling of the native Al oxide. To record dV/dI, a device was biased with a small lock-in excitation dI = 10 nA superposed to a DC current I, and the ensuing AC and DC voltage drops, dV and V, were measured with a lock-in amplifier technique and a digital multimeter, respectively.

Using a two-axis vector magnet, we apply on the sample an external magnetic field, **B**, which can be divided into parallel, $B_{\parallel}$, and perpendicular, $B_{\perp}$, components to the axis of the double nanowires. $B_{\parallel}$ is used to thread flux through the shell of the nanowires for the LP effect and to eventually fully destroy superconductivity at $B_{c\parallel}$, the parallel critical field of the shell, while the only role of $B_{\perp}$ is to suppress superconductivity until full destruction at $B_{c\perp} \ll B_{c\parallel}$. **B** is nominally

82

applied in the plane of the sample; a small out-of-plane misalignment should not alter qualitatively the conclusions presented here. The setup is schematically shown in Fig. 7.1d. Nominally, $B_\parallel$ is perfectly aligned to the long axis of the sample, while $B_\perp$ is orthogonal to this direction. These two directions are represented by black arrows in Fig. 7.1d. We denote as $B_\parallel^\theta$ and $B_\perp^\theta$ the two components of **B** which are instead misaligned by an angle θ from $B_\parallel$ and $B_\perp$, respectively. The effect of such misalignment is systematically studied.

Single-cylinder model and expected asymmetries in Little-Parks oscillations

Little-Parks oscillations of T_c are expected to follow a $T_c(B) = T_c(-B)$ symmetry. This symmetry can be exceptionally broken in the vicinity of a hysteretic ferromagnet [156,157]. Here, we discuss instead an intrinsic asymmetry of LP oscillations due to minor field misalignment that may occur in experiments. To show the expected effect of the misalignment angle θ on the LP oscillations, we employ the hollow thin-walled superconducting cylinder model used before in Ref. [150] to fit LP data in single InAs nanowires coated by an Al shell [21,158,159]. In this model, $T_c(\mathbf{B})$ is provided by

$$\ln\left(\frac{T_c(\alpha)}{T_{c0}}\right) = \Psi\left(\frac{1}{2}\right) - \Psi\left(\frac{1}{2} + \frac{\alpha}{2\pi T_c(\alpha)}\right) \tag{7.1}$$

where Ψ is the Digamma function [20] and $T_{c0} = T_c(\mathbf{B} = 0)$. The Cooper-pair breaking parameter [158, 160, 161], $\alpha = \alpha_\parallel(B_\parallel) + \alpha_\perp(B_\perp)$, contains the effects of both $B_\parallel$ and $B_\perp$ on T_c [29,162]:

$$\alpha_\parallel = \frac{4\xi^2 T_{c0}}{A_\parallel}\left[\left(n - \frac{\Phi_\parallel}{\Phi_0}\right)^2 + \frac{t_s^2}{d_F^2}\left(\frac{\Phi_\parallel^2}{\Phi_0^2} + \frac{n^2}{3}\right)\right], \quad \alpha_\perp = \frac{4\xi^2 T_{c0}}{A_\perp}\frac{\Phi_\perp^2}{\Phi_0^2} \tag{7.2}$$

The LP oscillations are encoded in $\alpha_\parallel(B_\parallel)$ given in Eq. 7.2, where ξ is the coherence length, d_F is the diameter of the cylinder, t_s is its wall thickness, $\Phi_\parallel = B_\parallel A_\parallel$ is the magnetic flux threading the cylinder of cross section $A_\parallel = \frac{\pi}{4}d_F^2$, and n is the number of flux quanta threaded through the cylinder. The first term in $\alpha_\parallel(B_\parallel)$ oscillates with $\Phi_\parallel$ and

attains a maximum for half-integer $\frac{\Phi_\parallel}{\Phi_0}$, while it is zero for integer values
of this ratio. In ultra thin-walled cylinders (i.e., $t_s/d_F \ll 1$), it dominates
over the second term. If the t_s/d_F ratio cannot be neglected, as it is the
case in our devices, then the second term provokes small shifts of the
LP T_c maxima. In turn, the Cooper-pair breaking effect of $B_\perp$ is given
by $\alpha_\perp(B_\perp)$ in Eq. 7.2, where $\Phi_\perp = B_\perp A_\perp$, and $A_\perp$ [163] is a free fitting
parameter.

To convert the misaligned fields $B_\parallel^\theta$ and $B_\perp^\theta$ shown in the scheme in
Fig. 7.1d into $B_\parallel$ and $B_\perp$, we use:

$$B_\parallel = \left[B_\parallel^\theta cos(\theta) - B_\perp^\theta sin(\theta) \right], \ B_\perp = \left[B_\parallel^\theta sin(\theta) + B_\perp^\theta cos(\theta) \right] \quad (7.3)$$

The critical current, I_c, which is the main quantity that we measure
in our devices, is modulated by the effective critical temperature $T_c(\alpha)$
due to the variation of the Cooper pair breaking terms introduced above
[150, 164]:

$$I_c(\alpha) = I_{c0} \left(\frac{T_c(\alpha)}{T_{c0}} \right)^{3/2} \quad (7.4)$$

where I_{c0} and T_{c0} (critical current and temperature for $\mathbf{B} = 0$) are
renormalization constants to satisfy boundary conditions. An experi-
mental justification for Eq. 7.4 is shown in Fig. D.3 of Appendix D.

In Fig. 7.1e, we show a calculated colormap of I_c versus $\Phi_\parallel$ and $\Phi_\perp$.
The colormap shows oscillations of the magnitude of I_c against $\Phi_\parallel$, and
a monotonic I_c reduction against $\Phi_\perp$. The oscillations come as a direct
consequence of the LP oscillations of T_c.

Lines in Fig. 7.1e indicate four types of $\mathbf{B}$ trajectories provided by
the vectorial combination of $B_\parallel$ and $B_\perp$. In Fig. 7.1f, we show the I_c
dependence in trajectories for $\theta = 0$, i.e. zero field misalignment. These
trajectories either cross the origin in Fig. 7.1e, as in the case of the solid
black line ($B_\perp = 0$), or are parallel to the horizontal axis, as in the case
of the dashed black line ($B_\perp > 0$). The corresponding oscillations of I_c
are perfectly $\pm\Phi_\parallel$-symmetric.

The behavior of the I_c LP oscillations against $\Phi_\parallel$ is different when
$\theta > 0$, i.e., for finite field misalignment. Fig. 7.1g shows the case when

$\theta = 1.52°$. Whereas the tilted trajectory which crosses the origin in Fig. 7.1e, given by the solid blue line, still gives rise to perfectly $\pm\Phi_\parallel$-symmetric I_c oscillations in Fig. 7.1g, the tilted trajectory given by the dashed blue line which is shifted vertically by $B_\perp^\theta > 0$ results in strongly *asymmetric* LP oscillations. Black arrows in Figs. 7.1e,g point to asymmetries in the height of the first LP lobes best seen in the dashed blue curve in Fig. 7.1g. In the same curve, due to misalignment, the second and third lobes at negative $\Phi_\parallel$ are absent. A secondary consequence of finite misalignment is that, even for $B_\perp^\theta = 0$, the magnitude of the LP lobes away from $\Phi_\parallel = 0$ is always smaller than for perfect alignment; e.g., compare the solid blue curve in Fig. 7.1g with the solid black curve in Fig. 7.1f.

Single-cylinder behavior in double nanowires

Before discussing asymmetries in the Little-Parks oscillations in the measured data, we first demonstrate the single hollow superconducting cylinder behavior of the superconducting shell of the investigated double-nanowire devices by fitting our experimental results to the above model. To do this, we focus on the well-established symmetric LP effect at $B_\perp = 0$ in a device in the non-destructive regime.

In the colormap of Fig. 7.2a, dV/dI is plotted as a function of $B_\parallel^\theta$ and I, for $B_\perp = 0$. The boundary of the white-color lobes, inside of which $dV/dI = 0$ or $dV/dI \approx 0$ and outside of which $dV/dI = R_N$, the normal-state resistance, corresponds to LP oscillations of the critical current, I_c. These are dependent on T_c. Data showing oscillations of T_c is shown in Appendix D. The I_c oscillations are nearly symmetric in $B_\parallel^\theta$, with small asymmetries related to a finite small (< 20 mT) remanence in the X and Z coils of the vector magnet.

By fitting the measured I_c to the corresponding values calculated by our model (dashed lines in Fig. 7.2a), we obtain $\theta = 1.54°$. The good quality of the fit indicates that the superconducting Al shell of the two nanowires can be faithfully described as a single shell, despite the ellipsoidal cross section [165]. To produce the fit, we equate d_F with an effective cylinder diameter d^*, which corresponds to the diameter of a circle with the same area as the cross section of the two nanowires. Fit
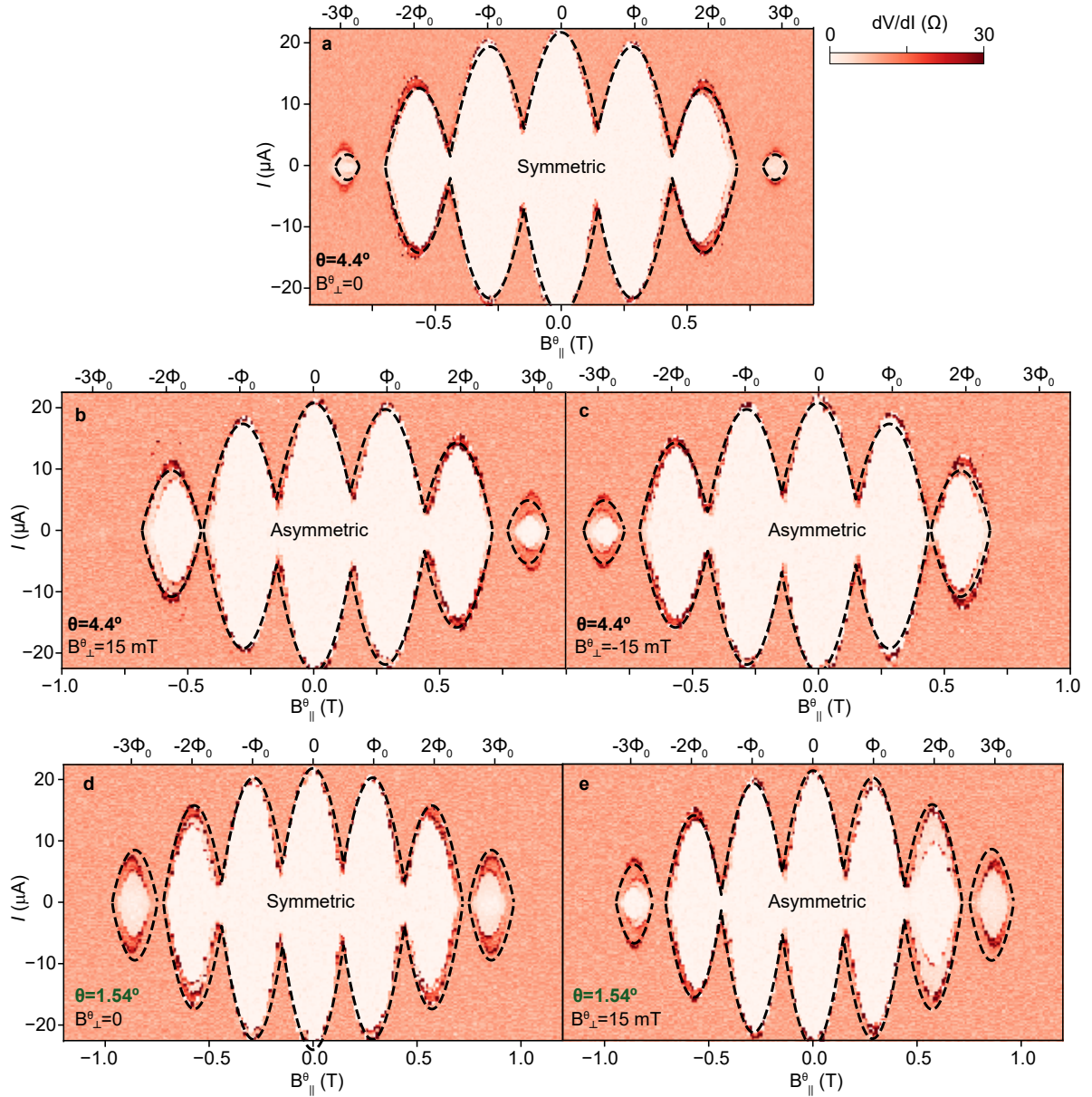
Figure 7.2: Evidence for single hollow superconducting cylinder behavior and asymmetric Little-Parks effect in the non-destructive regime (Device 1). (a-e) Colormaps of differential resistance, dV/dI, versus DC bias current, I, and magnetic field approximately parallel to the axis of the double nanowires, $B^\theta_\parallel$, with a small misalignment angle θ indicated in each plot. A small, constant magnetic field approximately perpendicular to the axis of the double nanowires, $B^\theta_\perp$, misaligned by the same angle θ, was also applied in (b,c,e), as indicated in each of these plots. Dashed lines in (a-e) are calculations of critical current, I_c, using the single hollow superconducting cylinder model. Fit parameters are given in Tab. 7.1.

parameters are provided in Tab. 7.1. In the single cylinder model, the

86

Table 7.1: Model parameters used to fit data of Devices 1 and 2 in Figs. 7.2 and 7.3. From left to right, coherence length (ξ), effective perpendicular flux area ($A_\perp$), effective parallel flux area ($A_\parallel$), and ratio of shell thickness (t_s) to effective single cylinder diameter (d^*). For parameter extraction methods, see Methods.

Device	ξ (nm)	$A_\perp$ (nm^2)	$A_\parallel$ (nm^2)	t_s/d^*
1	66	18000	7100	0.131
2	81	23080	5718	0.1

ratio d^*/ξ determines whether destructive (for $d^*/\xi < 1.2$, $T_c = 0$ at $\frac{\Phi_\parallel}{\Phi_0} = n/2$) or non-destructive (for $d^*/\xi > 1.2$, $T_c > 0$ at $\frac{\Phi_\parallel}{\Phi_0} = n/2$) regimes arise [158]. In Appendix D, we compile the d^*/ξ ratio obtained from fits with our model in five different double-nanowire devices, and show that this prediction holds also well in our devices. The quality of these fits indicates that these five devices behave as single hollow superconducting cylinders.

7.3 Asymmetric Little-Parks effect in the non-destructive and destructive regimes

In this section, we present experimental evidence for strong asymmetries of the Little-Parks oscillations of I_c. The asymmetries emerge when, in addition to $B_\parallel^\theta$, the parallel magnetic field misaligned by an angle θ, we apply $B_\perp^\theta$, a small perpendicular magnetic field misaligned by the same angle θ (refer to the sketch of the setup in Fig. 7.1d). As a result, the total magnetic field vector has different orientation for positive and negative values, which naturally creates a non-symmetric result in the B axis. We first study the non-destructive regime (Device 1) by comparing Little-Parks measurements for two different $B_\perp^\theta$ values and varying the misalignment angle θ. Secondly, we investigate the asymmetry effect in the destructive regime (Device 2) by instead increasing $B_\perp^\theta$ for a fixed misalignment angle θ.

Figure 7.2b shows the effect on the LP data of applying $B_\perp^\theta = 15\,\mathrm{mT}$ on the sample. In contrast to Fig. 7.2a, which shows approximately symmetric LP I_c oscillations measured at $B_\perp^\theta = 0$ mT, the data in Fig. 7.2b shows strong $\pm B_\parallel^\theta$ asymmetries in the LP oscillations. The lobe at $-3\Phi_0$

present in the symmetric case of Fig. 7.2a is missing in the asymmetric case in Fig. 7.2b, whereas the lobe at $+3\Phi_0$ in Fig. 7.2b is larger than the corresponding lobe in Fig. 7.2a. As shown in Fig. 7.2c, if the direction of $B_\perp^\theta$ is reversed, the LP asymmetries are mirrored along the vertical axis.

A decrease in the misalignment angle θ has two important consequences: 1) The size of the last lobe increases, due to a smaller effective perpendicular field. This is evidenced in the comparison of Fig. 7.2d for $\theta = 1.54°$, which shows larger lobes at $\pm 3\Phi_0$ than Fig. 7.2a, for $\theta = 4.4°$. 2) The degree of asymmetry decreases. To put this in evidence, Fig. 7.2e for $\theta = 1.54°$ and $B_\perp^\theta = 15$ mT can be compared with Fig. 7.2b for $\theta = 4.4°$ and the same $B_\perp^\theta$ value. The missing lobe at $-3\Phi_0$ in Fig. 7.2b reappears in Fig. 7.2e for smaller misalignment.

Our single-cylinder model fully accounts for the observed asymmetries, with θ as the only parameter which is varied; $\theta = 4.4°$ in Figs. 7.2a-c and $\theta = 1.54°$ in Figs. 7.2d,e. Other parameters are the same as those used to fit the data in Fig. 7.2a, given above.

Out of five measured devices, two were found to be in the destructive regime (see Appendix D). Here, we investigate asymmetric Little-Parks oscillations in Device 2, which lies in this regime. The observed phenomenology is similar to that in the non-destructive regime, aside from full destruction of superconductivity at half-flux quanta ($I_c = 0$ at $n\Phi_0/2$).

Figs. 7.3a-d show the evolution of the measured LP oscillations in this device with increasing $B_\perp^\theta$, for fixed θ. In Fig. 7.3a, at $B_\perp^\theta = 0$, the oscillations are approximately symmetric in $\pm B_\parallel^\theta$. In Fig. 7.3b, at $B_\perp^\theta = 10$ mT, the lobes at negative $B_\parallel^\theta$ are significantly more pronounced than those at positive $B_\parallel^\theta$. The asymmetry increases significantly in Fig. 7.3c at $B_\perp^\theta = 50$ mT, with the $2\Phi_0$ and $3\Phi_0$ lobes absent at positive $B_\parallel^\theta$, and the lobe at $-\Phi_0$ becoming larger than the zeroth lobe. In Fig. 7.3d, at the largest $B_\perp^\theta$ shown, $B_\perp^\theta = 75$ mT, all positive $B_\parallel^\theta$ are absent and the zeroth lobe turns faint in comparison to the $-\Phi_0$ and $-2\Phi_0$ lobes.

Our model of I_c, shown as dashed lines in Figs. 7.3a-d, matches reasonably well the behavior of the lobe boundaries as $B_\perp^\theta$ is increased with a single set of fitting parameters, shown in Tab. 7.1.
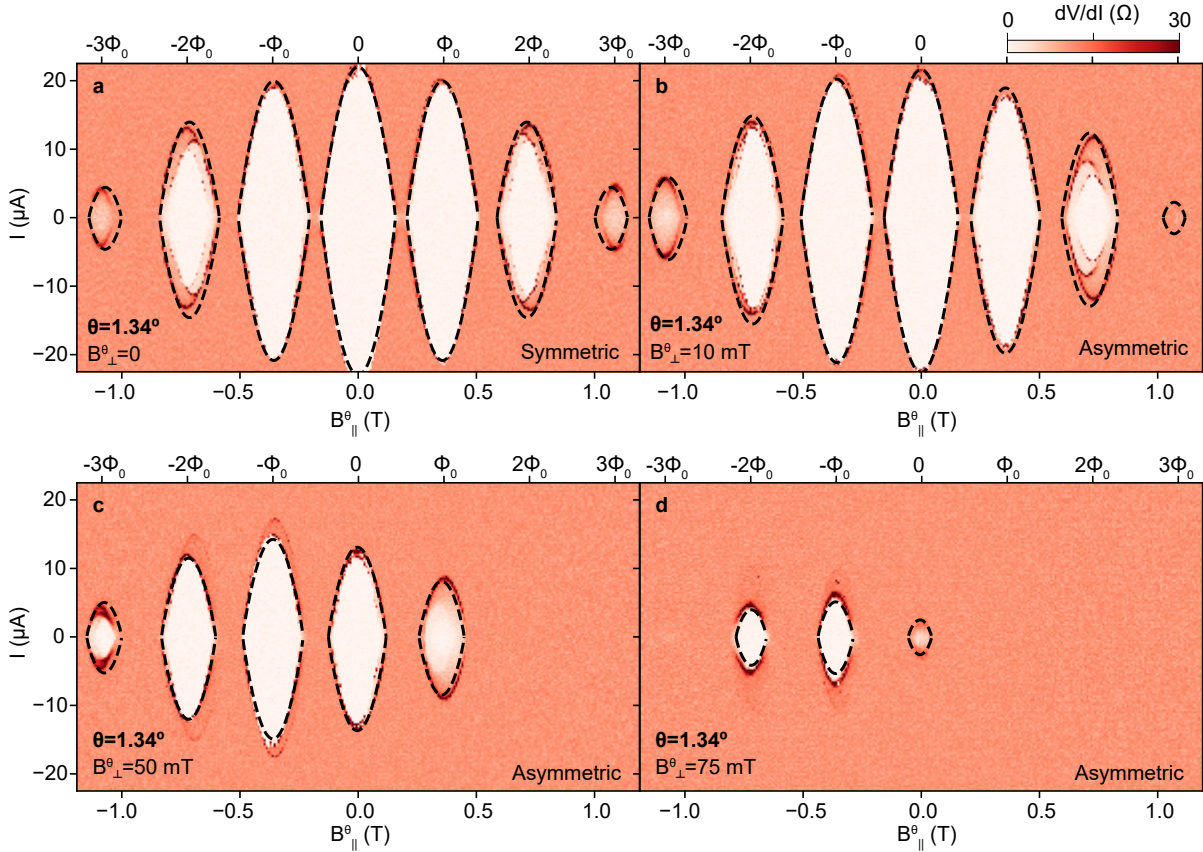
Figure 7.3: Asymmetric Little-Parks effect in the destructive regime (Device 2). (a-d)
Little-Parks data and fit for Device 2, akin to those shown in Figs. 7.2a-c. The misalignment angle $\theta = 1.34°$ is kept fixed in (a-d). The misaligned perpendicular field, $B_\perp^\theta$, is progressively increased as indicated in each panel, leading to an increased asymmetry in the Little-Parks oscillations of the critical current, I_c. Fit parameters are given in Tab. 7.1.

7.4   Discussion

We reported the Little-Parks effect in a new hybrid superconducting platform, consisting of double semiconductor nanowires coated by a superconducting shell. While the semiconductor nanowires were used here only as a template to shape the shell, they can in principle be used in future experiments to explore topological superconductivity in setups involving two hybrid Rashba nanowires [8, 9], using the recent findings involving the LP effect in single hybrid Rashba nanowires coated by a superconducting shell as a starting point [115]. The hybrid Rashba cores could also be used to extend investigations of Yu-Shiba-Rusinov states in quantum dots coupled to single core-shell

nanowires [71].

We found that, despite their double-nanowire template, the superconducting shell behaved as a *single* hollow superconducting cylinder. Both the destructive and non-destructive LP regimes were observed, indicating a smaller superconducting coherence length in the latter case, and variations in the diameter of the nanowires. In the presence of a small misalignment of the applied parallel and perpendicular magnetic fields with respect to the nominally aligned parallel and perpendicular directions to the axis of the nanowires, the LP oscillations showed strong *asymmetries* in the parallel field direction with respect to zero field. These strong asymmetries may be used to calibrate the alignment of the field with the axis of the nanowires, so as to maximize the critical field of the superconductor and thus maximize the observed number of LP oscillations. Given that a single cylinder model is used to model these asymmetries, the asymmetries are also expected to be present in *single* nanowires coated by a superconducting shell.

To convert parallel and perpendicular magnetic fields to magnetic fluxes, our model uses different parameters, $A_\parallel$ and $A_\perp$ [163], with $A_\parallel < A_\perp$, in contrast to a previous study in single nanowires coated by superconducting shells, in which $A_\parallel = A_\perp$ [150]. While $A_\parallel$ is interpreted as the cross section of the two nanowires, the physical meaning of $A_\perp$ is not presently understood beyond the phenomenological requirement that $A_\parallel < A_\perp$ to explain the lower perpendicular critical field of the samples (see Fig. D.2 in Appendix D). As expected, the parameter $A_\perp$ does not depend on the length of the shell, as shown in Fig. D.1 in Appendix D. We note that the model is expected to deviate from the data for field perpendicular to the axis of the nanowires due to the hexagonal cross section of the two nanowires serving as template for the shell, which is different from a strictly circular cross section. The deviation is less important for parallel field, as in this case the field is aligned to the facets of the shell.

The data in Figs. 7.2 and 7.3 shows additional switching currents at currents above the first switching identified as the critical current. A clear example of additional switchings is seen in Fig. 7.3a in the $-2\Phi_0$ lobe. The additional switching currents form a series of higher lobes, which are shifted leftwards or rightwards with respect to the main LP lobes, given by the first switching. The origin of these lobes, which have

been previously observed in single nanowires coated by superconducting shells [150], is beyond the single cylinder model. We speculate that the origin of these additional switchings is related to the superconductor under or close the ohmic contacts being damaged by the fabrication process (argon milling). The damaged regions may have different T_c than the pristine aluminum shell and that can be the origin of the additional switchings observed. Moreover, inhomogenities along the nanowire shell may lead to change in parameters (e.g. shell thickness).

Furthermore, the Little-Parks analysis presented does not take into account the proximity and inverse-proximity effects in our hybrid nanowires, which may affect the effective superconducting cross-sectional area. As we lack precise knowledge (transmission electron microscope micrographs) of the transverse area of the double nanowire devices measured, we cannot quantitatively compare it to the extracted superconducting cross-sectional area ($A_\parallel$). We note that a recent experimental work on partially covered InAsSb nanowires shows Little-Parks effect via circumferential proximity effect in the uncovered nanowire region [166], which is geometrically different from the (radial) proximity effects in our full-shell devices.

The clamping of the upper segments of these nanowires, which appears to be responsible for the observed single shell behavior, may be avoided by the growth of thicker, less flexible double nanowires [19]. Independent Little-Parks oscillations in the two nanowires may aid in attaining independent pairs of flux-induced Majorana zero modes in each nanowire, while the shared phase winding demonstrated in this work may be of utility to further characterize Majorana zero modes.

7.5   Methods

Here we describe the obtention of the parameters given in Tab. 7.1, used to fit the data from Devices 1 and 2 in Figs. 7.2 and 7.3 with the single hollow superconducting cylinder model. As the template for the superconducting shell in our devices consists of two nanowires of hexagonal cross section, we converted geometric device parameters into effective single cylinder parameters. The diameter of each nanowire was estimated from the transmission electron micrograph in Fig. 7.1b at $d \approx 90$ nm (including the Al shell). The area $A_\parallel$ of two hexagons of this diame-

91

ter equals the area of a circle with a diameter $d^* \approx 130$ nm. Additionally, from the same electron micrograph, we obtained $t_{\mathrm{s}} = 13$ nm. The parameters θ, ξ and $A_{\perp}$ were kept free. Two distinct sets of values for these parameters were found by fitting the corresponding multiple sets of data for Devices 1 and 2 in Figs. 7.2 and 7.3. The experimentally measured values of $A_{\parallel}$, d^* and t_{s} were further fine-tuned for a good fit to the data.

8

INTERACTION OF A SUPERCONDUCTING ISLAND WITH A MAGNETIC IMPURITY

This chapter escapes the scope of double-nanowire hybrids and investigates a special system where a superconducting island is coupled to a magnetic impurity in a single InAs nanowire. Traditionally, superconductors have been vastly investigated in close proximity with magnetic impurities [2–5, 25, 42, 43, 51, 88], but a finite charging energy E_c changes the physics of the system. We report charge stability diagrams of the quantum dot-superconducting island system (QD-SI) and bias spectroscopy measurements revealing asymmetric features owing to the $E_c \approx \Delta$ regime that the SI is tuned into and the single-level character of the QD. These findings are supported by a theoretical model developed by Pavešić et al. [44].

8.1 Introduction

Large superconducting objects coupled to magnetic impurities give rise
to an exchange interaction between quasiparticles in the superconduc-
tor and the magnetic impurity, forming a Yu-Shiba-Rusinov singlet
state [2–5, 43]. For strong enough coupling, this state becomes the
ground state of the system. While these effects are well understood,
a system where the Coulomb repulsion is significant in the supercon-
ductor has not been investigated. To achieve that, one may decrease
the size of the superconducting object to introduce an energy gap for
adding electrons, the Coulomb repulsion E_c. Interaction of such a su-
perconducting island with a magnetic impurity is of high significance
as superconducting islands have been studied in several experimental
setups [13, 14, 28, 36] and are relevant for other directions such as the
superconducting analogue of the multichannel Kondo effect [167–169].

In the absence of a magnetic impurity, the SI demonstrates 2-
electron (Cooper pair) transport for $E_c < \Delta$, while for $E_c > \Delta$ single-
electron charging is present [13, 36, 170].

In this work we include a magnetic impurity by forming a tunable
QD in a nanowire and we investigate the zero-bias charge degeneracy
map of the system. Furthermore, the bias spectroscopy reveals asym-
metric features owing to the finite $\frac{E_c}{\Delta}$ ratio and the large level spacing of
the QD. Finally, different $\frac{E_c}{\Delta}$ regimes are explored, showing the evolu-
tion of QD-SI system between limits of $\frac{E_c}{\Delta}$.

8.2 Results

Figure 8.1a shows an SEM image of the studied device. An InAs
nanowire with nominal width $\approx$110 nm and 7 nm aluminum thickness
is deposited on a Si/SiO$_2$ substrate. Selectively etching of the aluminum
is performed with standard electron beam lithography techniques using
transene-D as the etchant. Ohmic contacts are deposited and a dielec-
tric HfO$_2$ layer is deposited using ALD to insulate the nanowire from
the topgates. For more fabrication information see Chapter A. Five top-
gates are used, V_L and V_R are used to form tunnel barriers between the
ohmic contacts and the QD and SI respectively, while V_N and V_S tune the
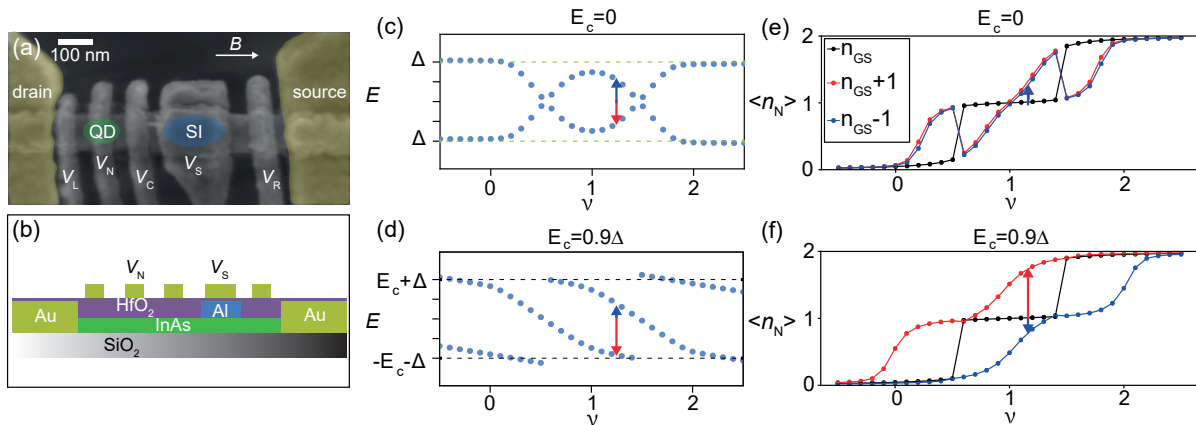
Figure 8.1: (a) SEM image of a QD-SI device fabricated on a single InAs nanowire. Ohmic contacts are false-colored (yellow) and five topgates are used to define tunnel barriers and tune the level of the QD and the SI. (b) Cross section schematic of the device. Selective etching of the aluminum forms a $\approx$350 nm long, 7 nm thick aluminum island. A 6 nm thick HfO_2 layers insulates the device from the designed topgates. (c) First excitation spectrum corresponding to a grounded superconductor (E_c=0) coupled to a QD. Tuning ν which is the QD occupation forms the known sub-gap state spectrum where addition and removal of an electron (red and blue lines) cost the same energy (electron-hole symmetry). (d) The superconductor has finite charging energy $E_c = 0.9\,\Delta$ which creates an electron-hole *asymmetry* in the sub-gap state spectrum. (e) Occupation expectation values for n, n+1 and n-1 electrons in the system for E_c=0. For any ν the values of n+1 and n-1 are equal, agreeing with electron-hole symmetry. (f) Occupation expectation values for a QD-SI system with $E_c = 0.9\,\Delta$. Significant differences on $<n_N>$ are present which are maximized near the charge fluctuation points (i.e. $\nu = 1.45$). This asymmetry stems from the fact that the QD has one level, hence it can only be filled by two electrons. As a result, removing an electron (blue arrow) would cost $U + \epsilon_d$ where U is the charging energy of the QD and ϵ_d the position of the QD level, while an electron (red arrow) can only be added in the SI, paying $E_c + \Delta$. The calculations shown are made by Luka Pavešić.

levels of the QD and the SI. A middle gate V_C is used to tune the coupling between the two objects. A cross section schematic of the device is shown in Fig. 8.1b. Figure 8.1c,d shows a model calculation introducing the main difference in the physics which stems from the finite E_c of the superconductor. For E_c=0, a typical electron-hole symmetric sub-gate state spectrum is observed when tuning the QD between even and odd charge sectors. The blue arrow corresponds to the energy required to remove an electron (and access the excited state) and the red arrow to the energy required to add one, which is the electron-hole counterpart. These two energies seize to be equal when the superconductor has a

significant charging energy, as seen in Fig. 8.1d. More insight on this difference can be found in Figure 8.1e,f where the occupation expectation values are plotted for n, n+1 and n-1 electrons as a function of QD occupation ν. The n+1 and n-1 lines are superimposed for the E_c=0 case, showing that adding or removing a charge is indifferent. However, the finite E_c regime shown in Figure 8.1f causes a difference in the expectation value, which stems from the energy penalty required to add an electron to the SI. This effect is maximized near the charge fluctuation points (i.e. ν=1.45) as adding an electron to the QD would cost $U + \epsilon_d$ (red arrow), while removing one from the QD is not energetically efficient (due to the large level spacing) and is hence removed from the SI, paying $E_c + \Delta$ (blue arrow).
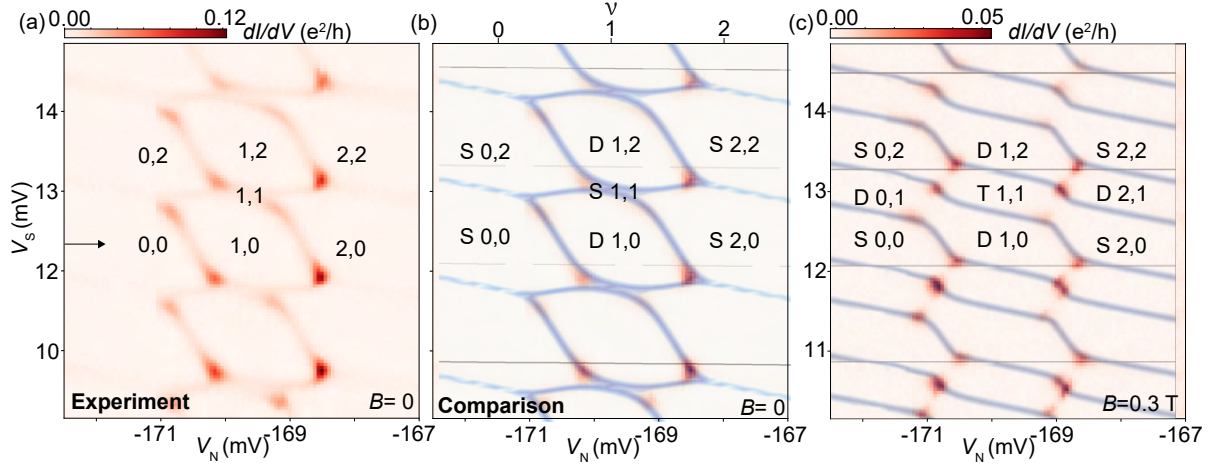
Figure 8.2: (a) Zero-bias differential conductance measurement as a function of the two plunger gates of the SI (V_S) and the QD (V_N). The other gates are set at V_L=-350 mV, V_C=-52 mV and V_R=-169 mV. A gate switch can be seen at $V_N \approx$ -171 mV, changing the conductance magnitude of the SI resonances. Numbers indicate the arbitrary occupation of the QD and the SI. The two-electron charging of the SI is disturbed when the QD has odd number of electrons, giving rise to Coulomb aided YSR singlet state (1,1 sector). (b) Comparison using a model with parameter shown in Table 8.1 yields good agreement with the data. (c) Calculation superimposed to experimental data measured at B=0.3 T. The 1,1 sector is enlarged owing to a singlet to triplet transition.

Next, we investigate the zero-bias conductance of the device, studying the charge stability diagram of the QD-SI system shown in Fig. 8.2a. Faint horizontal-like lines define the charge degeneracies of the SI, while the kinked vertical-like lines correspond to degeneracy lines of the QD. Numbers on the charge sectors correspond to the charge

Table 8.1: Parameters of the QD-SI device and model. Top-row parameters are estimates obtained from measurements, while the bottom-row ones represent best fits of the model output to the experimental data based on the measured parameters as the initial input for subsequent fine tuning.

Γ (meV)	U (meV)	E_c (meV)	Δ (meV)	V (meV)
0.05	0.8 -1.0	0.19	≤ 0.27	0.13
0.04	0.8	0.18	0.2	0.16

expectation value of the SI and the QD respectively. Note that this is an approximation as the total number is integer but each of the two occupation is not depending how close to a charge degeneracy the system is tuned. Small but resolvable 1,1 sectors are observed, which are created due to the YSR interaction between the SI and QD. Even though the SI is tuned in the $E_\mathrm{c} < \Delta$ regime (see Table 8.1) it is favourable for the SI to excite a quasiparticle in order to create a YSR singlet ground state. Figure 8.2b shows a model calculation superimposed on the experimental data. The model parameters are given in Table 8.1. Symbols S,D refer to the ground state of the system. Figure 8.2c shows a charge stability diagram measured at B=0.3 T to prove the spin character of the charge sectors and verify the charge expectation values shown in. Here, due to the Zeeman effect the doublet sectors (0,1 1,0 1,2 and 2,1) have grown in size as the parity lines are moving to expand the doublet sectors. The 1,1 sector has undergone a singlet to triplet transition, which results in an expansion of the 1,1 sector which is now clearly visible. As the coupling between the QD and the SI is weak, the triplet is probed at small magnetic fields. In contrast, the other sectors with even number of electrons (i.e 2,0) are still in a singlet ground state as the triplet involves adding an two electrons with the same spin on different levels of the QD. With these measurements we can verify that the QD has a well defined spin.

We now focus at the finite bias spectroscopy where superconducting Coulombic excitations (SCE) are observed. Figure 8.3a presents a bias spectroscopy measurement where the QD is tuned from 0 to 2 electrons. We observe that the SCE produce an S-shape spanning from V_sd= -0.37 $\rightarrow$ 0.37 meV. The extension of these features are obscured at larger bias due to the continuum edge. The SCE are inversion symmetric in position and conductance, as hinted by the two insert traces
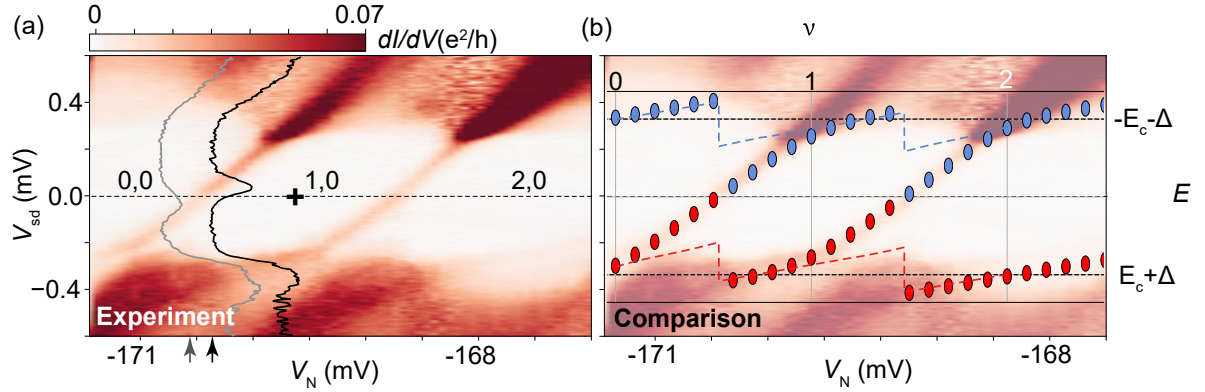
Figure 8.3: (a) Bias spectroscopy measurement tuning the QD following the arrow in Figure 8.2a. Numbers on the sectors correspond to the approximate charges on the QD and the SI. Bias asymmetric features reminiscent of Figure 8.1d is observed. Colorscale is saturated to highlight the superconducting Coulombic excitations. Gray and black arrows highlight the position where the superimposed conductance curves are measured. (b) Model calculation superimposed on the measured data. Red points correspond to addition of electrons and blue to removal. Dashed lines indicate the continuum edge.

(gray and black). The center of the 1,0 sector (marked with cross) highlights the symmetric point where it is equally energetically favorable to remove/add an electron from/to the QD resulting in equidistant SCE which are however obscured by the continuum edge. Figure 8.3b shows a superimposed calculation on the data, where red (blue) points correspond to removal (addition) of an electron. Colored dashed lines correspond to the continuum edge, which suffers discontinuities due to the charge redistribution near the charge fluctuation points (i.e. $v = 1.5$).

To further study the different SCE regimes, an additional device was measured in which the $\frac{E_c}{\Delta}$ ratio could be tuned. That device (see Appendix E) consists of a similar geometry to Fig. 8.1a, but it contains an additional SI in series, which for the aim of the current experiment has been coupled strongly to the closest lead, effectively making it a superconducting probe ($E_{cL} = 0$). Figure 8.4a shows a bias spectroscopy measurement tuning the QD where electron-hole symmetric sub-gap states are observed (gray dashed line). A replica of that state is observed at a higher energy elevated by Δ_L as the effective superconducting lead is probing the state (black dashed line). Inset shows a schematic of the device. The right panel shows a charge stability diagram of the gates tuning the QD V_N and the SI V_{SR}. Vertical lines are observed, corre-
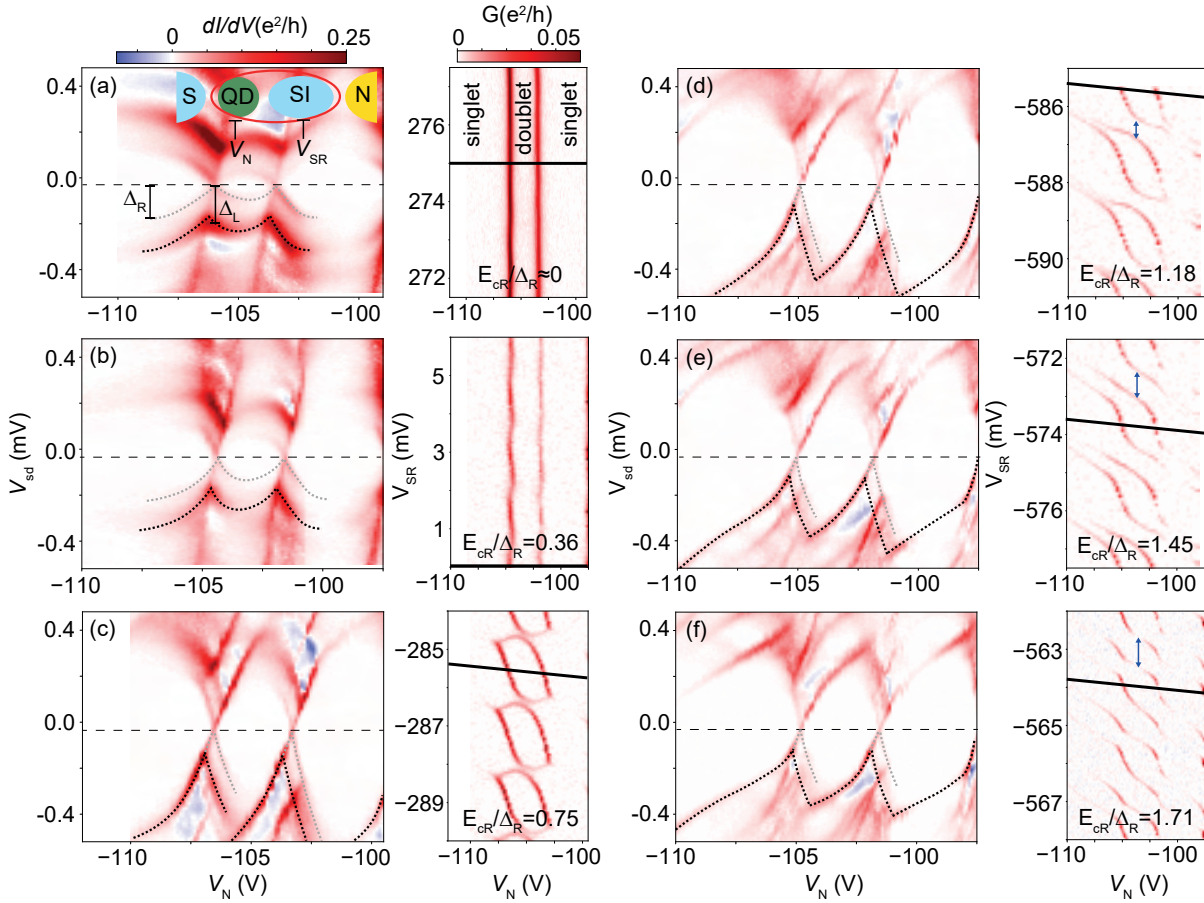
Figure 8.4: Series of bias spectroscopy measurements accompanied with the corresponding charge stability diagram for a QD-SI system tuned in several $\frac{E_{cR}}{\Delta_R}$ regimes. (a) $\frac{E_{cR}}{\Delta_R} \approx 0$. Minimum E_c causes the system to act as a QD coupled to an S lead since no change occurs in the charge stability pattern when tuning V_{SR}. The bias spectroscopy shows an electron-hole symmetric sub-gap state, reminiscent of a standard YSR state. (b-f) Increasing the $\frac{E_{cR}}{\Delta_R}$ ratio causes kinks to be introduced in the charge stability diagrams, recovering the QD-SI pattern studied in Fig. 8.2a. The "S" shape of SCE is also being recovered in the bias spectroscopy measurements. The other gates are set to: $V_{SL} = -50$ mV, $V_3 = -732.5$ mV, $V_5 = -300$ mV, $V_{bg} = -1.49$ V. Right SI parameters are: (a) $E_{cR} \approx 0$, $\Delta_R = 0.15$ meV, (b) $E_{cR} = 0.05$ meV, $\Delta_R = 0.14$ meV, (c) $E_{cR} = 0.12$ meV, $\Delta_R = 0.16$ meV, (d) $E_{cR} = 0.255$ meV, $\Delta_R = 0.215$ meV, (e) $E_{cR} = 0.255$ meV, $\Delta_R = 0.175$ meV, (f) $E_{cR} = 0.24$ meV, $\Delta_R = 0.14$ meV.

sponding to parity lines of the QD. Moving V_N from negative to positive voltage, the QD is changes parity from even (singlet), to odd (doublet) and again even (singlet) number of electrons. The V_{SR} has no effect on the pattern which is consistent with the SI having $\frac{E_{cR}}{\Delta_R} \approx 0$. Figure 8.4b,c presents measurements where the right SI is tuned accordingly in or-

der to increase the $\frac{E_{cR}}{\Delta_R}$ ratio and make SCE relevant. Small modulations
of the parity lines are observed in Fig. 8.4b while the excitations in the
bias spectroscopy measurement begin to tilt. Figure 8.4c presents clear
signatures of SCE as the S shape is recovered in bias spectroscopy and
there is also a clear dependence of the charge stability diagram to the
V_{SR}, with new stable ground states emerging such as the YSR singlet.
In the bias spectroscopy measurement, the YSR features have increased
in size, consistent with the increase of the energy gap $E_{cR} + \Delta_R$ by the
Coulombic contribution.

With further increase of the $\frac{E_{cR}}{\Delta_R}$ ratio the right SI is now tuned in
the regime where single electron charging is favourable, as the charging
energy is larger than the superconducting gap (Fig. 8.4d-f). A significant
difference in the SCE spectrum is that the size of the S shapes shrink is
size, due to the enlargement of the 1,1 sector (see blue double-headed
arrows). This occurs because for larger $\frac{E_{cR}}{\Delta_R}$, the states with one electron
in the SI are further stabilized.
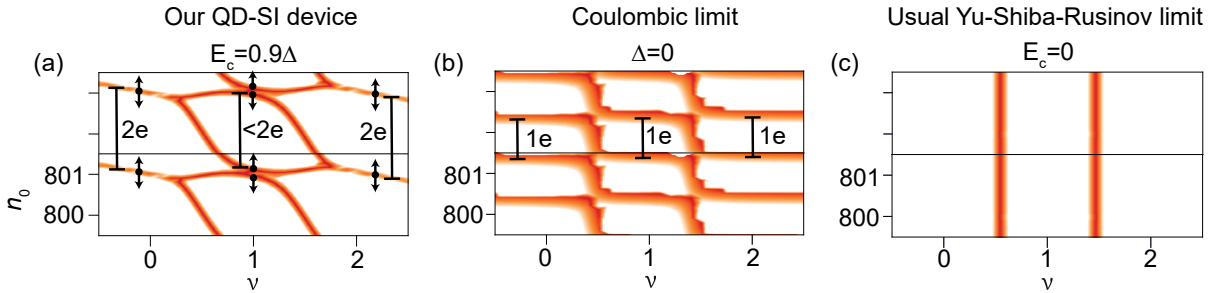
Figure 8.5: Calculations of ground state transitions for different E_c, Δ regimes for the
QD-SI system. (a) Calculation using the device parameters. As E_c is slightly smaller
than Δ, one-electron charge states are not stabilized unless there is an electron in the
QD. (b) Pure Coulombic limit (Δ=0) produces a one-electron spacing between each
charge sector regardless of the QD occupation. (c) YSR limit where the superconductor
has no charging energy produces the known transitions which are independent of the
number of electrons on the superconductor. These calculations are made by Luka
Pavešić.

In order to further understand the different regimes, Fig. 8.5
presents calculated diagrams of ground state transitions for different
E_c, Δ limits. Figure 8.5a shows a calculation using the parameters of the
measured device. For even occupation of the QD, each charge sector
has a vertical size of two-electrons. For odd occupation YSR physics are
relevant and the YSR singlet is stabilized, causing the doublet sectors to

100

shrink. For the Coulombic limit shown in Figure 8.5b, the YSR singlet has reached its full size and each charge sector has one-electron size, forming a honeycomb pattern. Figure 8.4f is reminiscent of this regime. For a grounded superconductor (E_c=0) the usual YSR pattern is recovered, as the transitions are independent of the number of electrons in the superconductor.

8.3   Conclusions

This chapter has presented a novel system where a superconducting island is coupled to a tunable magnetic impurity in a nanowire device. Superconducting Coulombic excitations have been observed, breaking the electron-hole symmetry of typical Yu-Shiba-Rusinov states in hybrid superconductor-quantum dot systems. Tunable $\frac{E_c}{\Delta}$ has been demonstrated in a second device, exploring the bias spectroscopy and charge stability diagrams from $\frac{E_c}{\Delta} \approx 0$ to $\frac{E_c}{\Delta} > 1$. The measurements are supported by a model of the system [44] yielding good agreement with relevant fit parameters. The understanding of SCE is vital for future applications involving coupled QDs with superconducting islands, such as an extended geometry involving a chain of SI-QD-SI which is proposed to host non-trivial overscreened states involving a spin on each object [171].

9

CONCLUSIONS AND OUTLOOK

This thesis has been inspired by the theoretical proposals involving parallel nanowires coupled to superconductors, which employ exotic phases such as the topological Kondo effect [9,10] and parafermions [8]. Throughout this thesis, double nanowires are introduced from the initial growth process until experimental realizations of various geometries. It has been found that the initial growth parameters of the double nanowires are crucial for the interwire tunneling and possible observation of crossed Andreev reflection processes. The Little-Parks effect has been demonstrated in full-shell double nanowires showing that a model describing a single superconducting cylinder provides a good fit for these devices. Furthermore, a study of superconducting islands bridging double nanowires has been conducted, showing charging of a sub-gap state via different two-terminal combinations. The temperature dependence of these resonances hints towards the presence of a common sub-gap state extending across the double nanowire superconducting island.

Even though the device geometries of the proposals [9, 10] have been experimentally realized, limitations of our nanowires such as low critical magnetic field and interwire tunneling prevents us from studying the 1e regime in the superconducting state and having full control of individual semiconducting channels.

In order to move a step forward towards the implementation of

the topological Kondo effect geometry, the focus should be put on more rigid nanowires (Type-I) which have a well-defined separation. This would make it more challenging to bridge the nanowires by a superconductor, making aluminum a poor choice. Therefore, alternative superconductors such as lead [139] or tin [138] can be investigated in these geometries. Having a higher critical magnetic field and well-defined separation between the nanowires which would minimize interwire tunelling can boost the pursuit of the topological Kondo effect.

Regarding pursuing of Crossed Andreev reflection in these geometries, the focus should be on different nanowire parameters, as it is essential that the distance between the two semiconducting channels is minimal (Type-II), and the nanowires shall be bridged by the superconductor. Therefore, one possible pathway is to create shadow mask during aluminum deposition, in order to evaporate the superconductor only in the junction of the two nanowires. This method may enhance the CAR process.

Furthermore, an alternative approach involves selective area grown (SAG) nanowires, which have the advantage that can be processed on the growth substrate. This characteristic unlocks vast device flexibility and makes it easier to form separated nanowires that are connected by thin layers of superconductors.

Escaping the scope of grown nanowires, the field of 2-dimension electron gases (DEG) has advanced, allowing the creation of flexible and high mobility nanostructures based on InAs/Al [126, 133]. These nanostructures are created by selective etching of aluminum and gating of the exposed InAs to form the desired structures. Therefore, proximitized double nanowires could be designed in 2-DEG platforms, opening a new path for double-nanowire exploration.

Following the above directions can significantly boost the pursuit and investigation of the proposed geometries involving parallel nanowire systems.

A

FABRICATION RECIPES

This Appendix presents the main recipes used to fabricate the devices shown in this thesis, from the base chip preparation to the final steps of the fabrication process.

Fabrication notes and abbreviations:

- Ashing: 100W diener oxygen plasma ashing

- IPA: Isopropanol

- MIBK/IPA 1/3 : 1/3 solution of Methyl isobutyl ketone and Isopropanol

- Transene D: Transene Aluminum etchant type D

- NMP: N-Methyl-2-pyrrolidone

- baking: heating the sample on a hotplate

- WF: Writefield

- EBL: 100 keV electron beam lithography instrument. All EBL patterns are exposed using the BEAMER program

A.1 Base chips fabrication

Alignment marks

- Cleaving a 20x20 μm^2 piece of highly doped Si/SiO$_2$ (16 number of individual chips)

- Ultrasonic sonication at 80 KHz, 100% power for 2 minutes in acetone solution

- Rinsing in acetone, then IPA

- Blowdry with N$_2$

- Ashing for 2 minutes

- Baking for 3 minutes at 185 °C

- Spin coating PMMA EL9 resist at 4000rpm for 45 seconds

- Baking for 3 minutes at 185 °C

- Spin coating CSAR4 resist at 4000rpm for 45 seconds

- Baking for 3 minutes at 185 °C

- EBL exposure with 400 $\mu C/cm^2$ area dose, 300 μm WF, 60000 dots and 500 pA current

- Developing in 30 seconds o-xylene, 40 seconds MIBK/IPA 1/3, 30 seconds IPA

- ashing 1 minute

- Depositing 5 nm Ti and 110 nm Au using a 10 keV e-beam evaporator

- Lift-off process using NMP for 75 minutes at 80 °C

- Assisting lift-off by blowing liquid to the sample using a pipette

- Rinsing in acetone for 1 minute, then rinsing in IPA for 1 minute

- Blowdry with N$_2$

Bonding pads

- Rinsing in acetone for 1 minute, then rinsing in IPA for 1 minute

- Blowdry with N_2

- Baking for 4 minutes at 185 °C

- Spin coating LOR3B resist at 4000rpm for 45 seconds

- Baking for 4 minutes at 185 °C

- Spin coating AZ1505 resist at 4000rpm for 45 seconds

- Baking for 2 minutes at 115 °C

- UV lithography exposure

- Developing in MF321 for 35 seconds (essential to not move the chip while developing)

- submerging in MQ water for 30 seconds

- Blowdry with N_2

- Ashing for 4 minutes

- Depositing 10 nm Ti and 90 nm Au while rotating (45% power and 15 ° tilt)

- Lift-off process using NMP for 1 hour at 80 °C (Chip must face down to prevent precipitation of gold particles)

- Assisting lift-off by blowing liquid to the sample using a pipette

- Rinsing in acetone for 1 minute, then rinsing in IPA for 1 minute

- Blowdry with N_2

- Ashing 2 minutes

Wafer dicing

- Spin coating AZ4511 resist at 4000rpm for 45 seconds

- Baking for 2 minutes at 115 °C

- Dicing wafer to 16 individual chips to fabricate nanowire devices

A.2   Nanowire device fabrication

Aluminum etching

- Ashing 1 minute

- Spin coating PMMA EL9 resist at 4000rpm for 45 seconds using a low acceleration program

- Baking for 2 minutes at 185 °C

- EBL exposure with 400 $\mu C/cm^2$ area dose, 300 μm WF, 60000 dots and 500 pA current

- Developing in MIBK/IPA 1/3 for 40 seconds

- Blowdry with N_2

- Ashing 1 minute

- Baking for 1 minute at 115 °C

- Heating a beaker with Transene D and one with MQ water with the same volume. Monitoring the temperature on the MQ beaker.

- At 50 °C submerge the chip in the Transene D beaker for 8 seconds

- Terminate etching by submerging the chip in the MQ beaker for 30 seconds

- Rinse in room temperature MQ for 30 seconds

- Blowdry with N_2

- Strip-off the resist using dioxolane for 2 minutes, acetone for 2 minutes and rinse in IPA for 1 minute

- Blowdry with N_2

Contacts and gates deposition

- Ashing 1 minute

- Spin coating PMMA A6 resist at 4000rpm for 45 seconds using a low acceleration program

- Baking for 4 minutes at 185 °C

- EBL exposure with 1000 $\mu C/cm^2$ area dose, 600 μm WF, 240000 dots and 500 pA current

- Developing in MIBK/IPA 1/3 for 30 seconds

- Rinse in IPA for 30 seconds

- Blowdry with N_2

- Ashing 45 seconds

- Argon milling to remove the oxide on the nanowires and establish good ohmic contact. Using 25 W 18 mTorr for 9 minutes for contacts on aluminum and 18 W 18 mTorr for 8 minutes for contacts on InAs. The process is performed in the same metallization chamber, without breaking vacuum between the argon milling and the metal evaporation procedure. Depositing 5 nm Ti and 200-250 nm Au (depending on the nanowire diameter)

- Lift-off process using NMP for 1 hour 30 minutes at 80 °C

- Assisting lift-off by blowing liquid to the sample using a pipette

- Rinsing in acetone for 1 minute, then rinsing in IPA for 1 minute

- Blowdry with N_2

- Ashing 2 minutes

Hafnium oxide deposition

- Ashing 2 minutes

- Spin coating PMMA A2 resist at 4000rpm for 45 seconds

- Baking for 2 minutes at 115 °C

- Spin coating PMMA A2 resist at 4000rpm for 45 seconds

- Baking for 2 minutes at 115 °C

- EBL exposure with 800 $\mu C/cm^2$ area dose, 300 μm WF, 20000 dots and 2 nA current

- Developing in MIBK/IPA 1/3 for 60 seconds

- Rinse in IPA for 30 seconds

- Blowdry with N_2

- Ashing 2 minutes

- Deposing Hafnium oxide using the atomic layer deposition method. 50 cycles, 10 hours prebake at 110 degrees with 0.2 HfO_2 pulsetime and 0.5 H_2O pulsetime

- After unloading from the ALD instrument, scratch the four corners of the chip

- lift-off in NMP for 4 hours at 83 °C (keeping the sample face down)

- Assisting lift-off by blowing liquid to the sample using a pipette

- Carefully inspect the chip using dark field microscopy for possible "fences" that can damage the top-gates from passing through.

B

ADDITIONAL DATA FOR DOUBLE NANOWIRE JOSEPHSON JUNCTIONS EXPERIMENT

This Appendix includes additional data of the device shown in Chapter 5, as well as data of a second device. Some parts of this extensive analysis are not required for the in-depth understanding of the experiment, but are included to demonstrate the systematic work that was conducted.

B.1 Overview stability diagram of shells W, X and Y of Device 1

Figure B.1 presents a large-scale dI/dV colormap as a function of the two QD plunger-gate voltages. It shows the stability diagrams of the three investigated QD shells W, X, Y of Device 1 in the superconducting regime, within a single plot (stitched together). The colormap was measured at $V_{bg} = -0.21$ V. As discussed in Chapter 5, approximately vertical and horizontal parity transition lines are observed, which respectively belong to the left and right QDs. The right-QD level in shell W displays two parity lines, while the corresponding right-QD level in shells X and Y shows instead a band of enhanced conductance in place of these lines. Similarly, the left-QD level in shells W and X shows two parity lines, while shell Y shows instead a band of enhanced conduc-
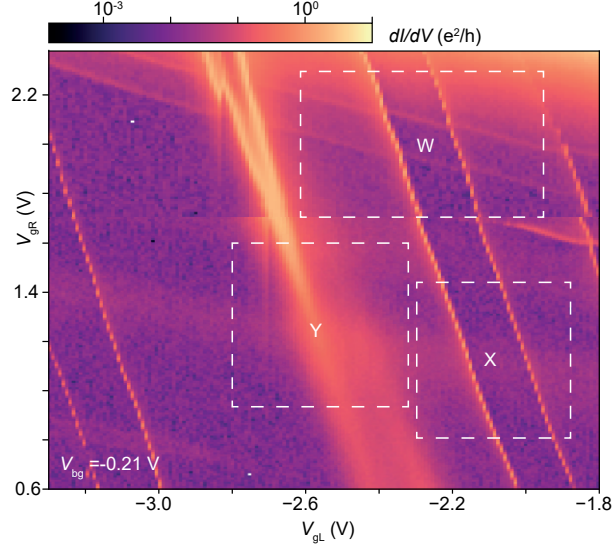
Figure B.1: Colormap of two-terminal voltage-biased zero-bias dI/dV in Device 1 vs. plunger gate voltages of the two QDs over wide gate ranges. The colormap provides an overview of the charge stability diagram in the superconducting regime. Letters are placed in the respective effective 1,1 charge sectors of QD shells W, X and Y. Dashed rectangles provide the relative gate regions explored in more detail in Chapter 5 in Figs. 5.2,5.4. The graph is a collage of two colormaps stitched together at $V_{gR} = 1.7$ V.

tance. These observations, as shown in Table 5.1, come as a result of the different $\Gamma_{L,R}$ values in the different QD shells. In turn, the band of conductance corresponding to the left QD in shell Y splits apart into two parity transition lines towards $V_{gR} = 2.2$ V, which is an indication of the dependence of V_{gR} on Γ_R.

The leakage currents generated by the side-gates did not exceed 170 pA for $V_{gL,gR} = -8$ V and for the backgate 100 pA at $V_{bg} = -5$ V. Hence, for the regimes studied our leakage currents were much lower since the voltages used were smaller.

B.2 Relation between the slope of the supercurrent branch and the switching current

In Chapter 5, we justified the use of voltage-biased zero-bias dI/dV as a gauge of the magnitude of the switching current based on the observed inverse dependence of the slope of the supercurrent branch and the switching current. Here, we show in detail our observations.

112

B.2. Relation between the slope of the supercurrent branch and the switching current
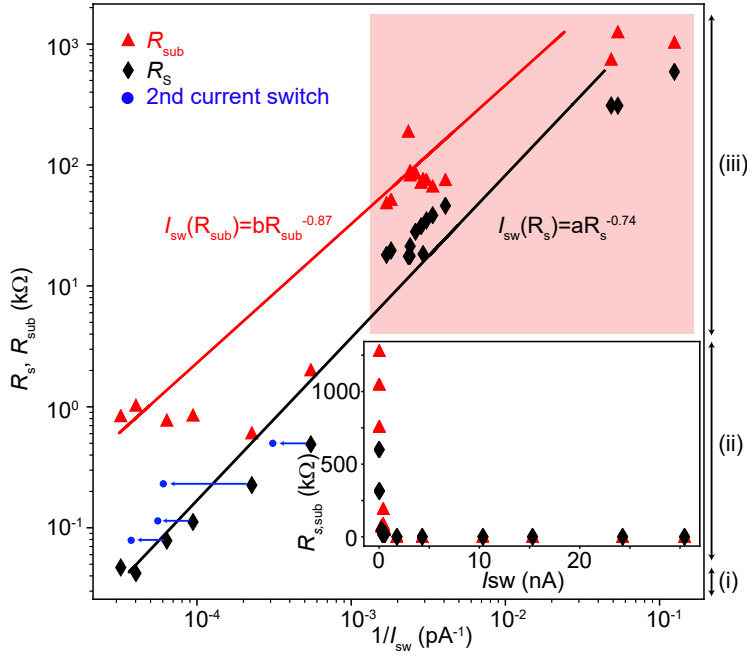
Figure B.2: Logarithmic-scale graph showing the relation of the resistance of the supercurrent branch, R_s (black diamonds), and the sub-gap resistance, R_{sub} (red triangles), to the reciprocal of the switching current, $1/I_{sw}$. Each R_s, R_{sub} and $1/I_{sw}$ data point was extracted from individual $I_{bias} - V$ curves obtained from Device 1 as in the examples shown in Fig. B.3. The two datasets, R_s and R_{sub}, are fitted to power-law functions given by the black and red lines respectively, to illustrate the trend of the datasets. Blue points correspond to the second switching which is observed for intermediate values of I_{sw}, e.g., in Figs. B.3b,c. Two-headed arrows show the range of the three regimes measured. A light-red box represents measurements in Coulomb blockade (iii). ($I_{sw} < 400$ pA). The inset shows the same datasets in linear scale.

In Fig. B.2, we investigate the inverse correlation between the resistance of the supercurrent branch, R_s, the sub-gap resistance, R_{sub}, and the switching current, I_{sw}, over more than three decades of I_{sw} in Device 1. Insets present the data in a linear scale. For reference, the datasets (red triangles and black diamonds, respectively) are fitted to power-law functions indicated in the plot (red and black curves, respectively). To obtain these two datasets, we analyzed 20 $I_{bias} - V$ curves measured in a four-terminal configuration at different gate voltages. Following Refs. [30, 31], who observed similar phenomena in ultra-small-area JJs, R_s is defined as the resistance of the supercurrent branch below a current I_{sw} at which the first switching instance to a branch of higher slope, R_{sub}, is recorded. Six examples of $I_{bias} - V$ curves covering a range

113

of $I_{sw} = 35$ nA to 7 pA are shown in Fig. B.3, with R_s, R_{sub} and I_{sw} indicated in each curve. These examples cover three typical regimes (i,ii,iii) observed and included in the data in Fig. B.2: (i) Fig. B.3a, 40 $\Omega < R_s < 50\,\Omega$; single switching with $25 < I_{sw} < 35$ nA. (ii) Figs. B.3b,c, $80\,\Omega < R_s < 600\,\Omega$, 1.8 nA$< I_{sw} < 15$ nA; large secondary switching at larger current (blue dots in Fig. B.2) with an intermediate, small slope between the first and the second switchings. (iii) Figs. B.3d-f, 20 $k\Omega < R_s < 700\,k\Omega$; single switching with 7 pA $< I_{sw} < 500$ pA. Regime (iii), shaded in red in Figs. B.2 and B.3, is relevant for the data shown in Chapter 5 as it occurs in Coulomb blockade of the two QDs.
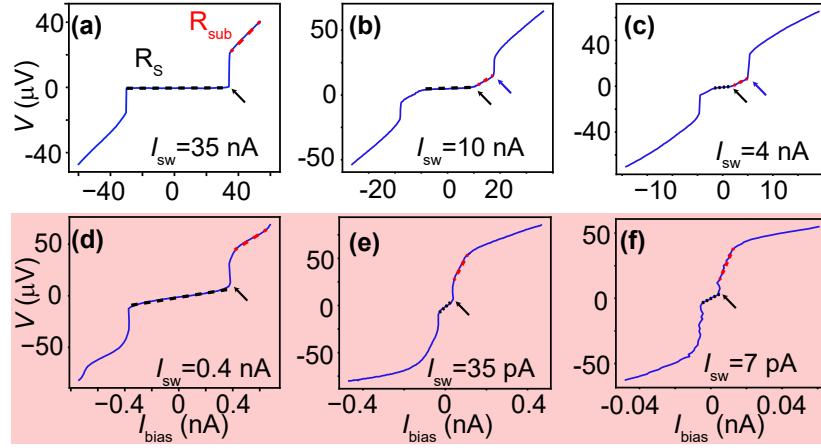
Figure B.3: Four-terminal $I_{bias} - V$ curves (in blue) at different gate voltages measured in Device 1. The data were measured using a 1 MΩ bias resistor. The switching current, I_{sw}, indicated by black arrows, decreases in each panel, ranging from (a) 35 nA to (f) 7 pA. Blue arrows in (b,c) indicate the second switching. The resistance of the supercurrent branch, R_s, is indicated by a black dashed line, while the sub-gap resistance after switching, R_{sub}, is indicated by a red dashed line. The $I_{bias} - V$ curves (d-f) inside the red box correspond to the Coulomb-blockade regime investigated in Chapter 5.

While our data is reminiscent of Refs. [30, 31], an identification of the mechanism behind our observations is outside of the scope of this article. The value of the data resides instead in the nearly monotonous inverse dependence of R_s on I_{sw} in Coulomb blockade, which justifies our interpretation of voltage-biased zero-bias dI/dV. We also note, that even though we could not perform true four-terminal measurements (device configuration of Fig. 1) for extracting the metal/hybrid nanowire contact resistance, we did make four-terminal measurements on a Josephson junction between two DQD junction devices on the same

Figure B.4: (a) Switching current I_{sw} as a function of gate voltage tuning the device through QD transitions. Red points are taken using a 2 GΩ bias resistor, and blue points using a 1 MΩ bias resistor. (b) $I_{bias} - V$ curves for three different bias resistors.

nanowire. By tuning this junction by the backgate, we observe similar range of slope from 100 Ω to the kΩ range as the switching current is diminished indicating that the slope is not related to significant contact resistance.

In Fig. B.4a we demonstrate the extracted switching current as a function of the plunger gate, tuning the device through a QD resonance. The data are measured with a 2 GΩ resistor (red line) and with a 1 MΩ resistor (blue line), as done in Chapter 5. As the figure shows, despite of the difference in the bias resistor, the switching occurs at the same current for both resistors throughout the measurement, for both small and larger values of I_{sw}, ranging from 10 pA to 400 pA.

In Fig. B.4b we show three examples of $I_{bias} - V$ curves using different bias resistors to showcase that the value of I_{sw} is independent to the choice of the bias resistor. Moreover, these measurements show the dependence of the slope of the switching to the choice of bias resistor. As the bias resistor becomes comparable to the junction resistance in Coulomb blockade (blue line) the switching acquires a negative slope. These measurements were taken from Device2 in a different gate setting to the one discussed in Section V.

B.3   Methods for the extraction of quantum-dot parameters

In this section, we present the methods which we used to measure the parameters of the QDs noted in Table 5.1. We detail our measurements through typical examples. First, we provide an example of the method

used to extract the charging energies of the side QDs, U_L and U_R. Figure B.5a shows a two-terminal voltage-biased Coulomb-diamond spectroscopy of the left QD in shell X (Device 1) taken in the superconducting state. We use white dashed lines to prolong straight features in the edges of the central diamond. The bias difference between the upper apex of the diamond and the edge of the superconducting gap, Δ, is a direct measurement of U_L. In this way, we obtain $U_L = 3.7 \pm 0.5$ meV, where the error bars come from the broadening of the edges of the diamond. From the ratio of the bias value of the apex of the diamond to the gate difference between its two zero-bias crossings, we find the lever-arm parameter of the left-QD plunger gate, $\alpha_L = 0.019 \pm 0.002$. The same method was used for obtaining lever-arm parameters of the two QDs in all shells.

We obtain the size of the superconducting gap, Δ, from voltage-biased spectroscopy centered on a bias window around the gap. Figure B.5b shows an example of such measurement in shell W. Two pairs of bias-symmetric horizontal dI/dV lines identified by white dashed lines are observed: 1) Outer pair, which correspond to the co-tunnelling lines due to quasiparticle transport from -2Δ in lead 1 to 2Δ in lead 2 (4Δ spacing), and 2) Inner pair, which correspond to the first multiple Andreev reflection line at $\pm\Delta$. From the bias position of the lines, we find $\Delta = 0.19 \pm 0.01$.

In order to estimate the total tunnelling rates between the left and right QDs and the superconducting leads, $\Gamma_{L,R}$, as well as the individual tunnelling rates of each QD to each lead (1 and 2), $\Gamma_{L1,L2}$ and $\Gamma_{R1,R2}$, we fit the even-charge side of Coulomb peaks of each dot (when applicable) in the normal state, where Kondo correlations are suppressed. An instance of this fit for the case of the left QD in shell X is shown in Fig. B.5c, which corresponds to a two-terminal voltage-biased zero-bias dI/dV measurement along the same plunger gate voltage as in Fig. B.5a. The measurement is done at $B = 2$ T to drive the device into the normal state. Red lines are fits of the data (black points) to the Lorentzian

$$\frac{dI}{dV} = \frac{e^2}{h} \frac{4\Gamma_1\Gamma_2}{\Gamma^2} \frac{(\Gamma^*/2)^2}{(\epsilon - \epsilon_0)^2 + (\Gamma^*/2)^2} \tag{B.1}$$

which is applicable in view of our system parameters ($k_b T \ll \Gamma$ and
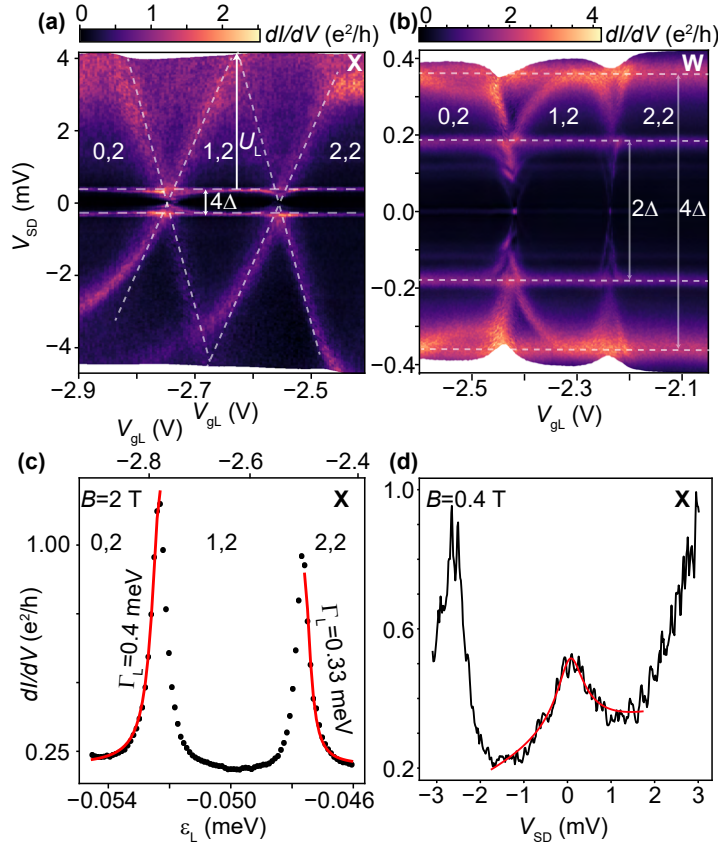
Figure B.5: (a-d) Examples of two-terminal, voltage-biased measurements used to extract QD parameters. (a) Colormap of the differential conductance, dI/dV, as a function of the bias voltage, V_{SD}, and of the plunger gate voltage of the left QD, V_{gL}, representing Coulomb-diamond spectroscopy of shell X in Device 1 in the superconducting state. The left, right QD charge states with respect to shell X are indicated in each diamond. Dashed lines correspond to an intermediate diamond drawn between the largest and the smallest of the diamonds which can fit well to the data. The resulting diamond is used to obtain the charging energy and the lever-arm parameter of the gate to the applied bias. (b) Colormap of dI/dV as a function of V_{SD} and V_{gL} measured in shell W in Device 1 in the superconducting state, showing a zoomed-in bias spectroscopy to determine the superconducting gap, Δ. The left, right QD charge states with respect to shell W are indicated. (c) Linear conductance at $B = 2$ T in the normal state (black dots) showing two Coulomb peaks whose left-QD even-charge sides are fitted to Eq. B.1 (red curve) to extract the total tunnelling rate and the individual tunnelling rates of the left QD to the leads. (d) dI/dV vs. V_{SD} linecut obtained from Fig. 2h, showing a Kondo resonance at $B = 0.4$ T in the normal state (black curve) fitted to Eq. B.2 (red curve).

$\Gamma < U$) [33, 172]. Here, $\Gamma^* = 1.36\Gamma$, ϵ is the level position of the QD, ϵ_0 is the position of the Coulomb peak, and $\Gamma = \Gamma_1 + \Gamma_2$. To convert from plunger gate voltages to ϵ of the QDs, we use the lever-arm parameter

of the corresponding gates obtained as detailed above. We proceed in this way to convert from V_{gL} to ϵ_L in Fig. B.5c, before performing the fit. Through error propagation of this conversion, and using the standard deviation of the fit, we obtain error bars for $\Gamma_{L,R}$ as reported in Table 5.1.

Next, we describe our method for extracting a rough estimate of the Kondo temperature, T_K. We fit Kondo resonances in the data with the device driven to the normal state by a $B = 0.4$ T field. The fit function utilized is the widely used Frota function [173]

$$\frac{dI}{dV} = a\text{Re}\left[\sqrt{\frac{i\Gamma_K}{V - \epsilon_k + i\Gamma_K}}\right] + bV + c \tag{B.2}$$

where $\Gamma_K = 1.6k_B T_K$ and ϵ_k is the position of the Kondo resonance. The original Frota function [173] is supplemented here by a term linear in V and a shift constant c to account for bias asymmetries and a background in conductance, respectively [174]. These appear in our case due to a bias-asymmetric triplet excited state which is broader at positive bias and interferes with the conductance from the Kondo resonance. To account for the finite B applied, we report T_K with and without subtracting the Zeeman energy $E_Z = g\mu_B B$. Figure B.5d shows an example of a measurement (in black) of dI/dV vs. bias voltage, V_{SD}, taken from Fig. 2h in the normal state at $B = 0.4$ T. This measurement displays the asymmetric Kondo resonance discussed above and it is fitted with Eq. B.2 (red curve). The fit is bounded by the tails of the excited triplet state at positive and negative V_{SD}. See Table 5.1 for extracted values.

In Fig. 2e, we had indicated with white dashed lines the positions of the parity lines in the stability diagram of shell X in Device 1 at $B = 2$ T in the normal state. In Fig. B.6a, we show the raw data used to extract those positions.

In Fig. B.6b, we show data of a larger magnetic field scan of Fig. 2h up to $B = 6$ T. The peak at $V_{SD} = 3$ mV at $B = 0$ T which we identify as a triplet state of the left QD anti-crosses (possibly with a singlet state of the same QD) at $B \approx 5$ T. It exhibits an energy avoidance of 0.32 mev with respect to zero-bias. The bias-symmetric counterpart of this peak shows the same anti-crossing.

Figure B.6: (a) Colormap of two-terminal, voltage-biased zero-bias differential conductance dI/dV, in the normal state of shell X in Device 1, measured at a magnetic field $B = 2$ T, and used to extract the Coulomb lines indicated by white dashed lines in Fig. 2e.(b) Colormap of dI/dV vs. bias voltage, V_{SD}, corresponding to the measurement in Fig. 2h stitched to a follow-up colormap at larger B field. Arrows point to an avoided crossing appearing in the large-B data.

B.4 Voltage-biased stability diagram, field measurements and Γ asymmetry in shell Y

In this section, we present additional measurements of shell Y.

To add additional support to our use of two-terminal, voltage-biased dI/dV data as a gauge of four-terminal I_{sw} data, we show in Fig. B.7a a two-terminal, voltage biased dI/dV colormap of shell Y in the superconducting state, taken at $V_{bg} = 0.3$ V; i.e., under the same experimental conditions as those used to obtain the I_{sw} data in Fig. 4a. The two colormaps are strongly alike, supporting our assertion that lines observed in dI/dV data are faithful parity lines of the QDs due to the finite resistance of the supercurrent branch in the Coulomb blockade regime, as shown in Appendix B.2. Figure B.7b shows the same charge stability diagram measured at $B = 2$ T, which corresponds to the dashed blue lines of Fig. 4a.

Through the measurements in Figs. B.7c-f, which have a similar character as those in Figs. 2f-i for shell X, we show that, in the limit of the resolution of the experiment, the inter-dot tunnel coupling t_d is negligible. Furthermore, the Zeeman splitting clearly observed at large fields for odd fillings in panels c, e and f establishes that the double quantum shell consists of two spin-degenerate levels.

Next, we describe in more detail the effect which V_{gR} has on the tunnelling rates between the left QD and the two superconducting

119

B. ADDITIONAL DATA FOR DOUBLE NANOWIRE JOSEPHSON JUNCTIONS EXPERIMENT
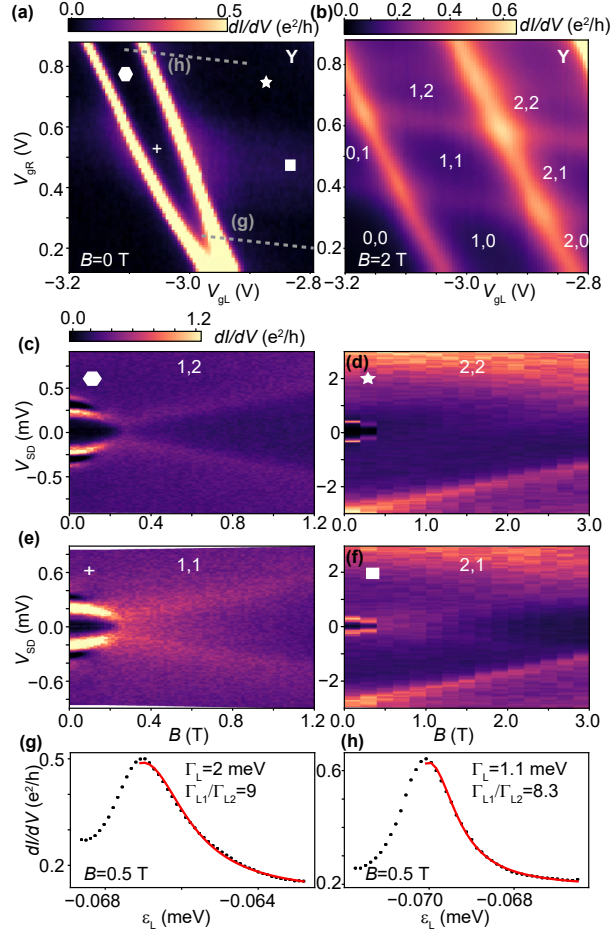
Figure B.7: (a) Colormap of two-terminal, voltage-biased zero-bias differential conductance dI/dV in the superconducting state of shell Y. Dashed rectangles enclose the nine charge states of the two shells. (b) Colormap of shell Y measured in the normal state at magnetic field $B = 2$ T, which is used to extract the Coulomb lines indicated by black dashed lines in Fig. 4a. (c-f) Colormaps of dI/dV vs. B and source-drain bias voltage, V_{SD}, taken in four different charge sectors indicated by symbols in (a). (g,h) Linear conductance at $B = 0.5$ T in the normal state in shell Y (black dots) taken with the plunger gate voltages swept through the grey dashed lines in (a), representing Coulomb peaks associated with the left-QD level at two different level positions with different tunnelling rates to the leads within the *same* level due to tunnelling-rate dependence on V_{gR}. Red curves are fits to Eq. B.1 of the data in the even-charge side of the rightmost Coulomb peaks, which we use to extract the total tunnelling rate to the leads, Γ_L, and the lead 1,2 tunnelling rate asymmetry, Γ_{L1}/Γ_{L2}, indicated in each plot.

leads, $\Gamma_{L1,L2}$. In Figs. B.7g,h, we show traces of linear conductance at $B = 0.5$ T in the normal state (black dots) measured with the plunger gates swept through the grey dashed lines indicated in Fig. B.7a. These grey dashed lines go through the top and the bottom parts of the right-

120

most Coulomb peak of shell Y (leftmost dashed rectangle) in the colormap of Fig. B.7a, which exhibits a V_{gR}-dependent spacing with the leftmost Coulomb peak. This is a signature of different total Γ_L among the upper and lower portions of the colormaps. We use Eq. B.1 to fit the even-charge portion of these peaks, as done above, and provide values of Γ_L and tunnelling rate asymmetry extracted from the fit in Figs. B.7g,h. We find that Γ_L is smaller in Fig. B.7h than in Fig. B.7g; i.e., it is smaller in the upper segment of the colormap in Fig. B.7a than in the bottom one, in agreement with our reasoning above. Moreover, the coupling asymmetry is also decreased in the upper segment, which explains the lower I_{sw} at lower V_{gR} in Fig. 4b,c, despite Γ_L being larger.

B.5 Additional data for shell W
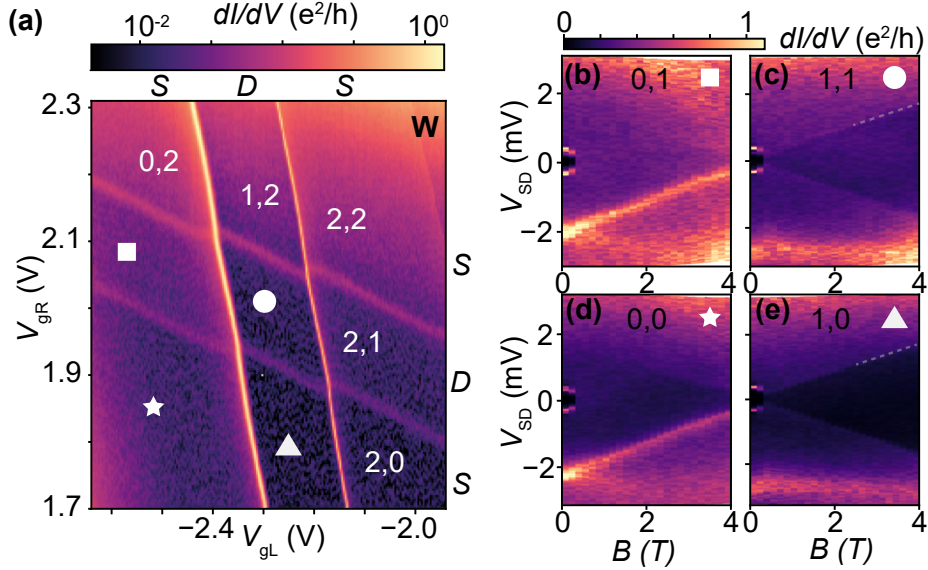
Figure B.8: (a) Colormap of two-terminal, voltage-biased zero-bias differential conductance dI/dV in the superconducting state of shell W. (b-e) Colormaps of dI/dV vs. magnetic field, B, and source-drain bias voltage, V_{sd}, taken in four different charge sectors indicated by symbols in (a). Dashed lines are added as a guide to the eye.

Figure B.8a shows the charge stability diagram measured at zero source-drain bias for shell W. On the charge sectors (0,0), (0,1), (1,0) and (1,1) noted by the four symbols measurements of V_{sd} vs. B are shown in Fig. B.8b-e. The co-tunnelling lines of QD_R are not visible in Fig. B.8b due to the fact that the parity lines have very faint conductance, as

seen in the charge stability diagram, causing the conductance of the co-tunnelling lines to be below the noise level. In the case where both QDs have no electrons on their highest unoccupied energy level, there are no signatures of co-tunnelling lines spitting, as seen in Fig. B.8d. For the case where the left QD has odd number of electrons, co-tunnelling lines are present shown in Figs. B.8c,e.

B.6 Device 2
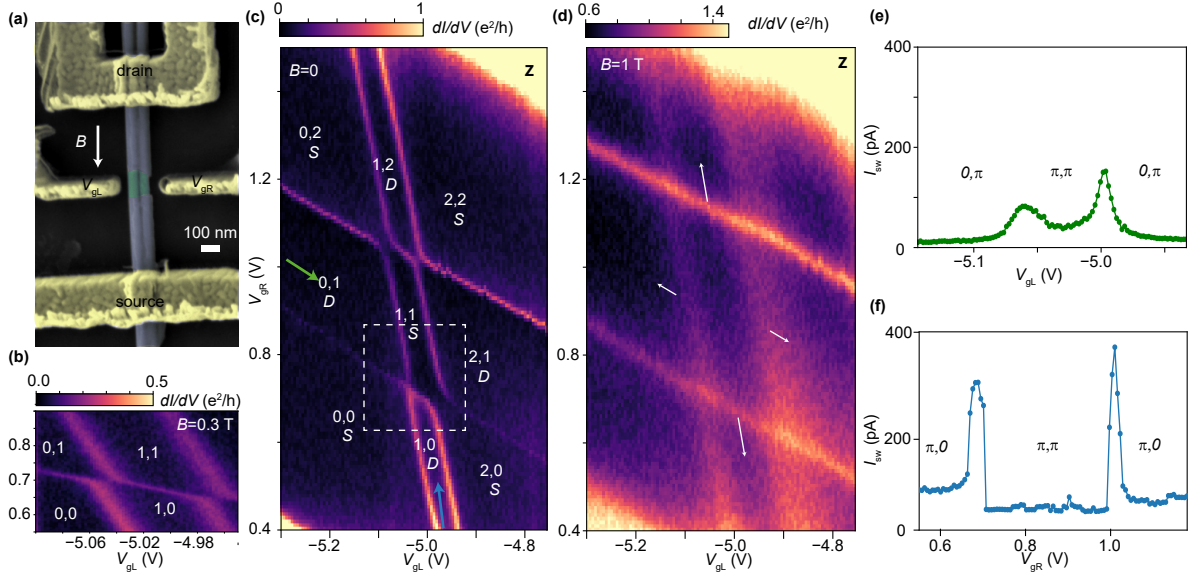
Figure B.9: (a) False-colored scanning electron micrograph of Device 2. The device has the same architecture as Device 1, and was fabricated in the same chip. (b,c,d) Colormaps of two-terminal, voltage-biased, zero-bias differential conductance, dI/dV, vs. plunger gate voltages of the two QDs. Data taken in a shell identified as Z in (c) the superconducting state, $B = 0$, and (d) the normal state, $B = 1$ T. Panel (b) corresponds to the gate region inside of the dashed rectangle in (c), showing the evolution of the triple points at the one-electron 1,0-0,1 and at the two-electron 1,1-2,0 charge transitions. (e,f) Four-terminal measurements of I_{sw} along gate trajectories collinear to the green (e) and blue (f) arrows in (c). For simplicity, only (e) V_{gL} and (f) V_{gR} values are indicated on the x-axes

We here show transport data from an additional double-nanowire parallel-QD JJ device. The device was fabricated on the same chip as the previous device, it has a similar architecture, and it was similarly tuned into a nearly-depleted Coulomb-blockaded regime. In Fig. B.9a

Table B.1: Parameters for shell Z of Device 2. Extraction methods are presented in detail in Sec. B.3. The meaning of indexes a and d is given in the caption of Table 5.1 in Chapter 5.

Shell	U_L (meV)	U_R (meV)	Γ_L (meV)	Γ_R (meV)	$\frac{\Gamma_L}{U_L}$	$\frac{\Gamma_R}{U_R}$	$k_B T_{K_L}$ (meV)	$k_B T_{K_R}$ (meV)	$\frac{k_B T_{K_L}}{0.3\Delta}$	$\frac{k_B T_{K_R}}{0.3\Delta}$
Z	0.8 ± 0.1	2.6 ± 0.4	0.29 ± 0.02^a	0.19 ± 0.01^a	0.39 ± 0.06	0.07 ± 0.01	0.03 ± 0.01^d	$(8.1 \pm 0.3) \cdot 10^{-5d}$	0.53	0.02

we present a false-colored SEM image of Device 2. The device has an identical geometry as Device 1.

In this device, as in the previous one, the supercurrent branch in four-terminal $I_{\text{bias}} - V$ measurements displays a finite slope, R_S, which is significant in Coulomb blockade, and which is also proportional to $1/I_{\text{sw}}$. Therefore, we also use here two-terminal, voltage-biased, zero-bias $dI/dV = 1/R_S \sim I_{\text{sw}}$ measurements to trace the GS parity stability diagram of the side QDs near depletion, as we did in Figs. 2a,e. Figure B.9c shows such a measurement in a selected shell of this device, denoted as Z (for shell parameters, see Table B.1). We assign effective charge numbers to the left and right QDs based on the smaller size of the central charge hexagon, 1,1, compared to the eight outer ones. The spins of the QDs are now forming an exchange singlet GS, as hinted by the curvature of the parity lines near the triple points. The absence of states crossing zero energy along the detuning line of 2,0-1,1-0,2 charge sectors verifies this claim. Figure B.9d shows a measurement of the charge stability diagram at $B = 1$ T, in the normal state. Here, the 1,1 charge sector grows in vertical and horizontal direction, and the curvature near the triple points is vanished. We argue that broadening of states due to absence of superconductivity is the reason why the interdot coupling signatures are obscured. The enlargement of the 1,1 sector can be explained as a singlet to triplet ground state transition occurs with the presence of a finite magnetic field, effectively enlarging the charge sector.

As Yu-Shiba-Rusinov physics are relevant in this charge sector, based on the strong coupling of QD_L to the superconducting contacts (see Table 5.1), we cannot estimate the inter-dot coupling from the charge stability diagram in the superconducting state. Figure B.9b shows a measurement at $B = 0.3$ T where the superconducting effects are dampened. Hence, we can use the 1,0-2,1 anti-cross, to estimate inter-dot charging U_d and inter-dot tunneling t_d, extracting an upper

limit of $t_d \approx 50 \ \mu eV$.

For completeness, in Figs. B.9e,f, we show four-terminal measurements of I_{sw} taken with the gates swept along the green (e) and blue (f) arrows in Figs. B.9c. In this device, we do not attempt to analyze possible supercurrent interference, because QD_L is near a GS transition. The related small energy difference between the doublet GS and singlet excited state when the dot has odd number of electrons (1,0 and 1,2 charge states) complicates the analysis compared to the Device 1.

C

ADDITIONAL DATA FOR DOUBLE NANOWIRE SUPERCONDUCTING ISLAND DEVICES

This Appendix presents raw data from which figures are created in Chapter 6 as well as additional data from a second device.

C.1 Coulomb blockade structure

Figure. C.1 shows high bias measurements for device A revealing Coulomb blockade structure for different setup configurations. The charging energy is found $E_c \approx 0.5$ meV for setups $I - V$. Setup VI reveals characteristic dips of conductance owing to the Fano effect [142, 143]. Different slopes of the Coulomb diamonds are owed to the different capacitances to the various leads.

C.2 Additional data on bias spectroscopy and temperature dependence

In this section we include the zero-bias traces for each setup measured in the superconducting and normal state (B= 0.4 T), bias spectroscopy maps (Fig. C.2) magnetic field dependence measurements (Fig. C.3) as
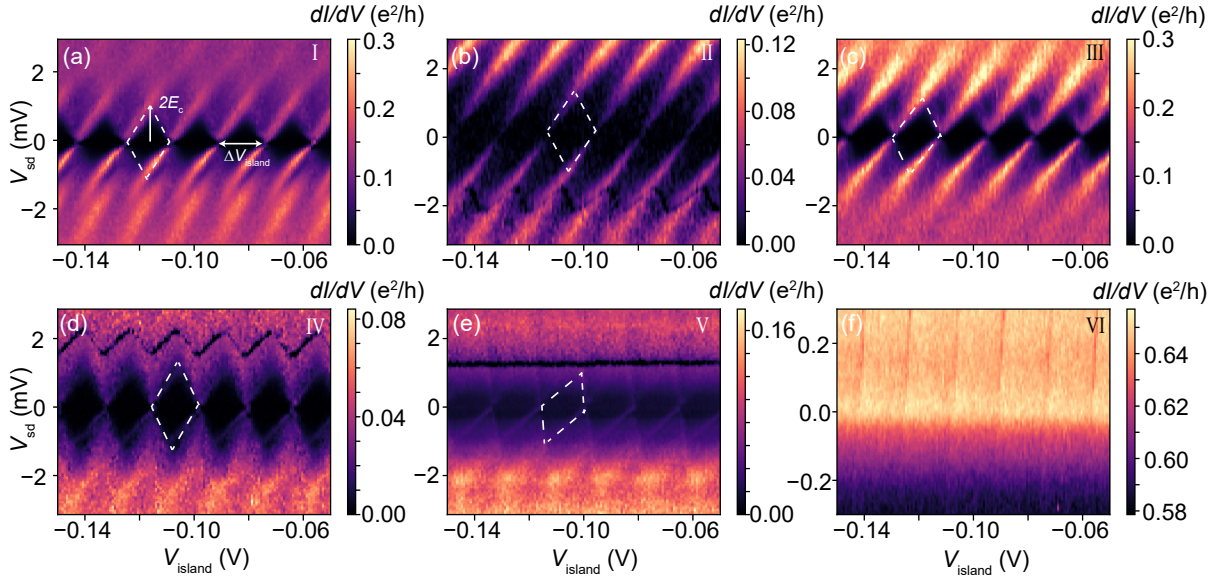
Figure C.1: Bias spectroscopy measurements for the six different setups. (a-e) Coulomb structure is observed in five setups yielding a charging energy $E_c \approx 0.5$ meV. Dashed lines are a guide to the eye for the Coulomb diamonds. (f) No Coulomb structure observed, owing to the Fano effect. These measurements are taken in gate tuning α.

well as the temperature dependence measurements (Fig. C.4) for all six setups of Device A.

Figure C.2: (a-f) Zero-bias conductance traces as a function of gate for each two-terminal combination. (g-l) Zero-bias conductance traces measured in the normal (state B= 0.4 T) for each two-terminal combination. The peaks are misaligned across different setups due to gate switches that occur when sweeping the magnetic field. (m-r) Bias spectroscopy for each setup. Measurements taken in gate tuning α.
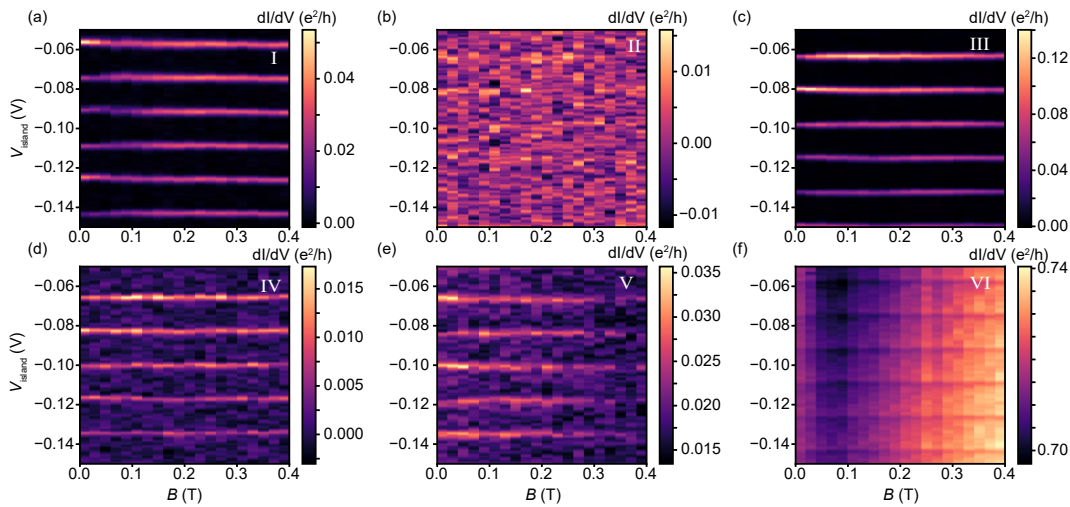
Figure C.3: (a-f) Zero bias magnetic field dependence of the superconducting island (SI) resonances. Measurements taken in gate tuning α.

C. Additional data for double nanowire superconducting island devices
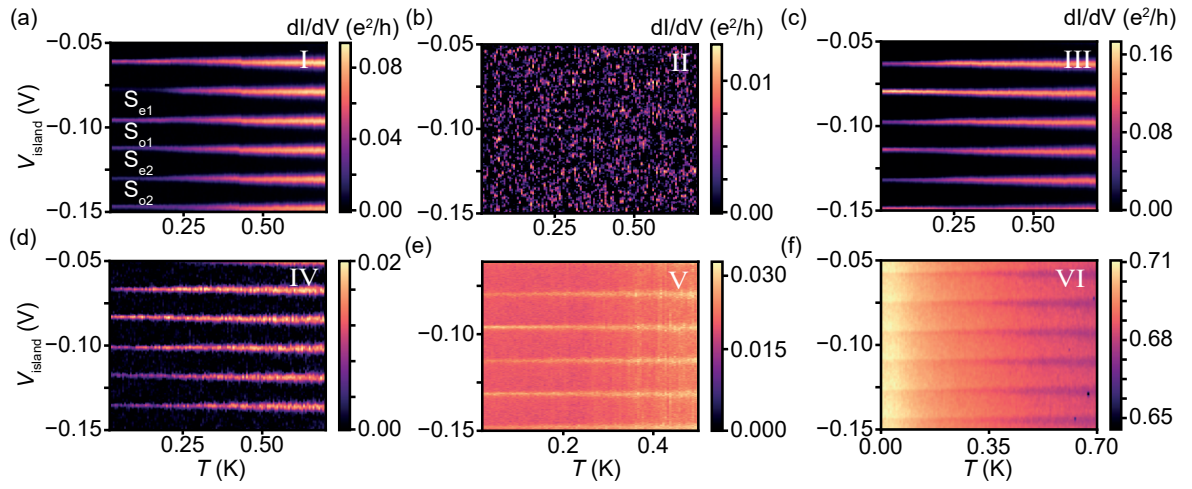
Figure C.4: (a-f) Zero bias temperature dependence of the superconducting island (SI) resonances. Measurements taken in gate tuning α.

C.3 Thermal model for superconducting island resonances

The fitting of Fig. 6.4(c,d) (solid lines) is done by using eq. C.1

$$F_o - F_e \approx -k_B T \ln \tanh \left[2\rho_{Al} V_{Al} \Delta K_1 \left(\frac{\Delta}{k_B T} \right) + \ln \coth \left(\frac{E_0}{2k_B T} \right) \right] \tag{C.1}$$

where $\rho_{Al} = 23$ eV^{-1} nm^{-3} is the electron density of states of aluminum [37–39], $V_{Al} = 91.8 \cdot 10^4$ nm^3 is the volume of the aluminum island, $K_1(x)$ is the Bessel function of the second kind, Δ is the superconducting gap of the island and E_0 is the lowest energy bound state originating by the proximity of InAs-Al. Using the above formula, we can extract a precise estimate of the energy of the bound state at different gate configurations, as shown in Fig. 6.4(c,d).

Figure. C.5 shows spacing differences $S_e - S_o$ as a function of T for finite magnetic field. Solid lines are fits using eq. C.1. For higher B the spacing diminishes, showing that the energy of the bound state has decreased due to the Zeeman effect. The raw data from where the spacings are extracted are shown in Fig. C.6.

Figure. C.7 shows three different spacing differences extracted from Fig. C.4a showing that across several charge states the change in the peaks is negligible, hinting that the SI parameters (Δ, E_0) are not modified. The discrepancy at temperatures lower than 150 mK is owed to state broadening [13] which is not included in the fits.
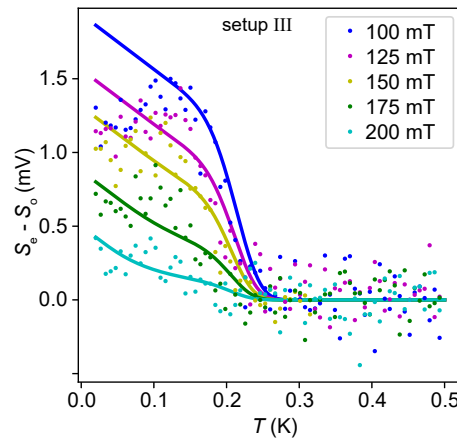
Figure C.5: Difference of even-odd sectors as a function of temperature for setup III at different magnetic field values.
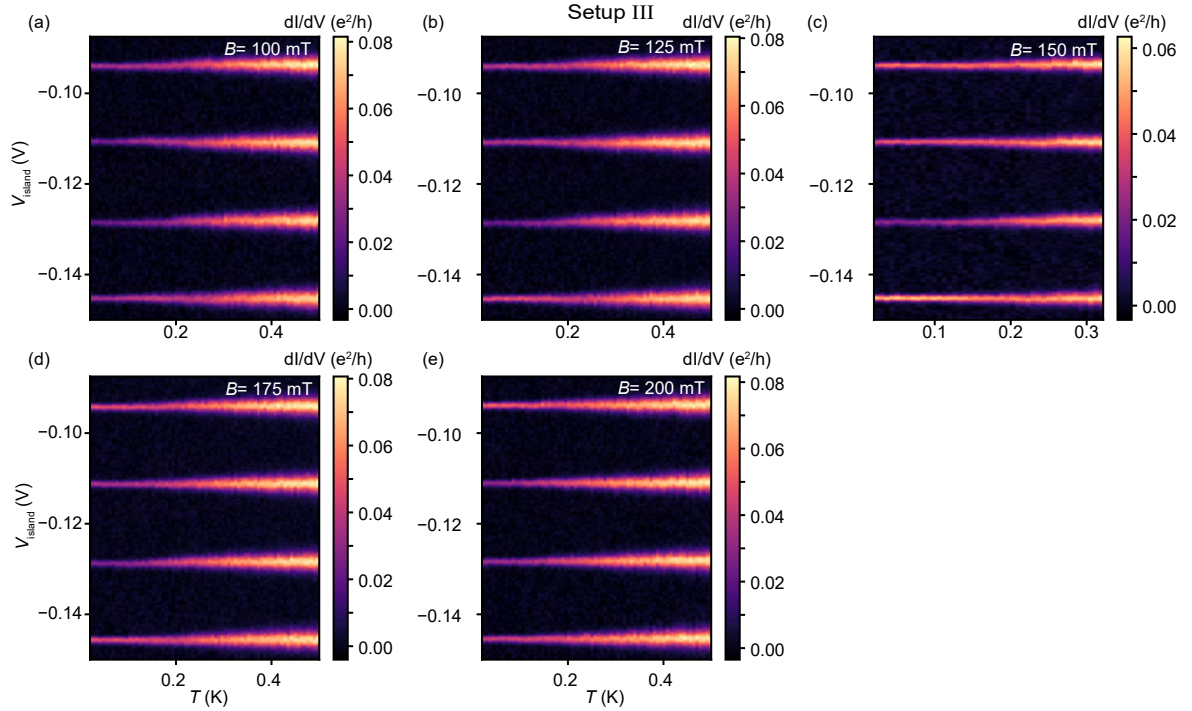
Figure C.6: Temperature dependence of the SI resonances at different magnetic field values. Data taken in setup III.
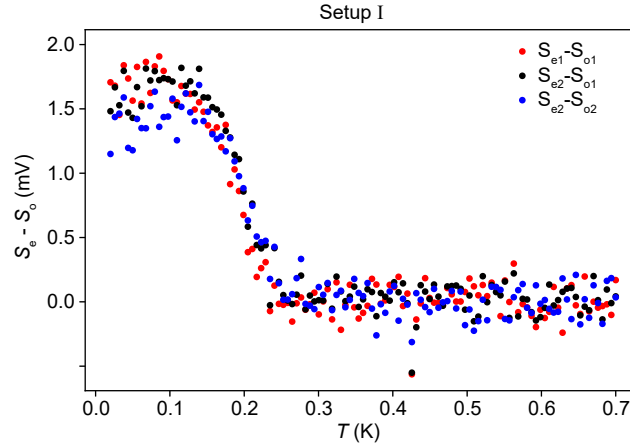
Figure C.7: Comparison of different even odd spacing differences. Legend corresponds to the S_e, S_o of Fig. C.4a. Data taken in setup I.

C.4 Zero-bias gate maps
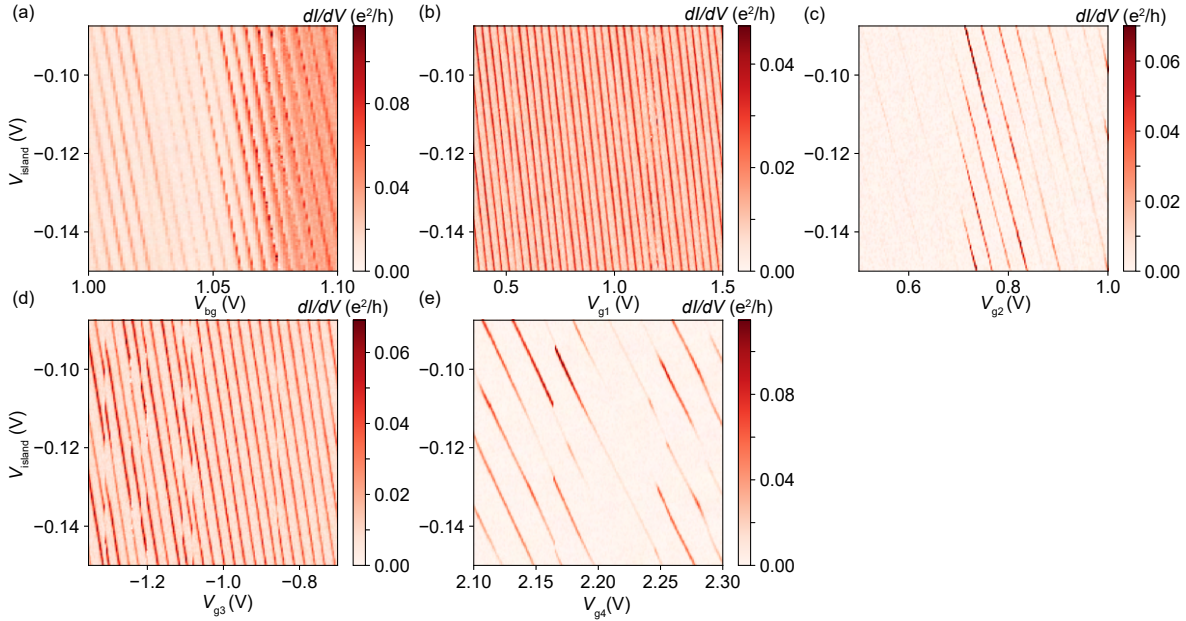
Figure C.8: Zero-bias maps of V_{island} as a function of every other gate of device A. No obvious signs of quantum dots are observed, apart from the regular resonances of the superconducting island across all gate combinations.

Figure C.8 shows zero-bias conductance maps of the plunger gate tuning the SI versus each other gate of the device. All gate maps reveal regular resonances that belong to the superconducting island. In Figure. C.8e shifts in the amplitude of the resonances are caused by an unknown effect. Hence, no obvious signs of quantum dot formation in the nanowires are observed.

C.5 Additional data for Device B

Figure C.9 shows zero-bias traces for each setup combination measured in the superconducting (Fig. C.9(a-f)) and in the normal state (Fig. C.9(g-l)). It is evident that only in setups I, IV, VI SI resonances are observed in the superconducting state. The absence of the resonances in the other setup combinations is owed to the weak coupling between the corresponding probed leads and the SI. When superconductivity breaks down at a high enough magnetic field, these resonances are recovered as seen in Fig. C.9(h,i). The interwire co-tunneling is found lower than in Device A, as the background conductance in setups V, VI is lower than the corresponding ones of Device A. The peaks are misaligned

131

unlike Device A because these measurements were not taken directly one after another, as gate-switches cause small changes in the voltages where the resonances are measured. The magnetic field data were the above measurements were taken from are shown in Fig. C.10. Figure C.11 shows the method used to estimate E_c and E_0 for device B.

In a different gate configuration, Fig. C.12 shows zero-bias traces as well as bias spectroscopy measurements for the six two-terminal combination setups for Device B. The signal is strongly suppressed inside the superconducting gap on most setups. However, Coulomb resonances are observed on all combinations confirming that the same SI is probed by all terminals.
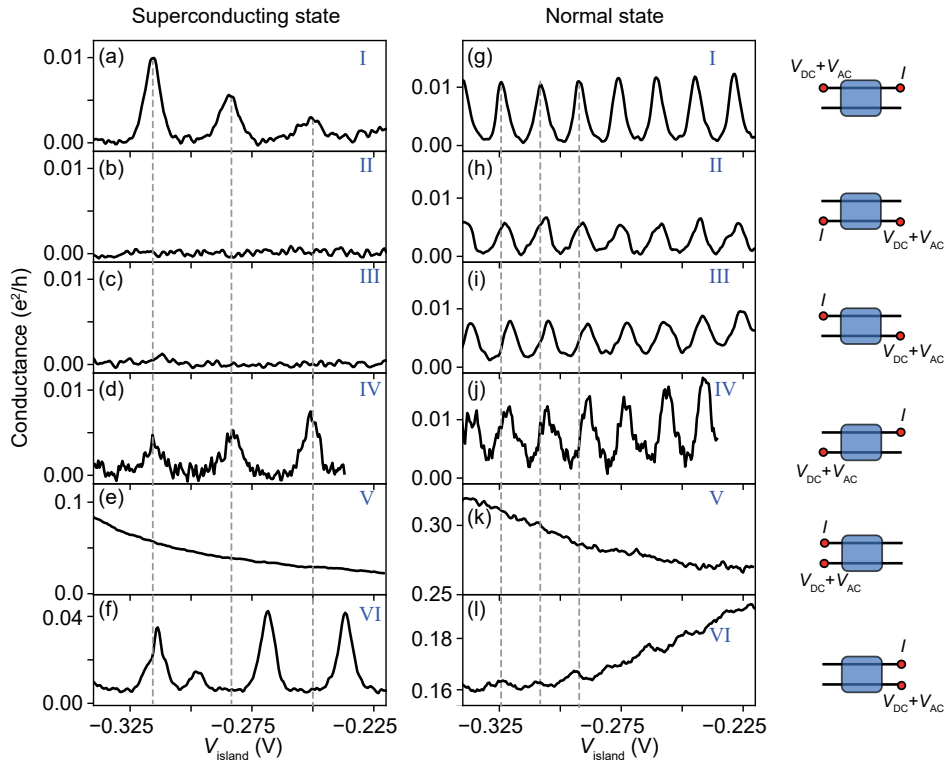
Figure C.9: Zero-bias conductance traces as a function of V_{island} for each two-terminal combination for Device B at the superconducting state ($B= 0$ T) and at the normal state ($B= 0.5$ T). Panel (l) is generated by averaging the signal for measurements from $B= 0.3$ T to $B= 0.35$ T.
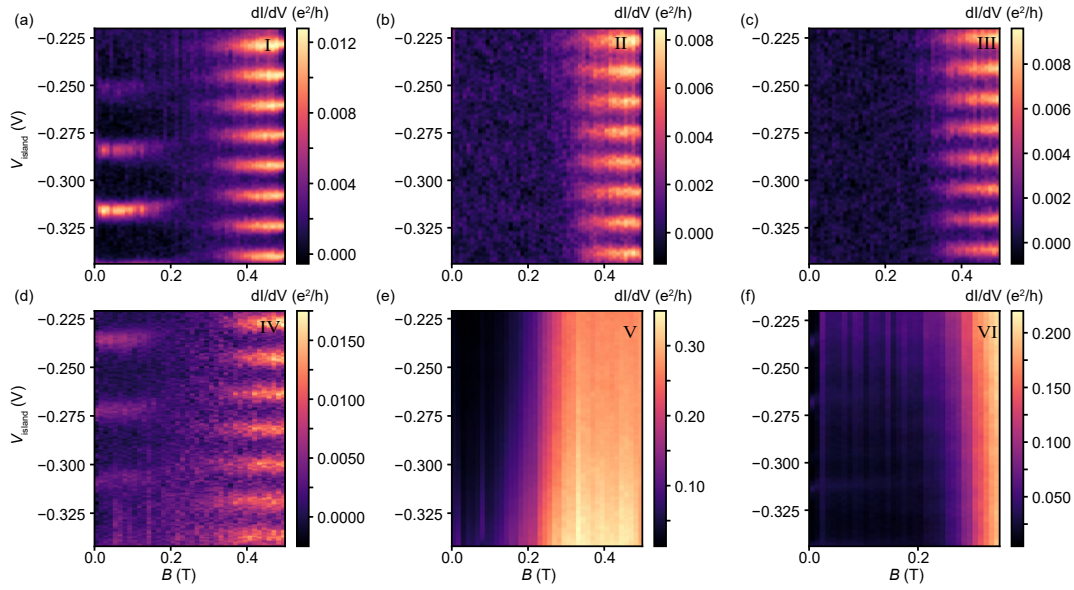
Figure C.10: (a-f) Zero bias magnetic field dependence of the superconducting island (SI) resonances in Device B. Data shown in Fig. C.9 are generated by these panels.
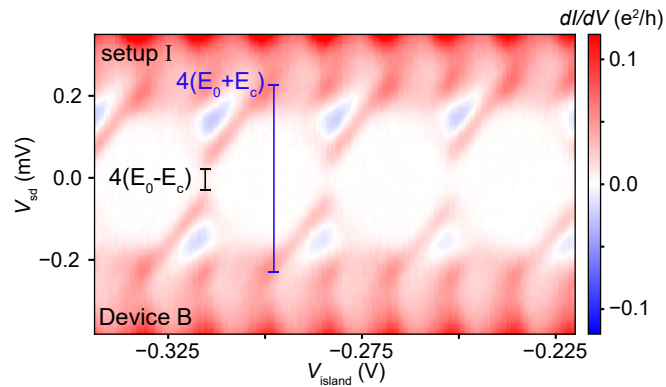
Figure C.11: Bias spectroscopy measurement of the SI in device B. As the SI is tuned at the $E_c < E_0$ regime, conductance in the proximity of zero-bias is suppressed (only valid for weakly coupled SI) and $4(E_0 - E_c)$ can be extracted from the black line. The distance between the tips of the diamonds (blue line) is $4(E_c + E_0)$. Therefore, the two values are estimated $E_c \approx 55\ \mu\text{eV}$ and $E_0 \approx 65\ \mu\text{eV}$.
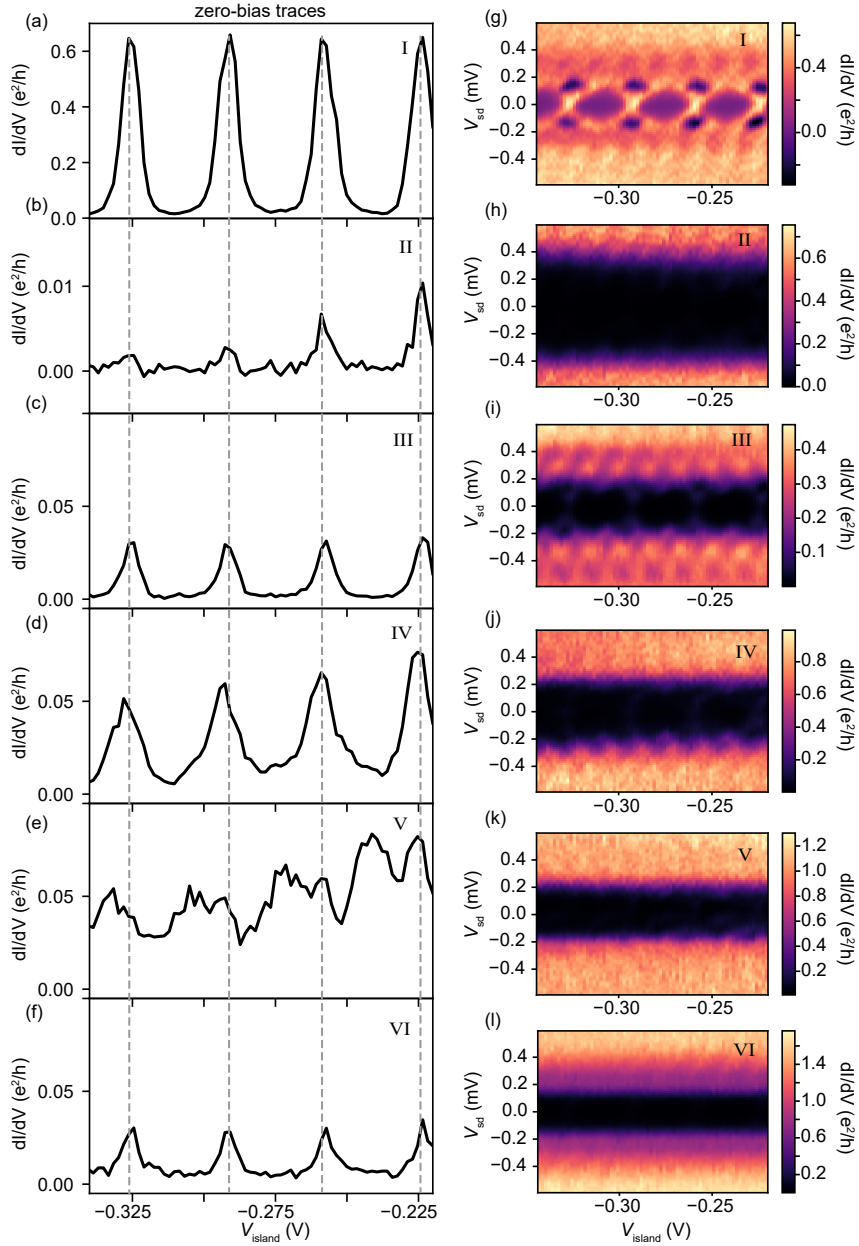
Figure C.12: Zero-bias traces for each two-terminal combination (a-f) with the corresponding bias spectroscopy measurements (g-l). The zero bias signal is strongly suppressed on all combinations but setup I. Above the superconducting gap higher conductance is recovered. Measurements are taken in a different gate configuration compared to the data shown in Chapter 6.

D

ADDITIONAL LITTLE-PARKS DATA

D.1 Little-Parks oscillations in 5 devices
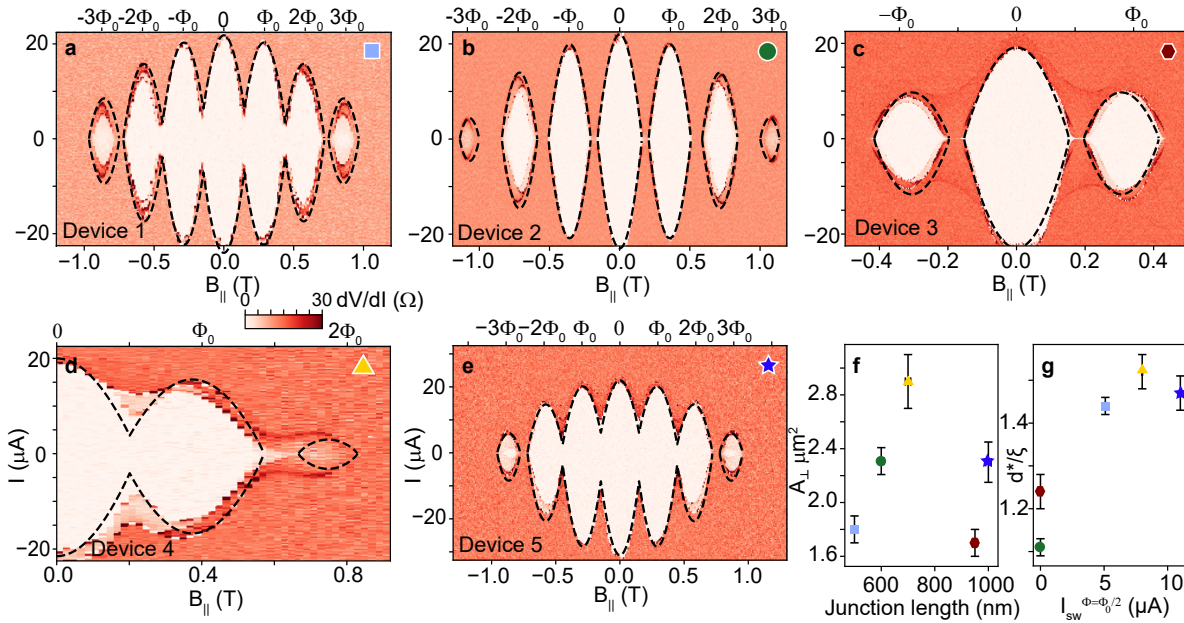
Figure D.1: Little-Parks oscillations in five different nanowire devices.(a,e) Differential resistance dV/dI measurements as a function of magnetic field B and applied current I for five different devices fabricated using five different double nanowires from the same growth batch. Dashed lines correspond to the fitted model. Panels b,c are the devices shown in Chapter 7. (f) $A_\perp$ as a function of junction length of each device shown in panels (a-e). (g) d^*/ξ ratio as a function of I_{sw} at $\Phi = \Phi_0/2$.

D. ADDITIONAL LITTLE-PARKS DATA

Table D.1: Model parameters used to fit data all devices in Fig. D.1. From left to right, coherence length (ξ), effective perpendicular flux parameter ($A_\perp$), effective parallel flux area ($A_\parallel$), and ratio of shell thickness (t_s) to effective single cylinder diameter (d^*).

Device	ξ (nm)	$A_\perp$ (nm^2)	$A_\parallel$ (nm^2)	t_s/d^*
1	66 $\pm$2	18000 $\pm$1000	7100 $\pm$50	0.13 $\pm$0.05
2	81 $\pm$2	23080 $\pm$1000	5718 $\pm$30	0.1 $\pm$0.05
3	78 $\pm$2	17000 $\pm$700	6163 $\pm$30	0.12 $\pm$0.05
4	59 $\pm$1	29000 $\pm$2000	5187 $\pm$40	0.12 $\pm$0.05
5	65 $\pm$2	23000 $\pm$1000	7000 $\pm$50	0.12 $\pm$0.05

Figure D.1a-e shows data and fit of Little-Parks oscillations in five different devices. Parameters used for the fit can be found in Table D.1 as well as their corresponding errors. The error bars are rough estimates changing only one parameter at a time, while keeping the other three fixed. All devices are fitted with the Little-Parks model with good agreement. Figures D.1a,b correspond to Device 1 and 2 analyzed in Chapter 7. To obtain a good fit, the parameter $A_\perp$ is chosen as a fitting parameter. In order to get an insight of the origin of $A_\perp$, we investigate this parameter versus junction length for the five devices shown in Fig. D.1f. However, no correlation between the two parameters is found as expected [163]. Figure D.1g presents the correlation between the d^*/ξ ratio and the switching current at the first half-integer flux quantum $I_{sw}^{\Phi=\Phi_0/2}$. Here, d^* is the diameter of a cylinder with the same area as the two hexagonal nanowires (effective diameter) and ξ the coherence length extracted from the fits. It is observed that devices with small ratio exhibit destructive Little-Parks (Devices 2 and 3), while those with larger ratio exhibit non-destructive Little-Parks oscillations, in agreement with theoretical work [158] and previous experiments in nanowires [115, 150], even though our device cross section is ellipsoid and not circular.

D.2 Angular and perpendicular magnetic field dependence

Here we analyze the dependence of I_c as a function of a rotating magnetic field of magnitude $B_r = 0.1$T, showing that the two parameters
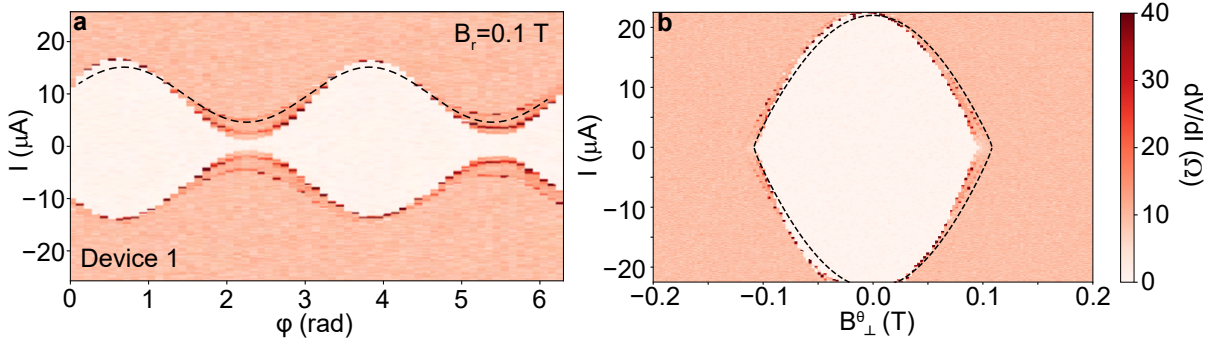
Figure D.2: Dependence of critical current on field angle and perpendicular field
(a,b) Colormaps of differential conductance, dV/dI, plotted as a function of bias current, I, and (a) angle between the vector magnetic field **B** and coil X, φ, and (b) magnetic field applied perpendicular the double nanowires with misalignment $\theta = 4.4°$, $B_\perp^\theta$. In (a), the critical current shows clear modulations and it reaches its minimum (maximum) when ϕ is such that $\theta = 90$ ($\theta = 0$), reflecting the phenomenological finding that the area threaded by parallel magnetic flux is smaller than the effective perpendicular parameter ($A_\parallel < A_\perp$). The critical perpendicular field found from the measurement in (b) is significantly smaller than the parallel critical field (0.1 T against 0.95 T), supporting the data and interpretation in (a). The asymmetry against $\pm B_\perp^\theta$ ($\varphi = 2.2$, 5.34 rad) in both (a) and (b) is attributed to coil remanence. The data was fitted with a calculation of the critical current, I_c (dashed lines), using the single hollow superconducting cylinder model. Reasonably good fits are obtained, with the fit quality decreased due to asymmetries. Data obtained from Device 1.

$A_\perp$ and $A_\parallel$ defined in Chapter 7 have to be different in order to have a modulating critical current versus a rotating magnetic field. Figure D.2a shows such a measurement from Device 1, where the black dashed-line is the model we use based on Eqs. 7.1,7.2 of Chapter 7. As the applied magnetic field is weak, we have $n = 0$ and the last term of Eqs. 7.2 ($\alpha_\parallel$) is negligible. As a result, $\alpha_\parallel$ and $\alpha_\perp$ would be identical if the two parameters are the same. A calculation from Ref. [163] for a solid cylinder found a factor of 2 between the parameters $A_\parallel$ and $A_\perp$ ($A_\perp/A_\parallel$=2), while we experimentally find a factor of $A_\perp/A_\parallel \approx 2.5 - 5$ for our elliptical hollow cross-sectional (13 nm shell) full-shell nanowires agreeing with the calculation on $A_\perp$ being larger than $A_\parallel$. Theoretical work on our specific system is needed to understand if these findings are consistent with theory.

Figure D.2b presents an $I - B$ measurement of Device 1 as a function of dV/dI at an angle perpendicular to nanowire axis. The black dashed-line is the fit, showing good agreement to the data, using the

same parameters as in Fig. D.2a and in Fig. 7.2.

D.3 Temperature dependence of Little-Parks oscillations

Figure D.3 presents Little-Parks oscillations of I_c and T_c of Device 3 to justify Eq. 7.4. The relation between the zero-field and finite-field critical current and critical temperature noted in Eq. 7.4 is verified in the data. Explicitly, at $B_\parallel^\theta = 0$ we measure $I_{sw}(B_\parallel^\theta = 0) = -24\ \mu A$ and $T_c(B_\parallel^\theta = 0) = 1.3$ K, and at $B_\parallel^\theta$ such that $\frac{\Phi_\parallel}{\Phi_0} = -1$ we measure $I_{sw}(\frac{\Phi_\parallel}{\Phi_0} = -1) = $
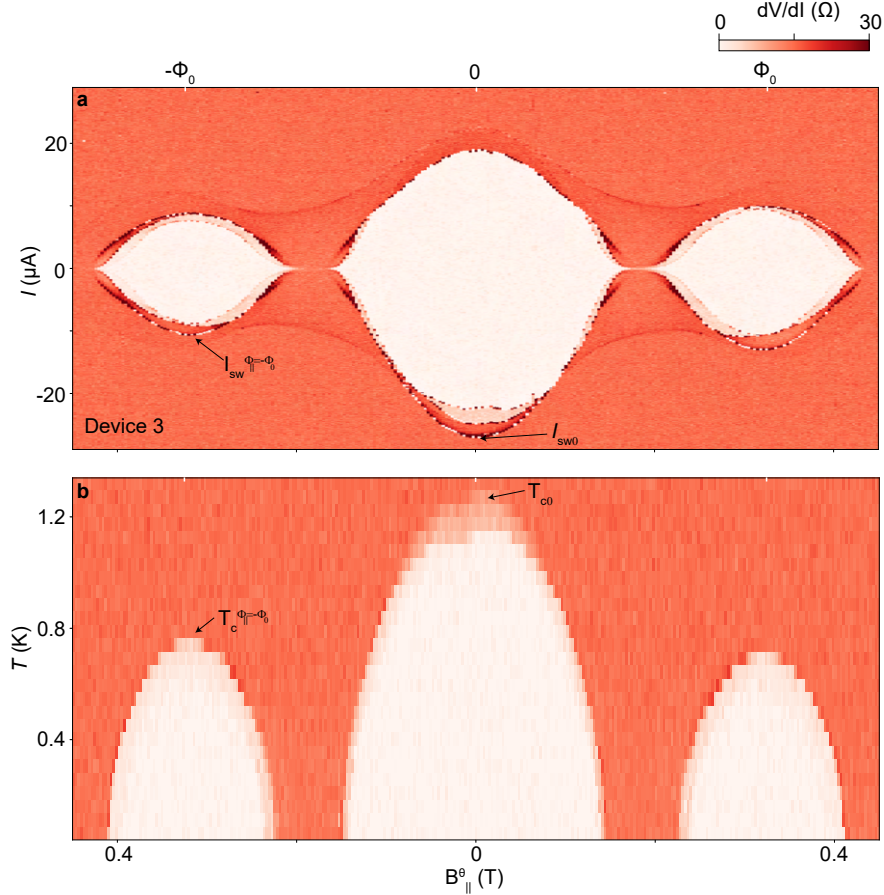
Figure D.3: Relation of I_c to T_c Little-Parks oscillations. (a,b) Colormaps of differential conductance, dV/dI, plotted as a function of magnetic field applied parallel to the double nanowires with misalignment $\theta = 10.7°$, $B_\parallel^\theta$, and (a) bias current, I swept from positive to negative values, at $T = 30$ mK and (b) refrigerator temperature, T, at $I = 0.7\ \mu A$. Little-Parks oscillations of I_c in (a) correlate to oscillations of T_c in (b), supporting our use of Eq. 7.4 in Chapter 7. Data obtained from Device 3.

$-10~\mu$A and $T_c(\frac{\Phi_\parallel}{\Phi_0} = -1) = 0.75$ K. Negative values of current are chosen to capture the switching current as the sweep direction is from positive to negative. For these values we verify the relation between I_c/I_{c0} and T_c/T_{c0} in Eq. 7.4 within 5%, assuming that $I_{sw} = I_c$. The lack of additional lobes beyond the ones at $\frac{\Phi_\parallel}{\Phi_0} = \pm 1$ is due to a large angle misalignment deduced from the fit in Fig. D.1d, which effectively reduces the critical magnetic field of the device.

ADDITIONAL DATA FOR INTERACTION OF A SUPERCONDUCTING ISLAND WITH A MAGNETIC IMPURITY

This appendix includes additional data for Chapter 8. Figure E.1 shows a scanning electron microscopy (SEM) image of the superconducting island - quantum dot - superconducting island (SI-QD-SI) device that was used to probe different $\frac{E_{cR}}{\Delta_R}$ regimes of superconducting Coulombic excitations. In that gate setting, the left SI (tuned by V_{SL}) is proximitized by the drain electrode, effectively forming a superconducting probe to study the $QD - SI_R$ system.

Figure E.1: Scanning electron microscopy (SEM) image of a superconducting island - quantum dot - superconducting island device.
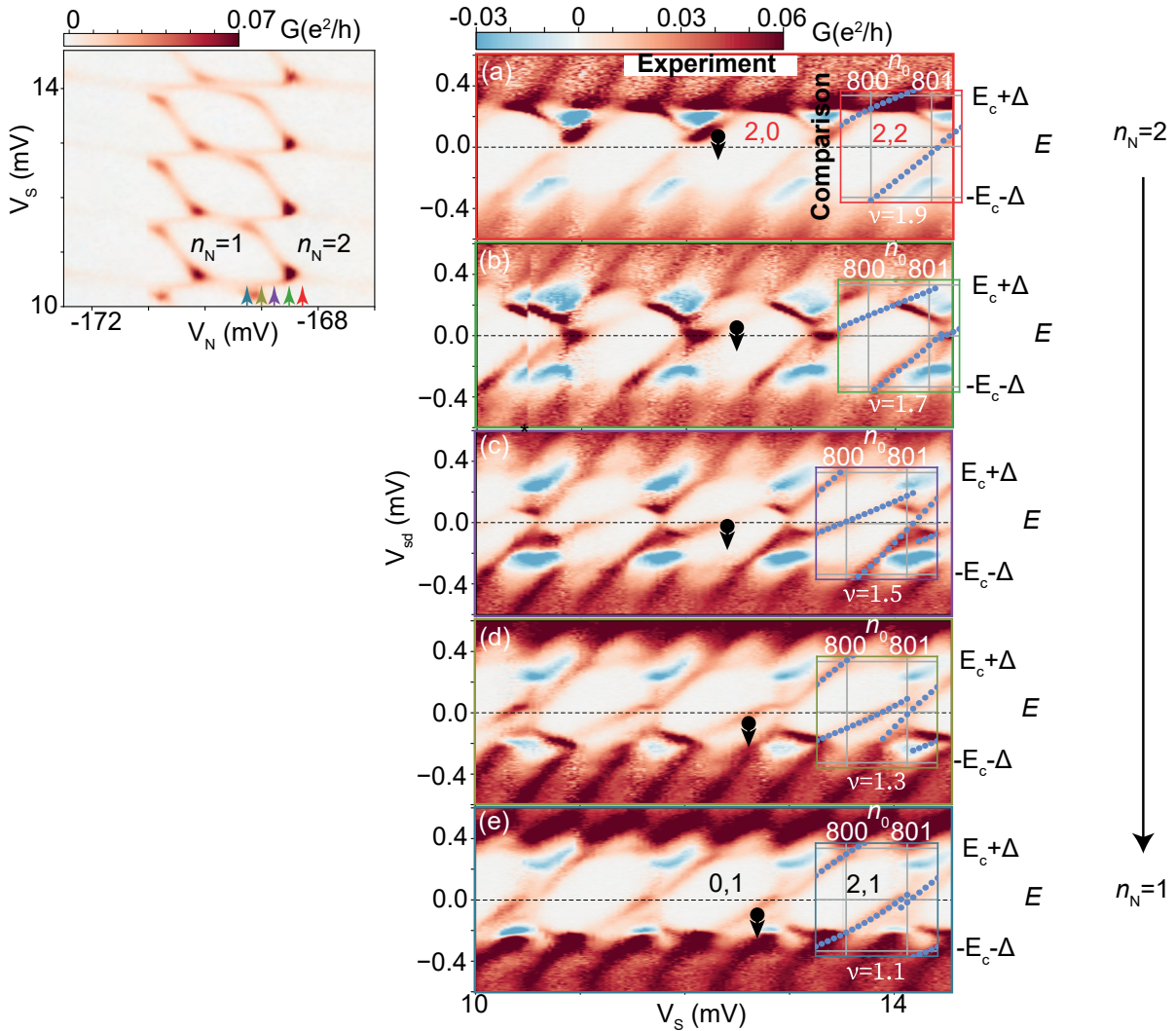
Figure E.2: Changes in the V_S dependence of superconducting Coulombic states across a $n_N = 2 \rightarrow 1$ transition. (a-e) Colormaps of G versus source-drain bias, V_{sd}, and SI gate voltage, V_S, at various settings of the QD gate voltage, V_N, indicated by (a) red, (b) green, (c) purple, (d) yellow and (e) cyan vertical arrows in the stability diagram on the left, which is a duplicate of Fig. 8.2a in Chapter 8. The tails of the black arrows are attached to a subgap state, while their heads point to the direction of the evolution of said state with varying V_N. The color scale is saturated to highlight subgap excitations. Charge numbers of the QD and the SI, n_N and n_S, are indicated in (a) and (e). An unwanted gate glitch is indicated by an asterisk in (b). Calculated SCE spectra using the same model parameters as in Fig. 8.2a in Chapter 8 are overlaid as blue dots on each panel for comparison. In the calculation, ν is fixed to the values indicated on top of each plot, and n_0 is swept. The calculation matches the position of positive-slope SCE, but does not account for negative-slope features, negative G features, and continuum features.

REFERENCES

[1] B. D. Josephson, "Possible new effects in superconductive tunnelling," *Physics Letters*, vol. 1, no. 7, pp. 251–253, Jul 1962.

[2] L. Yu, "Bound state in superconductors with paramagnetic impurities," *Acta Phys. Sin*, vol. 21, no. 1, 1965.

[3] H. Shiba, "Classical spins in superconductors," *Progress of theoretical Physics*, vol. 40, no. 3, pp. 435–451, 1968.

[4] A. Rusinov, "Superconductivity near a paramagnetic impurity," *Soviet Journal of Experimental and Theoretical Physics Letters*, vol. 9, p. 85, 1969.

[5] A. Yazdani, B. A. Jones, C. P. Lutz, M. F. Crommie, and D. M. Eigler, "Probing the local effects of magnetic impurities on superconductivity," *Science*, vol. 275, no. 5307, pp. 1767–1770, 1997. [Online]. Available: https://www.science.org/doi/abs/10.1126/science.275.5307.1767

[6] M. Ruby, F. Pientka, Y. Peng, F. von Oppen, B. W. Heinrich, and K. J. Franke, "End States and Subgap Structure in Proximity-Coupled Chains of Magnetic Adatoms," *Phys. Rev. Lett.*, vol. 115, no. 19, p. 197204, Nov 2015.

[7] Y. Oreg, G. Refael, and F. von Oppen, "Helical liquids and majorana bound states in quantum wires," *Phys. Rev. Lett.*, vol. 105, p. 177002, Oct 2010. [Online]. Available: https://link.aps.org/doi/10.1103/PhysRevLett.105.177002

[8] J. Klinovaja and D. Loss, "Time-reversal invariant parafermions in interacting Rashba nanowires," *Phys. Rev. B*, vol. 90, no. 4, p. 045118, Jul 2014.

[9] B. Béri and N. R. Cooper, "Topological Kondo Effect with Majorana Fermions," *Phys. Rev. Lett.*, vol. 109, no. 15, p. 156803, Oct 2012.

[10] A. Altland and R. Egger, "Multiterminal Coulomb-Majorana Junction," *Phys. Rev. Lett.*, vol. 110, no. 19, p. 196401, May 2013.

References

[11] V. Mourik, K. Zuo, S. M. Frolov, S. R. Plissard, E. P. A. M. Bakkers, and L. P. Kouwenhoven, "Signatures of Majorana Fermions in Hybrid Superconductor-Semiconductor Nanowire Devices," *Science*, May 2012. [Online]. Available: https://www.science.org/doi/10.1126/science.1222360

[12] M. T. Deng, S. Vaitiekėnas, E. B. Hansen, J. Danon, M. Leijnse, K. Flensberg, J. Nygård, P. Krogstrup, and C. M. Marcus, "Majorana bound state in a coupled quantum-dot hybrid-nanowire system," *Science*, vol. 354, no. 6319, pp. 1557–1562, Dec 2016.

[13] A. P. Higginbotham, S. M. Albrecht, G. Kiršanskas, W. Chang, F. Kuemmeth, P. Krogstrup, T. S. Jespersen, J. Nygård, K. Flensberg, and C. M. Marcus, "Parity lifetime of bound states in a proximitized semiconductor nanowire," *Nature Physics*, vol. 11, no. 12, pp. 1017–1021, 2015.

[14] S. M. Albrecht, A. P. Higginbotham, M. Madsen, F. Kuemmeth, T. S. Jespersen, J. Nygård, P. Krogstrup, and C. M. Marcus, "Exponential protection of zero modes in Majorana islands," *Nature*, vol. 531, no. 7593, pp. 206–209, Mar 2016.

[15] E. Prada, P. San-Jose, M. W. A. de Moor, A. Geresdi, E. J. H. Lee, J. Klinovaja, D. Loss, J. Nygård, R. Aguado, and L. P. Kouwenhoven, "From Andreev to Majorana bound states in hybrid superconductor–semiconductor nanowires," *Nat. Rev. Phys.*, vol. 2, pp. 575–594, Oct 2020.

[16] H. Pan and S. Das Sarma, "Physical mechanisms for zero-bias conductance peaks in Majorana nanowires," *Phys. Rev. Res.*, vol. 2, no. 1, p. 013377, Mar 2020.

[17] S. Baba, C. Jünger, S. Matsuo, A. Baumgartner, Y. Sato, H. Kamata, K. Li, S. Jeppesen, L. Samuelson, H. Q. Xu, C. Schönenberger, and S. Tarucha, "Cooper-pair splitting in two parallel InAs nanowires," *New J. Phys.*, vol. 20, no. 6, p. 063021, Jun 2018.

[18] K. Ueda, S. Matsuo, H. Kamata, S. Baba, Y. Sato, Y. Takeshige, K. Li, S. Jeppesen, L. Samuelson, H. Xu, and S. Tarucha, "Dominant nonlocal superconducting proximity effect due to electron-electron interaction in a ballistic double nanowire," *Sci. Adv.*, vol. 5, no. 10, p. eaaw2194, Oct 2019.

[19] T. Kanne, D. Olsteins, M. Marnauza, A. Vekris, J. C. E. Saldaña, S. Lorič, R. D. Schlosser, D. Ross, S. Csonka, K. Grove-Rasmussen, and J. Nygård, "Double Nanowires for Hybrid Quantum Devices," *Adv. Funct. Mater.*, vol. n/a, no. n/a, p. 2107926, Nov 2021.

[20] A. A. Abrikosov and L. P. Gor'kov, "Contribution to the theory of superconducting alloys with paramagnetic impurities," *Zhur. Eksptl'. i Teoret. Fiz.*, vol. 39, 1960.

[21] R. Groff and R. Parks, "Fluxoid quantization and field-induced depairing in a hollow superconducting microcylinder," *Physical Review*, vol. 176, no. 2, p. 567, 1968.

[22] I. O. Kulik, "Macroscopic Quantization and the Proximity Effect in S-N-S Junctions," *Soviet Journal of Experimental and Theoretical Physics*, vol. 30, p. 944, 1969. [Online]. Available: https://ui.adsabs.harvard.edu/abs/1969JETP...30..944K/abstract

[23] P. Krogstrup, N. Ziino, W. Chang, S. Albrecht, M. Madsen, E. Johnson, J. Nygård, C. M. Marcus, and T. Jespersen, "Epitaxy of semiconductor–superconductor nanowires," *Nature materials*, vol. 14, no. 4, pp. 400–406, 2015.

[24] J.-D. Pillet, C. H. L. Quay, P. Morfin, C. Bena, A. L. Yeyati, and P. Joyez, "Andreev bound states in supercurrent-carrying carbon nanotubes revealed," *Nat. Phys.*, vol. 6, pp. 965–969, Dec 2010.

[25] K. J. Franke, G. Schulze, and J. I. Pascual, "Competition of superconducting phenomena and kondo screening at the nanoscale," *Science*, vol. 332, no. 6032, pp. 940–944, 2011. [Online]. Available: https://www.science.org/doi/abs/10.1126/science.1202204

[26] J. C. E. Saldaña, A. Vekris, L. Pavešič, P. Krogstrup, R. Žitko, K. Grove-Rasmussen, and J. Nygård, "Coulombic subgap states," *arXiv*, Jan 2021. [Online]. Available: https://arxiv.org/abs/2101.10794v2

[27] A. E. G. Mikkelsen, P. Kotetes, P. Krogstrup, and K. Flensberg, "Hybridization at superconductor-semiconductor interfaces," *Phys. Rev. X*, vol. 8, p. 031040, Aug 2018. [Online]. Available: https://link.aps.org/doi/10.1103/PhysRevX.8.031040

[28] S. M. Albrecht, E. B. Hansen, A. P. Higginbotham, F. Kuemmeth, T. S. Jespersen, J. Nygård, P. Krogstrup, J. Danon, K. Flensberg, and C. M. Marcus, "Transport Signatures of Quasiparticle Poisoning in a Majorana Island," *Phys. Rev. Lett.*, vol. 118, no. 13, p. 137701, Mar 2017.

[29] M. Tinkham, *Introduction to superconductivity*. Courier Corporation, 2004.

[30] M. Iansiti, A. T. Johnson, C. J. Lobb, and M. Tinkham, "Quantum tunneling and low-voltage resistance in small superconducting tunnel junctions," *Phys. Rev. B*, vol. 40, no. 16, pp. 11 370–11 373(R), Dec 1989.

[31] R. L. Kautz and J. M. Martinis, "Noise-affected I-V curves in small hysteretic Josephson junctions," *Phys. Rev. B*, vol. 42, no. 16, pp. 9903–9937, Dec 1990.

[32] J. A. Van Dam, Y. V. Nazarov, E. P. Bakkers, S. De Franceschi, and L. P. Kouwenhoven, "Supercurrent reversal in quantum dots," *Nature*, vol. 442, no. 7103, pp. 667–670, 2006.

[33] H. I. Jørgensen, T. Novotný, K. Grove-Rasmussen, K. Flensberg, and P. E. Lindelof, "Critical Current 0-π Transition in Designed Josephson Quantum Dot Junctions," *Nano Lett.*, vol. 7, no. 8, pp. 2441–2445, Aug 2007.

[34] W. G. van der Wiel, S. De Franceschi, J. M. Elzerman, T. Fujisawa, S. Tarucha, and L. P. Kouwenhoven, "Electron transport through double quantum dots," *Rev. Mod. Phys.*, vol. 75, no. 1, pp. 1–22, Dec 2002.

[35] D. Sherman, J. S. Yodh, S. M. Albrecht, J. Nygård, P. Krogstrup, and C. M. Marcus, "Normal, superconducting and topological regimes of hybrid double quantum dots - Nature Nanotechnology," *Nat. Nanotechnol.*, vol. 12, no. 3, pp. 212–217, Mar 2017.

REFERENCES

[36] J. Shen, S. Heedt, F. Borsoi, B. van Heck, S. Gazibegovic, R. L. M. Op het Veld, D. Car, J. A. Logan, M. Pendharkar, S. J. J. Ramakers, G. Wang, D. Xu, D. Bouman, A. Geresdi, C. J. Palmstrøm, E. P. A. M. Bakkers, and L. P. Kouwenhoven, "Parity transitions in the superconducting ground state of hybrid InSb–Al Coulomb islands - Nature Communications," *Nat. Commun.*, vol. 9, no. 4801, pp. 1–8, Nov 2018.

[37] P. Lafarge, P. Joyez, D. Esteve, C. Urbina, and M. H. Devoret, "Measurement of the even-odd free-energy difference of an isolated superconductor," *Phys. Rev. Lett.*, vol. 70, pp. 994–997, Feb 1993. [Online]. Available: https://link.aps.org/doi/10.1103/PhysRevLett.70.994

[38] M. T. Tuominen, J. M. Hergenrother, T. S. Tighe, and M. Tinkham, "Experimental evidence for parity-based 2e periodicity in a superconducting single-electron tunneling transistor," *Phys. Rev. Lett.*, vol. 69, pp. 1997–2000, Sep 1992. [Online]. Available: https://link.aps.org/doi/10.1103/PhysRevLett.69.1997

[39] V. F. Maisi, S. V. Lotkhov, A. Kemppinen, A. Heimes, J. T. Muhonen, and J. P. Pekola, "Excitation of single quasiparticles in a small superconducting al island connected to normal-metal leads by tunnel junctions," *Phys. Rev. Lett.*, vol. 111, p. 147001, Oct 2013. [Online]. Available: https://link.aps.org/doi/10.1103/PhysRevLett.111.147001

[40] D. Goldhaber-Gordon, H. Shtrikman, D. Mahalu, D. Abusch-Magder, U. Meirav, and M. A. Kastner, "Kondo effect in a single-electron transistor - Nature," *Nature*, vol. 391, no. 6663, pp. 156–159, Jan 1998.

[41] L. Kouwenhoven and L. Glazman, "Revival of the Kondo effect," *Phys. World*, vol. 14, no. 1, pp. 33–38, Jan 2001.

[42] E. J. H. Lee, X. Jiang, M. Houzet, R. Aguado, C. M. Lieber, and S. De Franceschi, "Spin-resolved Andreev levels and parity crossings in hybrid superconductor–semiconductor nanostructures," *Nat. Nanotechnol.*, vol. 9, pp. 79–84, Jan 2014.

[43] A. Jellinggaard, K. Grove-Rasmussen, M. H. Madsen, and J. Nygård, "Tuning Yu-Shiba-Rusinov states in a quantum dot," *Phys. Rev. B*, vol. 94, no. 6, p. 064520, Aug 2016.

[44] L. Pavešić, D. Bauernfeind, and R. Žitko, "Subgap states in superconducting islands," *Phys. Rev. B*, vol. 104, no. 24, p. L241409, Dec 2021.

[45] G. de Lange, B. van Heck, A. Bruno, D. J. van Woerkom, A. Geresdi, S. R. Plissard, E. P. A. M. Bakkers, A. R. Akhmerov, and L. DiCarlo, "Realization of microwave quantum circuits using hybrid superconducting-semiconducting nanowire josephson elements," *Phys. Rev. Lett.*, vol. 115, p. 127002, Sep 2015. [Online]. Available: https://link.aps.org/doi/10.1103/PhysRevLett.115.127002

[46] T. W. Larsen, K. D. Petersson, F. Kuemmeth, T. S. Jespersen, P. Krogstrup, J. Nygård, and C. M. Marcus, "Semiconductor-nanowire-based superconducting qubit," *Phys. Rev. Lett.*, vol. 115, p. 127001, Sep 2015. [Online]. Available: https://link.aps.org/doi/10.1103/PhysRevLett.115.127001

[47] L. Hofstetter, S. Csonka, J. Nygård, and C. Schönenberger, "Cooper pair splitter realized in a two-quantum-dot Y-junction," *Nature*, vol. 461, pp. 960–963, Oct 2009.

[48] D. J. Carrad, M. Bjergfelt, T. Kanne, M. Aagesen, F. Krizek, E. M. Fiordaliso, E. Johnson, J. Nygård, and T. S. Jespersen, "Shadow Epitaxy for In Situ Growth of Generic Semiconductor/Superconductor Hybrids," *Adv. Mater.*, vol. 32, no. 23, p. 1908411, Jun 2020.

[49] D. Aasen, M. Hell, R. V. Mishmash, A. Higginbotham, J. Danon, M. Leijnse, T. S. Jespersen, J. A. Folk, C. M. Marcus, K. Flensberg, and J. Alicea, "Milestones Toward Majorana-Based Quantum Computing," *Phys. Rev. X*, vol. 6, no. 3, p. 031016, Aug 2016.

[50] L. Hofstetter, S. Csonka, J. Nygård, and C. Schönenberger, "Cooper pair splitter realized in a two-quantum-dot y-junction," *Nature*, vol. 461, no. 7266, pp. 960–963, 2009.

[51] K. Grove-Rasmussen, G. Steffensen, A. Jellinggaard, M. H. Madsen, R. Žitko, J. Paaske, and J. Nygård, "Yu–shiba–rusinov screening of spins in double quantum dots," *Nature Communications*, vol. 9, no. 1, pp. 1–6, 2018.

[52] M. Bjergfelt, D. J. Carrad, T. Kanne, M. Aagesen, E. M. Fiordaliso, E. Johnson, B. Shojaei, C. J. Palmstrøm, P. Krogstrup, T. S. Jespersen, and J. Nygård, "Superconducting vanadium/indium-arsenide hybrid nanowires," *Nanotechnology*, vol. 30, no. 29, p. 294005, 2019.

[53] R. S. Deacon, Y. Tanaka, A. Oiwa, R. Sakano, K. Yoshida, K. Shibata, K. Hirakawa, and S. Tarucha, "Tunneling Spectroscopy of Andreev Energy Levels in a Quantum Dot Coupled to a Superconductor," *Phys. Rev. Lett.*, vol. 104, no. 7, p. 076805, Feb 2010.

[54] A. Vekris, J. C. E. Saldaña, T. Kanne, M. Marnauza, D. Olsteins, F. Fan, X. Li, T. Hvid-Olsen, X. Qiu, H. Xu, J. Nygård, and K. Grove-Rasmussen, "Josephson junctions in double nanowires bridged by in-situ deposited superconductors," *Phys. Rev. Research*, vol. 3, p. 033240, Sep 2021. [Online]. Available: https://link.aps.org/doi/10.1103/PhysRevResearch.3.033240

[55] N. Y. Yao, C. P. Moca, I. Weymann, J. D. Sau, M. D. Lukin, E. A. Demler, and G. Zaránd, "Phase diagram and excitations of a Shiba molecule," *Phys. Rev. B*, vol. 90, no. 24, p. 241108(R), Dec 2014.

[56] E. Gaidamauskas, J. Paaske, and K. Flensberg, "Majorana bound states in two-channel time-reversal-symmetric nanowire systems," *Phys. Rev. Lett.*, vol. 112, p. 126402, Mar 2014. [Online]. Available: https://link.aps.org/doi/10.1103/PhysRevLett.112.126402

[57] H. Ebisu, B. Lu, J. Klinovaja, and Y. Tanaka, "Theory of time-reversal topological superconductivity in double Rashba wires: symmetries of Cooper pairs and Andreev bound states," *Progress of Theoretical and Experimental Physics*, vol. 2016, no. 8, 08 2016, 083I01. [Online]. Available: https://doi.org/10.1093/ptep/ptw094

[58] C. Schrade, M. Thakurathi, C. Reeg, S. Hoffman, J. Klinovaja, and D. Loss, "Low-field topological threshold in majorana double nanowires," *Phys. Rev. B*, vol. 96, p. 035306, Jul 2017. [Online]. Available: https://link.aps.org/doi/10.1103/PhysRevB.96.035306

[59] C. Reeg, J. Klinovaja, and D. Loss, "Destructive interference of direct and crossed andreev pairing in a system of two nanowires coupled via an *s*-wave superconductor," *Phys. Rev. B*, vol. 96, p. 081301(R), Aug 2017. [Online]. Available: https://link.aps.org/doi/10.1103/PhysRevB.96.081301

References

[60] C. Schrade and L. Fu, "Parity-controlled 2π josephson effect mediated by majorana kramers pairs," *Phys. Rev. Lett.*, vol. 120, p. 267002, Jun 2018. [Online]. Available: https://link.aps.org/doi/10.1103/PhysRevLett.120.267002

[61] M. Thakurathi, P. Simon, I. Mandal, J. Klinovaja, and D. Loss, "Majorana kramers pairs in rashba double nanowires with interactions and disorder," *Phys. Rev. B*, vol. 97, p. 045415, Jan 2018. [Online]. Available: https://link.aps.org/doi/10.1103/PhysRevB.97.045415

[62] O. Dmytruk, M. Thakurathi, D. Loss, and J. Klinovaja, "Majorana bound states in double nanowires with reduced zeeman thresholds due to supercurrents," *Phys. Rev. B*, vol. 99, p. 245416, Jun 2019. [Online]. Available: https://link.aps.org/doi/10.1103/PhysRevB.99.245416

[63] M. Thakurathi, D. Chevallier, D. Loss, and J. Klinovaja, "Transport signatures of bulk topological phases in double rashba nanowires probed by spin-polarized stm," *Phys. Rev. Research*, vol. 2, p. 023197, May 2020. [Online]. Available: https://link.aps.org/doi/10.1103/PhysRevResearch.2.023197

[64] P. Kotetes, M. T. Mercaldo, and M. Cuoco, "Synthetic weyl points and chiral anomaly in majorana devices with nonstandard andreev-bound-state spectra," *Phys. Rev. Lett.*, vol. 123, p. 126802, Sep 2019. [Online]. Available: https://link.aps.org/doi/10.1103/PhysRevLett.123.126802

[65] M. Papaj, Z. Zhu, and L. Fu, "Multichannel charge kondo effect and non-fermi-liquid fixed points in conventional and topological superconductor islands," *Phys. Rev. B*, vol. 99, p. 014512, Jan 2019. [Online]. Available: https://link.aps.org/doi/10.1103/PhysRevB.99.014512

[66] A. Haim and Y. Oreg, "Time-reversal-invariant topological superconductivity in one and two dimensions," *Physics Reports*, vol. 825, pp. 1–48, 2019. [Online]. Available: https://www.sciencedirect.com/science/article/pii/S0370157319302613

[67] M. R. Galpin, A. K. Mitchell, J. Temaismithi, D. E. Logan, B. Béri, and N. R. Cooper, "Conductance fingerprint of majorana fermions in the topological kondo effect," *Phys. Rev. B*, vol. 89, p. 045143, Jan 2014. [Online]. Available: https://link.aps.org/doi/10.1103/PhysRevB.89.045143

[68] P. Krogstrup, N. L. B. Ziino, W. Chang, S. M. Albrecht, M. H. Madsen, E. Johnson, J. Nygård, C. M. Marcus, and T. S. Jespersen, "Epitaxy of semiconductor–superconductor nanowires," *Nat. Mater.*, vol. 14, no. 4, pp. 400–406, Jan 2015.

[69] J. C. Estrada Saldaña, A. Vekris, G. Steffensen, R. Žitko, P. Krogstrup, J. Paaske, K. Grove-Rasmussen, and J. Nygård, "Supercurrent in a Double Quantum Dot," *Phys. Rev. Lett.*, vol. 121, no. 25, p. 257701, Dec 2018.

[70] J. C. Estrada Saldaña, A. Vekris, R. Žitko, G. Steffensen, P. Krogstrup, J. Paaske, K. Grove-Rasmussen, and J. Nygård, "Two-impurity Yu-Shiba-Rusinov states in coupled quantum dots," *Phys. Rev. B*, vol. 102, no. 19, p. 195143, Nov 2020.

[71] M. Valentini, F. Peñaranda, A. Hofmann, M. Brauns, R. Hauschild, P. Krogstrup, P. San-Jose, E. Prada, R. Aguado, and G. Katsaros, "Non-topological zero bias peaks in full-shell nanowires induced by flux tunable Andreev states," *arXiv*, Aug 2020. [Online]. Available: https://arxiv.org/abs/2008.02348v2

[72] J. C. Estrada Saldaña, A. Vekris, V. Sosnovtseva, T. Kanne, P. Krogstrup, K. Grove-Rasmussen, and J. Nygård, "Temperature induced shifts of Yu–Shiba–Rusinov resonances in nanowire-based hybrid quantum dots," *Commun. Phys.*, vol. 3, no. 125, pp. 1–11, Jul 2020.

[73] D. Razmadze, E. C. T. O'Farrell, P. Krogstrup, and C. M. Marcus, "Quantum Dot Parity Effects in Trivial and Topological Josephson Junctions," *Phys. Rev. Lett.*, vol. 125, no. 11, p. 116803, Sep 2020.

[74] M. R. Buitelaar, T. Nussbaumer, and C. Schönenberger, "Quantum Dot in the Kondo Regime Coupled to Superconductors," *Phys. Rev. Lett.*, vol. 89, no. 25, p. 256801, Dec 2002.

[75] R. S. Deacon, Y. Tanaka, A. Oiwa, R. Sakano, K. Yoshida, K. Shibata, K. Hirakawa, and S. Tarucha, "Kondo-enhanced Andreev transport in single self-assembled InAs quantum dots contacted with normal and superconducting leads," *Phys. Rev. B*, vol. 81, no. 12, p. 121308(R), Mar 2010.

[76] S. Li, N. Kang, P. Caroff, and H. Q. Xu, "$0-\pi$ phase transition in hybrid superconductor–InSb nanowire quantum dot devices," *Phys. Rev. B*, vol. 95, no. 1, p. 014515, Jan 2017.

[77] E. J. H. Lee, X. Jiang, R. Žitko, R. Aguado, C. M. Lieber, and S. De Franceschi, "Scaling of subgap excitations in a superconductor-semiconductor nanowire quantum dot," *Phys. Rev. B*, vol. 95, no. 18, p. 180502(R), May 2017.

[78] Z. Su, A. B. Tacla, M. Hocevar, D. Car, S. R. Plissard, E. P. A. M. Bakkers, A. J. Daley, D. Pekker, and S. M. Frolov, "Andreev molecules in semiconductor nanowire double quantum dots," *Nat. Commun.*, vol. 8, no. 585, pp. 1–6, Sep 2017.

[79] J. Gramich, A. Baumgartner, and C. Schönenberger, "Andreev bound states probed in three-terminal quantum dots," *Phys. Rev. B*, vol. 96, no. 19, p. 195418, Nov 2017.

[80] Z. Su, R. Žitko, P. Zhang, H. Wu, D. Car, S. R. Plissard, S. Gazibegovic, G. Badawy, M. Hocevar, J. Chen, E. P. A. M. Bakkers, and S. M. Frolov, "Erasing odd-parity states in semiconductor quantum dots coupled to superconductors," *Phys. Rev. B*, vol. 101, no. 23, p. 235315, Jun 2020.

[81] R. Žitko, J. S. Lim, R. López, and R. Aguado, "Shiba states and zero-bias anomalies in the hybrid normal-superconductor Anderson model," *Phys. Rev. B*, vol. 91, no. 4, p. 045441, Jan 2015.

[82] G. Kiršanskas, M. Goldstein, K. Flensberg, L. I. Glazman, and J. Paaske, "Yu-Shiba-Rusinov states in phase-biased superconductor–quantum dot–superconductor junctions," *Phys. Rev. B*, vol. 92, no. 23, p. 235422, Dec 2015.

REFERENCES

[83] K. Satori, H. Shiba, O. Sakai, and Y. Shimizu, "Numerical Renormalization Group Study of Magnetic Impurities in Superconductors," *J. Phys. Soc. Jpn.*, vol. 61, no. 9, pp. 3239–3254, Sep 1992.

[84] J. Bauer, A. Oguri, and A. C. Hewson, "Spectral properties of locally correlated electrons in a Bardeen–Cooper–Schrieffer," *J. Phys.: Condens. Matter*, vol. 19, no. 48, p. 486211, Nov 2007.

[85] A. V. Rozhkov, D. P. Arovas, and F. Guinea, "Josephson coupling through a quantum dot," *Phys. Rev. B*, vol. 64, no. 23, p. 233301, Nov 2001.

[86] F. S. Bergeret, A. L. Yeyati, and A. Martín-Rodero, "Interplay between josephson effect and magnetic interactions in double quantum dots," *Phys. Rev. B*, vol. 74, p. 132505, Oct 2006. [Online]. Available: https://link.aps.org/doi/10.1103/PhysRevB.74.132505

[87] J.-P. Cleuziou, W. Wernsdorfer, V. Bouchiat, T. Ondarçuhu, and M. Monthioux, "Carbon nanotube superconducting quantum interference device," *Nat. Nanotechnol.*, vol. 1, pp. 53–59, Oct 2006.

[88] K. Grove-Rasmussen, H. I. Jørgensen, and P. E. Lindelof, "Kondo resonance enhanced supercurrent in single wall carbon nanotube Josephson junctions," *New J. Phys.*, vol. 9, no. 5, p. 124, May 2007.

[89] A. Eichler, R. Deblock, M. Weiss, C. Karrasch, V. Meden, C. Schönenberger, and H. Bouchiat, "Tuning the Josephson current in carbon nanotubes with the Kondo effect," *Phys. Rev. B*, vol. 79, no. 16, p. 161407(R), Apr 2009.

[90] S. De Franceschi, L. Kouwenhoven, C. Schönenberger, and W. Wernsdorfer, "Hybrid superconductor–quantum dot devices," *Nat. Nanotechnol.*, vol. 5, pp. 703–711, Oct 2010.

[91] R. Žitko, M. Lee, R. López, R. Aguado, and M.-S. Choi, "Josephson current in strongly correlated double quantum dots," *Phys. Rev. Lett.*, vol. 105, p. 116803, Sep 2010. [Online]. Available: https://link.aps.org/doi/10.1103/PhysRevLett.105.116803

[92] A. Martín-Rodero and A. Levy Yeyati, "Josephson and andreev transport through quantum dots," *Advances in Physics*, vol. 60, no. 6, pp. 899–958, 2011.

[93] R. Maurand, T. Meng, E. Bonet, S. Florens, L. Marty, and W. Wernsdorfer, "First-Order $0-\pi$ Quantum Phase Transition in the Kondo Regime of a Superconducting Carbon-Nanotube Quantum Dot," *Phys. Rev. X*, vol. 2, no. 1, p. 011009, Feb 2012.

[94] B.-K. Kim, Y.-H. Ahn, J.-J. Kim, M.-S. Choi, M.-H. Bae, K. Kang, J. S. Lim, R. López, and N. Kim, "Transport Measurement of Andreev Bound States in a Kondo-Correlated Quantum Dot," *Phys. Rev. Lett.*, vol. 110, no. 7, p. 076803, Feb 2013.

[95] R. Delagrange, D. J. Luitz, R. Weil, A. Kasumov, V. Meden, H. Bouchiat, and R. Deblock, "Manipulating the magnetic state of a carbon nanotube Josephson junction using the superconducting phase," *Phys. Rev. B*, vol. 91, no. 24, p. 241401(R), Jun 2015.

[96] R. Delagrange, R. Weil, A. Kasumov, M. Ferrier, H. Bouchiat, and R. Deblock, "0-π Quantum transition in a carbon nanotube Josephson junction: Universal phase dependence and orbital degeneracy," *Physica B*, vol. 536, pp. 211–222, May 2018.

[97] V. Meden, "The Anderson–Josephson quantum dot—a theory perspective," *J. Phys.: Condens. Matter*, vol. 31, no. 16, p. 163001, Feb 2019.

[98] J. C. Estrada Saldaña, R. Žitko, J. P. Cleuziou, E. J. H. Lee, V. Zannier, D. Ercolani, L. Sorba, R. Aguado, and S. De Franceschi, "Charge localization and reentrant superconductivity in a quasi-ballistic InAs nanowire coupled to superconductors," *Sci. Adv.*, vol. 5, no. 7, p. eaav1235, Jul 2019.

[99] S. Baba, J. Sailer, R. S. Deacon, A. Oiwa, K. Shibata, K. Hirakawa, and S. Tarucha, "Superconducting transport in single and parallel double inas quantum dot josephson junctions with nb-based superconducting electrodes," *Applied Physics Letters*, vol. 107, no. 22, p. 222602, 2015.

[100] R. S. Deacon, A. Oiwa, J. Sailer, S. Baba, Y. Kanai, K. Shibata, K. Hirakawa, and S. Tarucha, "Cooper pair splitting in parallel quantum dot Josephson junctions," *Nat. Commun.*, vol. 6, no. 7446, pp. 1–7, Jul 2015.

[101] B. Probst, F. Domínguez, A. Schroer, A. L. Yeyati, and P. Recher, "Signatures of nonlocal cooper-pair transport and of a singlet-triplet transition in the critical current of a double-quantum-dot josephson junction," *Physical Review B*, vol. 94, no. 15, p. 155445, 2016.

[102] A. Das, Y. Ronen, M. Heiblum, D. Mahalu, A. V. Kretinin, and H. Shtrikman, "High-efficiency Cooper pair splitting demonstrated by two-particle conductance resonance and positive noise cross-correlation," *Nat. Commun.*, vol. 3, no. 1165, pp. 1–6, Nov 2012.

[103] O. Kürtössy, Z. Scherübl, G. Fülöp, I. E. Lukács, T. Kanne, J. Nygård, P. Makk, and S. Csonka, "Andreev Molecule in Parallel InAs Nanowires," *Nano Lett.*, vol. 21, no. 19, pp. 7929–7937, Oct 2021.

[104] S. Guiducci, M. Carrega, F. Taddei, G. Biasiol, H. Courtois, F. Beltram, and S. Heun, "Full electrostatic control of quantum interference in an extended trenched Josephson junction," *Phys. Rev. B*, vol. 99, no. 23, p. 235419, Jun 2019.

[105] R. Žitko, O. Bodensiek, and T. Pruschke, "Effects of magnetic anisotropy on the subgap excitations induced by quantum impurities in a superconducting host," *Phys. Rev. B*, vol. 83, no. 5, p. 054512, Feb 2011.

[106] C. Beenakker and H. van Houten, "The superconducting quantum point contact," in *Nanostructures and Mesoscopic Systems*, W. P. Kirk and M. A. Reed, Eds. Academic Press, 1992, pp. 481–497. [Online]. Available: https://www.sciencedirect.com/science/article/pii/B9780124096608500511

[107] Z. Scherübl, G. Fülöp, C. P. Moca, J. Gramich, A. Baumgartner, P. Makk, T. Elalaily, C. Schönenberger, J. Nygård, G. Zaránd, and S. Csonka, "Large spatial extension of the zero-energy Yu–Shiba–Rusinov state in a magnetic field," *Nat. Commun.*, vol. 11, no. 1834, pp. 1–9, Apr 2020.

REFERENCES

[108] H. I. Jørgensen, K. Grove-Rasmussen, K.-Y. Wang, A. Blackburn, K. Flensberg, P. Linde-lof, and D. Williams, "Singlet–triplet physics and shell filling in carbon nanotube double quantum dots," *Nature Physics*, vol. 4, no. 7, pp. 536–539, 2008.

[109] T. Meng, S. Florens, and P. Simon, "Self-consistent description of Andreev bound states in Josephson quantum dot devices," *Phys. Rev. B*, vol. 79, no. 22, p. 224521, Jun 2009.

[110] A. Kogan, S. Amasha, D. Goldhaber-Gordon, G. Granger, M. A. Kastner, and H. Shtrik-man, "Measurements of Kondo and Spin Splitting in Single-Electron Transistors," *Phys. Rev. Lett.*, vol. 93, no. 16, p. 166602, Oct 2004.

[111] L. G. Herrmann, F. Portier, P. Roche, A. L. Yeyati, T. Kontos, and C. Strunk, "Carbon Nanotubes as Cooper-Pair Beam Splitters," *Phys. Rev. Lett.*, vol. 104, no. 2, p. 026801, Jan 2010.

[112] P. Recher, E. V. Sukhorukov, and D. Loss, "Andreev tunneling, Coulomb blockade, and resonant transport of nonlocal spin-entangled electrons," *Phys. Rev. B*, vol. 63, no. 16, p. 165314, Apr 2001.

[113] Z. Scherübl, A. Pályi, and S. Csonka, "Transport signatures of an Andreev molecule in a quantum dot-superconductor-quantum dot setup." *Beilstein J. Nanotechnol.*, vol. 10, pp. 363–378, 2019.

[114] A. Vekris, J. C. Estrada Saldaña, J. de Bruijckere, S. Lorić, T. Kanne, M. Marnauza, D. Olsteins, J. Nygård, and K. Grove-Rasmussen, "Asymmetric Little–Parks oscillations in full shell double nanowires - Scientific Reports," *Sci. Rep.*, vol. 11, no. 19034, pp. 1–8, Sep 2021. [Online]. Available: https://doi.org/10.1038/s41598-021-97780-9

[115] S. Vaitiekėnas, G. W. Winkler, B. van Heck, T. Karzig, M.-T. Deng, K. Flensberg, L. I. Glazman, C. Nayak, P. Krogstrup, R. M. Lutchyn, and C. M. Marcus, "Flux-induced topological superconductivity in full-shell nanowires," *Science*, vol. 367, no. 6485, p. eaav3392, Mar 2020.

[116] F. Peñaranda, R. Aguado, P. San-Jose, and E. Prada, "Even-odd effect and majorana states in full-shell nanowires," *Phys. Rev. Research*, vol. 2, p. 023171, May 2020. [Online]. Available: https://link.aps.org/doi/10.1103/PhysRevResearch.2.023171

[117] B. M. Terhal, F. Hassler, and D. P. DiVincenzo, "From majorana fermions to topological order," *Phys. Rev. Lett.*, vol. 108, p. 260504, Jun 2012. [Online]. Available: https://link.aps.org/doi/10.1103/PhysRevLett.108.260504

[118] S. Plugge, L. A. Landau, E. Sela, A. Altland, K. Flensberg, and R. Egger, "Roadmap to majorana surface codes," *Phys. Rev. B*, vol. 94, p. 174514, Nov 2016. [Online]. Available: https://link.aps.org/doi/10.1103/PhysRevB.94.174514

[119] S. Plugge, A. Rasmussen, R. Egger, and K. Flensberg, "Majorana box qubits," *New J. Phys.*, vol. 19, no. 1, p. 012001, jan 2017. [Online]. Available: https://doi.org/10.1088/1367-2630/aa54e1

154

[120] B. Béri, "Majorana-klein hybridization in topological superconductor junctions," *Phys. Rev. Lett.*, vol. 110, p. 216803, May 2013. [Online]. Available: https://link.aps.org/doi/10.1103/PhysRevLett.110.216803

[121] P. Joyez, P. Lafarge, A. Filipe, D. Esteve, and M. H. Devoret, "Observation of parity-induced suppression of josephson tunneling in the superconducting single electron transistor," *Phys. Rev. Lett.*, vol. 72, pp. 2458–2461, Apr 1994. [Online]. Available: https://link.aps.org/doi/10.1103/PhysRevLett.72.2458

[122] D. V. Averin and Yu. V. Nazarov, "Single-electron charging of a superconducting island," *Phys. Rev. Lett.*, vol. 69, no. 13, pp. 1993–1996, Sep 1992.

[123] T. M. Eiles, J. M. Martinis, and M. H. Devoret, "Even-odd asymmetry of a superconductor revealed by the Coulomb blockade of Andreev reflection," *Phys. Rev. Lett.*, vol. 70, no. 12, pp. 1862–1865, Mar 1993.

[124] G. C. Ménard, F. K. Malinowski, D. Puglia, D. I. Pikulin, T. Karzig, B. Bauer, P. Krogstrup, and C. M. Marcus, "Suppressing quasiparticle poisoning with a voltage-controlled filter," *Phys. Rev. B*, vol. 100, p. 165307, Oct 2019. [Online]. Available: https://link.aps.org/doi/10.1103/PhysRevB.100.165307

[125] J. E. Sestoft, T. Kanne, A. N. Gejl, M. von Soosten, J. S. Yodh, D. Sherman, B. Tarasinski, M. Wimmer, E. Johnson, M. Deng, J. Nygård, T. S. Jespersen, C. M. Marcus, and P. Krogstrup, "Engineering hybrid epitaxial inassb/al nanowires for stronger topological protection," *Phys. Rev. Materials*, vol. 2, p. 044202, Apr 2018. [Online]. Available: https://link.aps.org/doi/10.1103/PhysRevMaterials.2.044202

[126] E. C. T. O'Farrell, A. C. C. Drachmann, M. Hell, A. Fornieri, A. M. Whiticar, E. B. Hansen, S. Gronin, G. C. Gardner, C. Thomas, M. J. Manfra, K. Flensberg, C. M. Marcus, and F. Nichele, "Hybridization of subgap states in one-dimensional superconductor-semiconductor coulomb islands," *Phys. Rev. Lett.*, vol. 121, p. 256803, Dec 2018. [Online]. Available: https://link.aps.org/doi/10.1103/PhysRevLett.121.256803

[127] J. van Veen, A. Proutski, T. Karzig, D. I. Pikulin, R. M. Lutchyn, J. Nygård, P. Krogstrup, A. Geresdi, L. P. Kouwenhoven, and J. D. Watson, "Magnetic-field-dependent quasiparticle dynamics of nanowire single-cooper-pair transistors," *Phys. Rev. B*, vol. 98, p. 174502, Nov 2018. [Online]. Available: https://link.aps.org/doi/10.1103/PhysRevB.98.174502

[128] D. J. Carrad, M. Bjergfelt, T. Kanne, M. Aagesen, F. Krizek, E. M. Fiordaliso, E. Johnson, J. Nygard, and T. S. Jespersen, "Shadow Epitaxy for In Situ Growth of Generic Semiconductor/Superconductor Hybrids," *ADVANCED MATERIALS*, vol. 32, no. 23, JUN 2020.

[129] J. Shen, G. W. Winkler, F. Borsoi, S. Heedt, V. Levajac, J.-Y. Wang, D. van Driel, D. Bouman, S. Gazibegovic, R. L. M. Op Het Veld, D. Car, J. A. Logan, M. Pendharkar, C. J. Palmstrøm, E. P. A. M. Bakkers, L. P. Kouwenhoven, and B. van Heck, "Full parity phase diagram of a proximitized nanowire island," *Phys. Rev. B*, vol. 104, p. 045422, Jul 2021. [Online]. Available: https://link.aps.org/doi/10.1103/PhysRevB.104.045422

[130] C. Fleckenstein, F. Domínguez, N. Traverso Ziani, and B. Trauzettel, "Decaying spectral oscillations in a majorana wire with finite coherence length," *Phys. Rev. B*, vol. 97, p. 155425, Apr 2018. [Online]. Available: https://link.aps.org/doi/10.1103/PhysRevB.97.155425

[131] J. C. Estrada Saldaña, A. Vekris, L. Pavešič, P. Krogstrup, R. Žitko, K. Grove-Rasmussen, and J. Nygård, "Excitations in a superconducting Coulombic energy gap," *arXiv*, Jan 2021. [Online]. Available: https://arxiv.org/abs/2101.10794v3

[132] B. van Heck, R. M. Lutchyn, and L. I. Glazman, "Conductance of a proximitized nanowire in the coulomb blockade regime," *Phys. Rev. B*, vol. 93, p. 235431, Jun 2016. [Online]. Available: https://link.aps.org/doi/10.1103/PhysRevB.93.235431

[133] A. M. Whiticar, A. Fornieri, E. C. T. O'Farrell, A. C. C. Drachmann, T. Wang, C. Thomas, S. Gronin, R. Kallaher, G. C. Gardner, M. J. Manfra, C. M. Marcus, and F. Nichele, "Coherent transport through a Majorana island in an Aharonov–Bohm interferometer - Nature Communications," *Nat. Commun.*, vol. 11, no. 3212, pp. 1–6, Jun 2020.

[134] D. Razmadze, D. Sabonis, F. K. Malinowski, G. C. Ménard, S. Pauka, H. Nguyen, D. M. van Zanten, E. C. O'Farrell, J. Suter, P. Krogstrup, F. Kuemmeth, and C. M. Marcus, "Radio-frequency methods for majorana-based quantum devices: Fast charge sensing and phase-diagram mapping," *Phys. Rev. Applied*, vol. 11, p. 064011, Jun 2019. [Online]. Available: https://link.aps.org/doi/10.1103/PhysRevApplied.11.064011

[135] D. Sabonis, E. C. T. O'Farrell, D. Razmadze, D. M. T. van Zanten, J. Suter, P. Krogstrup, and C. M. Marcus, "Dispersive sensing in hybrid InAs/Al nanowires," *Appl. Phys. Lett.*, vol. 115, no. 10, p. 102601, Sep 2019.

[136] J. van Veen, D. de Jong, L. Han, C. Prosko, P. Krogstrup, J. D. Watson, L. P. Kouwenhoven, and W. Pfaff, "Revealing charge-tunneling processes between a quantum dot and a superconducting island through gate sensing," *Phys. Rev. B*, vol. 100, p. 174508, Nov 2019. [Online]. Available: https://link.aps.org/doi/10.1103/PhysRevB.100.174508

[137] D. J. van Woerkom, A. Geresdi, and L. P. Kouwenhoven, "One minute parity lifetime of a NbTiN Cooper-pair transistor - Nature Physics," *Nat. Phys.*, vol. 11, no. 7, pp. 547–550, Jul 2015.

[138] M. Pendharkar, B. Zhang, H. Wu, A. Zarassi, P. Zhang, C. P. Dempsey, J. S. Lee, S. D. Harrington, G. Badawy, S. Gazibegovic, R. L. M. O. h. Veld, M. Rossi, J. Jung, A.-H. Chen, M. A. Verheijen, M. Hocevar, E. P. A. M. Bakkers, C. J. Palmstrøm, and S. M. Frolov, "Parity-preserving and magnetic field–resilient superconductivity in InSb nanowires with Sn shells," *Science*, vol. 372, p. 508, Apr 2021. [Online]. Available: https://www.science.org/doi/10.1126/science.aba5211

[139] T. Kanne, M. Marnauza, D. Olsteins, D. J. Carrad, J. E. Sestoft, J. de Bruijckere, L. Zeng, E. Johnson, E. Olsson, K. Grove-Rasmussen, and J. Nygård, "Epitaxial Pb on InAs nanowires for quantum devices - Nature Nanotechnology," *Nat. Nanotechnol.*, vol. 16, no. 7, pp. 776–781, Jul 2021.

[140] M. S. Bjergfelt, D. J. Carrad, T. Kanne, E. Johnson, E. M. Fiordaliso, T. S. Jespersen, and J. Nygård, "Superconductivity and Parity Preservation in As-Grown In Islands on InAs Nanowires," *Nano Lett.*, vol. 21, no. 23, pp. 9875–9881, Dec 2021.

[141] S. Vaitiekėnas, A. M. Whiticar, M.-T. Deng, F. Krizek, J. E. Sestoft, C. J. Palmstrøm, S. Marti-Sanchez, J. Arbiol, P. Krogstrup, L. Casparis, and C. M. Marcus, "Selective-area-grown semiconductor-superconductor hybrids: A basis for topological networks," *Phys. Rev. Lett.*, vol. 121, p. 147701, Oct 2018. [Online]. Available: https://link.aps.org/doi/10.1103/PhysRevLett.121.147701

[142] U. Fano, "Effects of configuration interaction on intensities and phase shifts," *Phys. Rev.*, vol. 124, pp. 1866–1878, Dec 1961. [Online]. Available: https://link.aps.org/doi/10.1103/PhysRev.124.1866

[143] B. Babić and C. Schönenberger, "Observation of fano resonances in single-wall carbon nanotubes," *Phys. Rev. B*, vol. 70, p. 195408, Nov 2004. [Online]. Available: https://link.aps.org/doi/10.1103/PhysRevB.70.195408

[144] C.-K. Chiu, J. D. Sau, and S. Das Sarma, "Conductance of a superconducting coulomb-blockaded majorana nanowire," *Phys. Rev. B*, vol. 96, p. 054504, Aug 2017. [Online]. Available: https://link.aps.org/doi/10.1103/PhysRevB.96.054504

[145] Z. Iftikhar, S. Jezouin, A. Anthore, U. Gennser, F. D. Parmentier, A. Cavanna, and F. Pierre, "Two-channel kondo effect and renormalization flow with macroscopic quantum charge states," *Nature*, vol. 526, no. 7572, pp. 233–236, Oct 2015. [Online]. Available: https://doi.org/10.1038/nature15384

[146] Z. Iftikhar, A. Anthore, A. K. Mitchell, F. D. Parmentier, U. Gennser, A. Ouerghi, A. Cavanna, C. Mora, P. Simon, and F. Pierre, "Tunable quantum criticality and super-ballistic transport in a charge kondo circuit," *Science*, vol. 360, no. 6395, pp. 1315–1320, 2018. [Online]. Available: https://www.science.org/doi/abs/10.1126/science.aan5592

[147] W. Pouse, L. Peeters, C. L. Hsueh, U. Gennser, A. Cavanna, M. A. Kastner, A. K. Mitchell, and D. Goldhaber-Gordon, "Exotic quantum critical point in a two-site charge kondo circuit," 2021.

[148] W. Little and R. Parks, "Observation of quantum periodicity in the transition temperature of a superconducting cylinder," *Physical Review Letters*, vol. 9, no. 1, p. 9, 1962.

[149] P. De Gennes, "Physique des basses températures," *C. R. Acad. Sci.*, vol. 292, p. 279, 1981.

[150] S. Vaitiekėnas, P. Krogstrup, and C. Marcus, "Anomalous metallic phase in tunable destructive superconductors," *Physical Review B*, vol. 101, no. 6, p. 060507, 2020.

[151] B. S. Deaver Jr and W. M. Fairbank, "Experimental evidence for quantized flux in superconducting cylinders," *Physical Review Letters*, vol. 7, no. 2, p. 43, 1961.

[152] R. Doll and M. Näbauer, "Experimental proof of magnetic flux quantization in a superconducting ring," *Physical Review Letters*, vol. 7, no. 2, p. 51, 1961.

REFERENCES

[153] Y. Liu, Y. Zadorozhny, M. Rosario, B. Rock, P. Carrigan, and H. Wang, "Destruction of the global phase coherence in ultrathin, doubly connected superconducting cylinders," *Science*, vol. 294, no. 5550, pp. 2332–2334, 2001.

[154] D. Sabonis, O. Erlandsson, A. Kringhøj, B. van Heck, T. W. Larsen, I. Petkovic, P. Krogstrup, K. D. Petersson, and C. M. Marcus, "Destructive Little-Parks Effect in a Full-Shell Nanowire-Based Transmon," *Phys. Rev. Lett.*, vol. 125, no. 15, p. 156804, Oct 2020.

[155] D. Razmadze, E. OFarrell, P. Krogstrup, and C. Marcus, "Quantum dot parity effects in trivial and topological josephson junctions," *Physical Review Letters*, vol. 125, no. 11, p. 116803, 2020.

[156] D. S. Golubović, W. V. Pogosov, M. Morelle, and V. V. Moshchalkov, "Little-Parks effect in a superconducting loop with a magnetic dot," *Phys. Rev. B*, vol. 68, no. 17, p. 172503, Nov 2003.

[157] A. V. Samokhvalov, A. S. Mel'nikov, J.-P. Ader, and A. I. Buzdin, "Little-Parks oscillations in hybrid ferromagnet–superconductor systems," *Phys. Rev. B*, vol. 79, no. 17, p. 174502, May 2009.

[158] G. Schwiete and Y. Oreg, "Persistent current in small superconducting rings," *Physical review letters*, vol. 103, no. 3, p. 037001, 2009.

[159] ——, "Fluctuation persistent current in small superconducting rings," *Phys. Rev. B*, vol. 82, no. 21, p. 214514, Dec 2010.

[160] I. Sternfeld, E. Levy, M. Eshkol, A. Tsukernik, M. Karpovski, H. Shtrikman, A. Kretinin, and A. Palevski, "Magnetoresistance oscillations of superconducting al-film cylinders covering inas nanowires below the quantum critical point," *Physical review letters*, vol. 107, no. 3, p. 037001, 2011.

[161] V. H. Dao and L. Chibotaru, "Destruction of global coherence in long superconducting nanocylinders," *Physical Review B*, vol. 79, no. 13, p. 134524, 2009.

[162] A. Rogachev, A. T. Bollinger, and A. Bezryadin, "Influence of High Magnetic Fields on the Superconducting Transition of One-Dimensional Nb and MoGe Nanowires," *Phys. Rev. Lett.*, vol. 94, no. 1, p. 017004, Jan 2005.

[163] N. Shah and A. Lopatin, "Microscopic analysis of the superconducting quantum critical point: Finite-temperature crossovers in transport near a pair-breaking quantum phase transition," *Phys. Rev. B*, vol. 76, p. 094511, Sep 2007. [Online]. Available: https://link.aps.org/doi/10.1103/PhysRevB.76.094511

[164] J. Bardeen, "Critical fields and currents in superconductors," *Rev. Mod. Phys.*, vol. 34, pp. 667–681, Oct 1962. [Online]. Available: https://link.aps.org/doi/10.1103/RevModPhys.34.667

[165] M. Daumens, C. Meyers, and A. Buzdin, "Little-Parks effect for arbitrary geometry: fluctuations of the magnetic moment of mesoscopic loops," *Phys. Lett. A*, vol. 248, no. 5, pp. 445–452, Nov 1998.

[166] L. Stampfer, D. J. Carrad, D. Olsteins, C. E. Petersen, S. A. Khan, P. Krogstrup, and T. S. Jespersen, "Andreev interference in the surface accumulation layer of half-shell inassb/al hybrid nanowires," *arXiv preprint arXiv:2104.00723*, 2021.

[167] R. M. Potok, I. G. Rau, H. Shtrikman, Y. Oreg, and D. Goldhaber-Gordon, "Observation of the two-channel Kondo effect - Nature," *Nature*, vol. 446, no. 7132, pp. 167–171, Mar 2007.

[168] R. Žitko and M. Fabrizio, "Non-fermi-liquid behavior in quantum impurity models with superconducting channels," *Phys. Rev. B*, vol. 95, p. 085121, Feb 2017. [Online]. Available: https://link.aps.org/doi/10.1103/PhysRevB.95.085121

[169] Y. Komijani, "Isolating kondo anyons for topological quantum computation," *Phys. Rev. B*, vol. 101, p. 235131, Jun 2020. [Online]. Available: https://link.aps.org/doi/10.1103/PhysRevB.101.235131

[170] J. M. Hergenrother, M. T. Tuominen, and M. Tinkham, "Charge transport by andreev reflection through a mesoscopic superconducting island," *Phys. Rev. Lett.*, vol. 72, pp. 1742–1745, Mar 1994. [Online]. Available: https://link.aps.org/doi/10.1103/PhysRevLett.72.1742

[171] L. Pavešić and R. Žitko, "Qubit based on spin-singlet Yu-Shiba-Rusinov states," *arXiv*, Oct 2021. [Online]. Available: https://arxiv.org/abs/2110.13881v2

[172] J. König, J. Schmid, H. Schoeller, and G. Schön, "Resonant tunneling through ultrasmall quantum dots: Zero-bias anomalies, magnetic-field dependence, and boson-assisted transport," *Phys. Rev. B*, vol. 54, no. 23, pp. 16 820–16 837, Dec 1996.

[173] H. O. Frota, "Shape of the Kondo resonance," *Phys. Rev. B*, vol. 45, no. 3, pp. 1096–1099, Jan 1992.

[174] H. Prüser, M. Wenderoth, A. Weismann, and R. G. Ulbrich, "Mapping Itinerant Electrons around Kondo Impurities," *Phys. Rev. Lett.*, vol. 108, no. 16, p. 166604, Apr 2012.